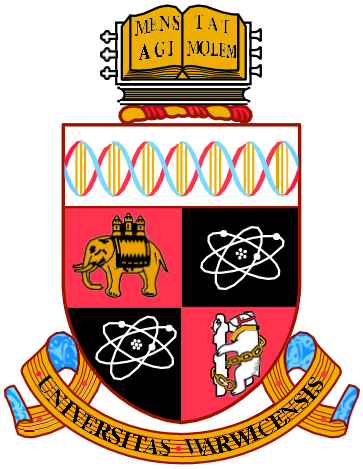

Examining biological systems at a molecular level via polarised light spectroscopy and scattering turbidity

by

Glen Dorrington

Thesis

Submitted to the University of Warwick for the degree of

Doctor of Philosophy

Supervisors: Prof. Alison Rodger, Tim Dafforn, Dave Smith and Nick Jackson

MOAC Doctoral Training Centre

September 2016

THE UNIVERSITY OF WARWICK

Table of Contents

List of Tables xiii

Abbreviations xiv

Acknowledgements xv

Declarations xvi

Abstract xvii

Chapter 1: Introduction 1

1.1 Review of optical spectroscopy, uses and importance 1

1.2 Basic principles behind spectroscopic techniques. 3

1.3 Dichroism spectroscopy. 6

1.4 Biological system components 15

DNA and Nucleotides 15

Proteins and Amino Acids 17

Liposomes and Lipids 19

1.5 Spectral artefacts and scattered light 21

Chapter 2: Theoretical scattering approaches 25

2.1 Current application 27

2.2 Rayleigh-Gans-Debye scattering 32

2.3 Derivation and calculation of turbidity linear dichroism 33

2.4 Parameters for τ_{LD} calculation 39

2.4.1 Polarisability, α 39

2.4.2 R, form function for solid ovoids and rod-like particles 39

2.4.3 Form factor *R* adjustment required for hollow particles 41

2.4.4 Peterlin-Stuart probability density function 41

2.4.5 Incident light intensity distance relationship 42

2.4.6 Wavelength dependence, bridging RGD-Mie theory 43

2.4.7 Computational integration 43

2.5 Conclusions 44

Chapter 3: Light scattering from lipid vesicles under flow 45

3.1 Overview 45

3.1.1 Scattering correction code implementation. 46

3.1.2 Application 49

3.2 Results 50

3.2.1 Leakage from liposomes at steady state and flow 52

3.2.2 Quantification of leakage from liposomes 53

3.2.3 Liposome volume change in Couette flow 55

3.2.4 Liposome LD spectra 56

3.2.5 Scattering Correction 57

3.2.6 Discussion 61

3.3 Conclusions 67

Chapter 4: Minimal component systems 70

4.1 Experimental materials and protocols 71

4.2 Analysis method: Component Gaussian decomposition 74

4.2.2 Space-scale filtering 76

4.3 Complications 79

4.3.1 CD nucleobase – DNA calculation discrepancies 80

4.4 LD fitting and component peak assignment 84

4.4.2 M13 Phage 86

4.4.3 Red blood cells (RBCs) 88

4.4.3.1 Component: Hemoglobin 91

4.4.3.2 Preliminary LD spectra 97

4.4.4 Fission Yeast Cells 100

4.5 Conclusions 104

Chapter 5: Erythrocyte LD dynamics 105

5.1 Overview 105

5.1.1 Protein orientation 105

5.1.2 Cellular orientation 109

5.1.3 Light scattering 112

5.2 Methods 114

5.3 Results: Flow Dynamics 117

5.3.1 RBC flow-on dynamics 117
5.3.2 RBC flow-off dynamics 118
5.3.3 Steric influences: Concentration and pathlength assays 120
5.4 Results: Environmental influences 122
5.5 Results: Morphological dependence 123
5.6 Results: Applications 126
5.7 Results: LD scattering influence 128
5.8 Discussion 129
5.9 Conclusions 139
Chapter 6: Conclusions and future work 141
References 144
Appendix A 148
A.1 Liposome LD scattering calculation 148
A.2 Aromatic amino acid spectra 150
A.3 M13 fitting spectra 151
A.4 Matlab scattering program code. 152
VesicleCCalc.m: Code for determination of liposome short semi-axis and associated leakage for a given long semi-axis 'c', provided the surface area matches that of a sphere of radius 'r'. 152
VesicleSCalc.m: Code for determination of liposome short semi-axis and associated leakage for a given long semi-axis 'c', provided the surface area matches that of a sphere of radius 'r' increased by a factor 'Stretch'. 152
VesicleConstantFinal.m: Code for determination of liposome scattering, provided the surface area matches that of a sphere of radius 'r'. 153
VesicleStretchFinal.m: Code for determination of liposome scattering, provided the surface area matches that of a sphere of radius 'r' increased by a factor 'Stretch'. 155
Orient.m: Code for determination of liposome orientation parameter S.[38] (primarily derived from Mchlaughan *et al*). 157

List of Figures

Figure 1.1: Basic diagram demonstrating the ability of a prism splitting light into a spectrum in the visible wavelength range). 2
Figure 1.2: Schematic diagram illustrating the basic facets of a spectroscopic setup and the possible interactions of incident light with the sample. 3
Figure 1.3: Illustration of the sinusoidal wave patterns corresponding to the electric wave vectors of polarised light that comprise the incident beams for both CD (*right*) and LD (l*eft*). Regarding the wave combination; for LD both waves are in phase, and for CD, one wave is 1/4 wavelength out of phase. E is the electric field vector, B is the magnetic field vector and k represents the axis of incident light beam direction. 8
Figure 1.4: Assorted spectra produced by 260 μM calf thymus DNA; Absorbance (Top Left) [pathlength 1cm], CD (Top Right, [path-length 1 cm]) and LD (Bottom, [path-length 0.05 cm]). 9
Figure 1.5: Four commonly used methods for the induction of biomolecular orientation: (a) Flow-orientation, (b) EM orientation, (c) Thin-film alignment and (c) Squeeze alignment[111]. 10
Figure 1.6: Schematic illustrating the shear flow system, standard rotary speeds are 3000rpm. 12
Figure 1.7: [28]Schematic depicting the structural elements comprising the primary 4 nucleotides, and the double-helical DNA structure that they form. 16
Figure 1.8: Molecular structure of the four standard aromatic amino acids. 17
Figure 1.9: [30]Diagram of protein structure, using PNCA as an example 18
Figure 1.10: [31]Graphical representation of protein secondary structural elements and their absorbance contributions with regards to their orientation relative to incident light direction. 19
Figure 1.11: Molecular structure of phosphatidylchloline (top) and the associated macromolecules lipid structures formed (bottom) 20
Figure 1.12: [26]Representative flow LD of intrinsic microtubules and the corresponding scattering subtraction. 22
Figure 2.1: Illustration of the light scattering produced by an induced dipole moment after exposure to an incident electromagnetic wave (*Vo* relates to the frequency of the incident light)[33]. 26
Figure 2.2: Tryptophan UV-Vis absorption spectrum with associated scattered fit via the non- linear regression approach [0.1 mg/ml, pathlength: 1mm]. Scattering was calculated from the 310- 500 nm region of non-absorption. 30
Figure 2.3: Coffee Creamer 2.5 g/ml UV-Visible absorption spectrum overlaid with that of the predicted scattering from Mie-Sphere scattering code, particle radius: 255 nm. 31

Figure 2.4: Schematic for an LD experiment outlining the scattering vector s and associated polar and azimuthal angles for particle orientation axis **P**(θ, ϕ), and propagation vector **s**(β, ε).....34
Figure 2.5: Schematic diagram of the scattering plane (*X, Y', Z'*); (a) Plane orientation with respect to the initial *X,Y,Z* coordinate system. (b) Scattered wave polarization in relation to the initial (*X, Y, Z*). (b) Scattered wave polarization in relation to the τ_{LD} axis system. The bisectrix of **s** is given by angle γ bounded by *XOB*.....35
Figure 2.6: Schematic outlining the plane of reference and the origin of the values present within the *S* matrix; *l* and *r* denote the parallel and perpendicular unit vectors with regards to the plane, ID corresponds to the origin of the induced dipole moment as the incident light strikes the particle..37
Figure 3.1: Lipids used in the calcein leakage study, with the exception of BTLE, which is a composite variety of lipids.....47
Figure 3.2: Demonstration of the created GUI for the purpose of scattering correction for de- formable spheroidal particles with alternate mode to permit membrane stretching, and various particle specific input parameters.....50
Figure 3.3: (a) Emission spectra for calcein excited at 460 nm as a function of concentration. (b) Concentration of calcein against maximum of emitted fluorescence.....51
Figure 3.4: Couette shear flow on (3000 rpm)/off: (left) fluorescence and (right) fluorescence + scattering time-courses, for calcein (50 mM initial concentration inside liposomes) filled soybean PC liposomes (20 mg/mL) [52].....53
Figure 3.5: Fluorescence of calcein leaked from a variety of liposomes preparations (Figure 3.1) with and without the influence of shear flow as indicated in the figures. a) Stationary samples. b) Samples in Couette flow. c) Traces for pure DMPC liposomes fitted to a curve, since measured values had poor signal: noise. Initial calcein concentration inside liposomes 50 mM, lipid concentration 20 mg/ml, pathlength: 0.5 mm.[53].....54
Figure 3.6: Ovoid model of liposomes used herein: length *L*, radii of both other axes are identical and denoted *r*.....56
Figure 3.7: Molecular structure of the fluorescent chromophore DPH and its stretched film LD spectrum dropped from a concentrated solution in $CHCl_3$ onto pre-stretched polyethylene film. 57
Figure 3.8: Representative LD spectra from POPC liposome preparations, (7.5 mM), with fitted scattering curve for a set volume loss of 1.4%. Samples were prepared containing DPH (1%w/w) with associated fitted scattering curves and corrected spectra for constant surface area. Pathlength: 0.5 mm.....58
Figure 3.9: Representative LD spectra from POPC/POPS/cholesterol liposome preparations, (total concentration 7.1 mM, mixed at a 75:10:15 ratio). Samples were prepared containing DPH (1%w/w) with associated fitted scattering curves and corrected spectra for constant surface area. Pathlength: 0.5 mm.....58

Figure 3.10: Representative LD spectra from Soy-PC liposome preparations, (10 mM). Samples were prepared containing DPH (1%w/w) with associated fitted scattering curves and corrected spectra for constant surface area. Pathlength: 0.5 mm. 59
Figure 3.11: Representative LD plots for diphenylalanine (top) and FtsZ (bottom) flow orientated fiber particles. Legend for diphenylalanine denotes time (mins) since the initiation of fiber growth[55] ... 66
Figure 4.1: *Top* Space Scale Image of CMP (UV-Vis Absorption Spectrum). *Bottom* UV-Vis Absorption spectrum of cytosine with peak Gaussian contributions labelled (vertical lines) 78
Figure 4.2: Example of the Gaussian fitted curves (Bold) and component Gaussians (Hairline), for CMP absorbance spectra. 78
Figure 4.3: Component spectra for each of the DNA nucleotides, *Left* Experimentally collected absorbance data (GDP 216 μg/ml, ADP 118.5 μg/ml, CMP 175.2 μg/ml, TMP 217 μg/ml, pathlength = 1cm). Samples were concentration corrected and zeroed at 350 nm (absence of absorbance). *Right,* Literature representation of the CD spectra given from each of the pure nucleotide bases. 80
Figure 4.4: Literature estimated transition moments for the nucleotide base, Guanine[61]. 81
Figure 4.5: Contrast of the calculated DNA CD to actual DNA CD spectra. (GDP 46μg/ml, ADP 118.5μg/ml, CMP 175.2μg/ml, TMP 217μg/ml, DNA 260 μg/ml, pathlength = 1cm with the exception of GDP which was 1mm to optimise recordings). Samples were concentration corrected and zeroed at 350nm (absence of absorbance). 82
Figure 4.6: Representative CD spectra for both A (30ug/ml) and B (260ug/ml) isoforms of DNA. A-DNA was concentration corrected via the Beer-lambert Law, to be equivalent to B-DNA), Samples were zeroed at 350nm (absence of absorbance), pathlength = 1cm 84
Figure 4.7: Overlay of the normalised calf-thymus spectra from composite nucleobase absorbance fitting (magenta), and DNA absorbance (blue) and LD (black). Vertical lines represent peak values 86
Figure 4.8: Schematic depicting M13 bacteriophage and key capsid proteins[78] 87
Figure 4.9: Spectra overlay of M13 LD with peak component Gaussian values represented by vertical lines; *Top*, [Trp (Blue), Tyr (Orange) and Phe (Magenta)]. *Bot*, [GDP (Blue), ADP (Red), TMP (Magenta) and CMP (Green)] 88
Figure 4.10: Graphical representation of red blood cell in flow[77] 89
Figure 4.11: Demonstrating of a red blood cell plasma membrane with a variety of integral and structural proteins.[72] 90
Figure 4.12: Illustration of the core square planar form of the porphyrin based heme chromophore (and the plane in which the primary Soret $\pi - \pi^*$ bands absorb) and as part of its parent protein hemoglobin (*right*), [Source PDB, 1GZX, porphyrin rings are defined in green][65] 92
Figure 4.13: Representative absorbance spectra for lysed cell preparations [conc. 1.5% PCV, pathlength = 1mm]. 93

Figure 4.14: Literature absorption spectra of the common derivatives of bovine (—) and human (– – – –) hemoglobin in the visible range. (A) oxyhemoglobin (1) and deoxyhemoglobin (2); (B) methemoglobin (1) and carboxyhemoglobin (2)[75] 95
Figure 4.15. Absorbance spectrum for powdered haemoglobin suspensions; *Left*, full spectrum. *Right*, expansion of the hemoglobin low intensity region containing the porphyrin Q-bands 95
Figure 4.16: Absorbance spectra for intact and lysed cell preparations, (lysis by replacement of cell buffer with purified water.) [conc. 1.5% PCV, pathlength = 1mm] 96
Figure 4.17: Shear-flow difference LD spectrum collected from an erythrocyte cell preparation in PBS buffer. [conc 3% PCV, pathlength = 0.5mm, position 29cm] 98
Figure 4.18: Representative flow state LD spectrum from an erythrocyte cell preparation in PBS buffer. [conc 3% PCV, pathlength = 0.5mm] 99
Figure 4.19: Flow-off state LD (*left*) and absorbance (*right*) spectra from an erythrocyte cell preparation in PBS buffer. [conc. 3% PCV, pathlength = 1mm] 99
Figure 4.20: Microscopic view from a fission yeast culture from the literature[79]. 101
Figure 4.21: Absorbance spectra from a fission yeast sample suspended in purified water, (conc. 5% PCV, pathlength 0.5mm). 102
Figure 4.22: LD spectra from a fission yeast sample suspended in purified water, (conc. 5% packed cell volume, pathlength 0.5mm). *Left*: Flow on/off difference spectrum. *Right:* Individual base-lined flow on/off spectra. 103
Figure 5.1: Literature illustration of the angular states of the planar heme group within deoxyhemoglobin; projection of the proteins molecular surface (*Top*) and optical absorption ellipsoid (*Bottom*). Central 2-fold molecular axes are shown to demonstrate the various angular positions of the collective heme planes in contrast to the natural axis of the beta 6 residues. The views are drawn from computer plots of a stick model using atomic coordinates of horse deoxyhemoglobin, whose structure is very similar to that of human deoxyhemoglobin A[65] 107
Figure 5.2: The flow orientation distribution of healthy red blood cells (hollow circles) and hardened cells (solid circles, hardened by treatment with glutaraldehyde) oriented such that the cellular long axis has an angle of < 20° with respect to the flow direction[103] 110
Figure 5.3: Graphical representation of the transition from a normal red blood cell to echinocyte (hypertonic) and stomatocyte geometries (hypotonic) based on the osmotic pressure of the buffer. 111
Figure 5.4: Evaluated differential scattering cross sections for rim-on He-Ne laser light illumination of a biconcave-disk-shaped RBC plotted versus the scattering angle θ [89] 113
Figure 5.5: Apparatus used in the angular contribution assays to move samples in 1mm and 1cm pathlength quartz cuvettes along the incident light direction (left to right) between emitter and detector. 116
Figure 5.6: Representative LD variable duration assay [conc.: 3% PCV, pathlength = 0.5mm] 117

Figure 5.7: Microscopy images for RBCs. *Left* 1% PCV, *Right* 2% PCV. Scale automatically determined by the Auto M10 Cellometer for cells of 2-12um in size. 118
Figure 5.8: Time-course flow-off LD spectra taken at 3-minute intervals over the course of an hour. [conc. 1.5% PCV, pathlength 1mm, position 29cm]. 120
Figure 5.9: LD flow-off (Left) and Absorbance (Right) spectra from serially diluted RBC sus- pensions in PBS to four concentrations; LD data has been concentration corrected and zeroed to a non-absorbing wavelength (750 nm) to contrast peak intensities. [pathlength: 1mm] 121
Figure 5.10: Flow-off LD spectra demonstrating the influence of hemoglobin oxygenation state for both LD (*left*) and Absorbance (*right*). [conc.: 1.5% PCV, pathlength = 0.5mm]. Data has been zeroed to a non-absorbing wavelength (750nm) to contrast peak intensities 123
Figure 5.11: Flow-off RBC LD spectra in PBS for a range of buffer tonicity. Data has been shown as zeroed to a non-absorbing wavelength (750nm) (*left*), and raw data in contrast to the buffer baseline (*right*). [conc.: 1.5% PCV, pathlength: 1mm, position: 18cm from emitter]. 124
Figure 5.12: Flow-off RBC LD spectra in saline buffer under pH basic conditions in contrast to neutral standard conditions (pH 7). Data has been zeroed to a non-absorbing wavelength (750nm) to contrast peak intensities (*left*), and raw data in contrast to the buffer baseline (*right*). Samples were recorded both immediately after pH fixing ('init'*)* and after 5 minutes of equilibration ('end'). [conc.: 1.5% PCV, pathlength: 1mm, position: 18cm from emitter] 125
Figure 5.13: Phosphate salt-free buffer LD assay. Samples were incubated at either 4 or 37ºC for a 24h period and contrasted to a standard 4ºC sample allowed to equilibrate for a period of 2h. [conc.: 1.5% PCV, pathlength: 1mm, position: 18cm from emitter] 127
Figure 5.14: LD distance assay for zeroed (*left*) and non-zeroed (*right*) samples. Legend denotes the spacing distance between sample position and the light emitter aperture. (Left) Spectra were zeroed (at 700nm) after baseline solvent correction for clarity. Distance from emitter to detector apertures was 30cm in total. [Conc: 0.15% PCV, pathlength = 1cm] 128
Figure 5.15: Illustration of the various falling dynamics demonstrated by discs depending on the Reynolds number and inertia of the falling disc; a) Steady-falling regime observed at lower Reynolds (Re) numbers, b) Periodic-oscillating motion observed at higher Re and low dimensionless moment of inertia (I), c) Chaotic motion found when both Re and I are moderately large. d) Tumbling motion found at very large inertia. [Figure reproduced from literature[96]] 131
Figure 5.16: Illustration of a simplistic LD setup and the relative orientations of both cell and heme plane within a 1mm rectangular cuvette. 135
Figure 5.17: A cross-section of a sickle red blood cell, demonstrating the polymerised hemoglobin- S strands forming along the long axis forcing the characteristic distortion of shape[107] 135
Figure A.1: Calcein leakage fluorescence spectra collected from DMPC vesicles under flow on and off conditions, [conc 20ug/ml, pathlength 0.5mm] 148

Figure A.4: Absorbance spectra for each of the aromatic amino acids at a variety of concentrations and pathlength (as denoted in the corresponding graph legend). 150
Figure A.5: Near-UV CD spectra for each of the aromatic amino acids at 1mg/ml, [pathlength (Trp, Tyr) 1mm, (Phe) 1cm]. 150
Figure A.6: Overlaid spectrum of the fitted absorbance spectrum for M13 with associated Gaussians, and the M13 LD spectrum. Vertical lines represent peak values for the component Gaussians... 151

List of Tables

Table 3.1: Vesicle scattering correction program input parameters used to model the experimental setup. 48

Table 3.2: Example values of orientation parameter *S*, and volume *V*, calculated according to for ovoids of length *L*, and radius *r*, with the same surface area as a sphere of radius 50 nm and volume 524,000 nm^3. This makes an upper bound for volume change induced by shear flow 56

Table 3.3: Examples of calculated liposome deformation parameters for several liposome varieties, with concentrations changed by serial dilution. Samples denoted [1,2] indicate repeated identical preparations. Top: Constant surface area; Bottom: surface area expanded such that soybean PC had a value of 0.03 for S. POPC (10 mM) samples were used as the standard to calculate the instrument parameter, I_0/r^2, as outlined in the text. Actual % volume loss determined by the difference in maximum % volume loss in Fig 3.5 for each lipid between flow states. 60

Table 4.1: Standard scanning machine parameters for the measurement of absorbance, LD and CD within the UV-Vis wavelength range. 72

Abbreviations

LD	Linear Dichroism
CD	Circular Dichroism
IR	Infrared
RGD	Rayleigh-Gans-Debye
DLS	Dynamic Light Scattering
DNA	Deoxyribonucleic acid
RBC	Red blood cell
DPH	1,6-Diphenyl-1,3,5-hexatriene
POPC	1-palmitoyl-2-oleoyl-sn-glycero-3-phosphocholine
POPS	1-palmitoyl-2-oleoyl-sn-glycero-3-phospho-L-serine (sodium salt)
DMPC	1,2-dimyristoyl-sn-glycero-3-phosphocholine
BTLE	Brain total lipid extract
PBS	Phosphate buffered Saline

Acknowledgements

Professor Alison Rodger, Dr Nikola Chmel and the rest of the Warwick Biological Chemistry research group.

Declarations

The work presented in this document is original. At time of writing, only material in Chapter 3 regarding the light scattering calculations produced by liposomes under flow has been published as part of a light scattering review paper[110]. The author of this thesis carried out all work, except where specifically stated in the text.

Abstract

During the course of this work the development and optimisation of the dichroism field of spectroscopic techniques regarding their application towards living biological systems has been examined. To this end we have studied the theory of light scattering, as one of the principle flaws that can prevent accurate analysis of spectral data. The fields of Rayleigh-Gans-Debye and Mie theory were investigated and implemented into a program for the calculation of scattering for various different systems. The developed program was then optimised using previously collected data regarding the scattering produced by liposomes under flow, and further data regarding the deformation of liposomes validated. A secondary feature to be addressed was the inherent complexity of cellular spectra that comprise a variety of different components. Experimental studies were therefore conducted regarding the deconvolution of several biological systems in terms of their individual chromophores, in increasing degrees of complexity. An approach in which each component was converted into a series of Gaussian curves and the contribution of sets of these Gaussians (from each component) to the overall system spectrum was developed. Since biological systems contain various components that interact with each other, such as the hypochromicity of DNA, the influence on this spectral decomposition approach was also outlined and studied. Unusual features were observed in the most complex cellular samples of red blood cells and fission yeast, regarding the linear dichroism (LD) spectra produced in the absence of flow. Further studies were conducted regarding the simpler of these systems, red blood cells, to determine the source of these spectral features. The principle component was determined to be oxy-hemoglobin, and that both cellular and protein orientation was required to produce the observed LD spectrum. Sedimentary forces were then discovered to be the signal source within the sample vessel, and the spectrum comprised of both absorbing and scattering elements. Of the latter, both typical RGD/Mie type scattering was observed in addition to resonance scattering. In addition, it was observed that alterations to the cellular geometry, due to various

environmental influences such as pH and tonicity, were directly related to spectral behaviour.

Chapter 1: Introduction

One of the most significant issues in the current research climate is the matter of detection. Without adequate means with which to investigate samples, be they macroscopic or molecular, biological or synthetic, the latter stages of research involving analysis and application become impossible. In fact, this can be further expanded towards the capacity to ascertain whether or not that there is actually exists a feature of interest to further investigate. Therefore, the adaptation and optimisation of existent techniques and the development of novel ones is of vital importance to practically all categories of analytical science. Discussed in this thesis is the step-wise development of a novel application for spectroscopic techniques aiming towards investigation of living cells. The spectroscopic techniques of interest include absorbance, circular and linear dichroism, and the analysis of the resultant data that was optimised via the application of modified light scattering theory.

1.1 Review of optical spectroscopy, uses and importance

When it comes to the general scientific field of detection and analysis, it can be generally split up into several different levels of resolution. Low resolution techniques are easily exemplified by optical microscopy, a technique by which it is easy to obtain large scale structural information about the sample of interest[1]. Conversely there is the extremely high resolution of crystallographic techniques, permitting observation of a sample at, or close to, the atomic-level[2]. Each excels within the resolution limits of its own field, but cannot be easily expanded to cover aspects of the other. Spectroscopy however is harder to define, since depending on the technique, the sample, and the method used one can examine the structural features of individual proteins or investigate macro-molecular organisation – often within the same samples[3]. Due to this, spectroscopy has proven to be ideal for the bridging of these two resolution regimes. The field of optical spectroscopy is an ancient one; in fact the basic ability of a prism to present a rainbow of colours was noted (although obviously not understood) as far back as the Roman Empire[3]. However, it took until the 17th century before

several researchers and most notably Sir Isaac Newton explored some of the inferences of this in terms of actually splitting light into component parts.

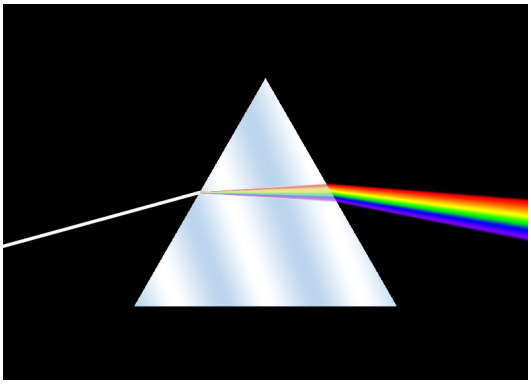

Figure 1.1: Basic diagram demonstrating the ability of a prism splitting light into a spectrum in the visible wavelength range).

This was only the very beginning; however, and soon the nature of light as a wave began to be understood in terms of interference patterns and diffraction. The crucial step was at last taken with the discovery and application of diffraction gratings (Fraunhofer) in place of the prism, and allowed for much finer wavelength resolution and most importantly quantification[4]. With this in place, by the 1900's the groundwork for the field of spectroscopy was finally ready. To accompany this, scientists also began to notice the connection between sample material and the emission of different colours (at the time conducted via the combustion of various salts and soon to be accompanied by observations on the differing coloured sparks given out by different metals), which has in essence become the flame spectroscopy of today[5]. Over the years since, this field has grown rapidly and has spawned a huge subset of spectroscopic techniques each specialised for a particular purpose. To illustrate their importance a few examples of these techniques and what purposes they have been used:

- Raman spectroscopy[6]: Chemical Fingerprinting, Bio-pharmaceuticals
- Infrared spectroscopy[7]: Molecular Bonding, Forensic Science
- Fluorescence spectroscopy[8]: Organic Compounds, HPLC Purification

1.2 Basic principles behind spectroscopic techniques.

Behind every type of optical spectroscopy there are several essential facets that are the same for each variant; these are primarily to do with fundamental laws on how incident light interacts with particles. This is easily noticeable when considering the fact that the absorbance of light acts as a basis for the aforementioned techniques (i.e. Raman and Fluorescence spectroscopy). We will begin by discussing the core principles behind absorbance spectroscopy, the most basic of spectroscopy techniques[9].

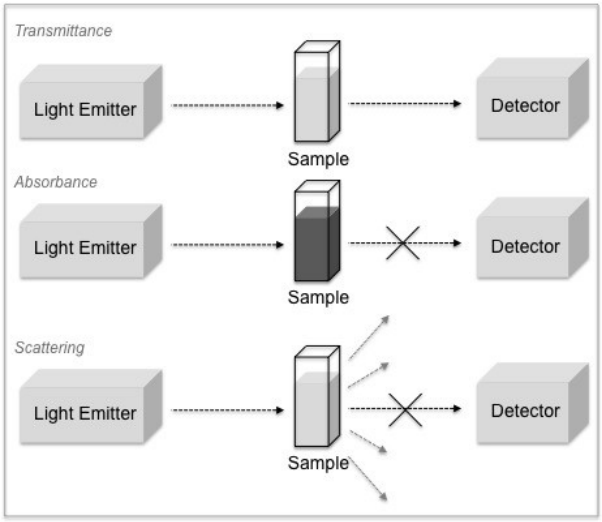

Figure 1.2: Schematic diagram illustrating the basic facets of a spectroscopic setup and the possible interactions of incident light with the sample.

In the simplest fashion, a spectroscopic experiment is demonstrated in Fig.1.2, outlining the 3 key features found in any spectroscopic setup. In practise this setup is far more complex even for simple absorbance spectroscopy, involving adjustments to these features (and/or the inclusion of additional ones dependant on the technique being used), however, the behaviour of this central system always remains the same. When incident light strikes a sample, there are 3 effects that can occur. Firstly there is *transmission*, where the light simply passes through the sample without any further interactions and strikes the detector. Since there is no energy loss from interaction with the sample, there is therefore no change to the incident wave and what is recorded is simply the baseline light from the emitter. Since the sample absorbance is the feature being investigated (i.e. the 'loss' of light striking the detector), usually a measurement

using a blank sample is used to record a transmission spectrum (i.e., a baseline spectrum) in order to remove any potential noise inherent to the instrument. When subtracted from a resultant absorbance spectrum what results is a much cleaner pure absorbance spectrum, better suited to be quantitatively analysed.

Secondly is *absorbance*. When an incident light wave strikes an absorbing particle, there may occur a loss of intensity that the sample absorbs, usually seen as an excitation of electrons or vibrations within the sample to a higher energy level. It can also be thought of as the sample absorbing photons from the incident light wave. The structure of a particle dictates this wavelength dependent absorbance intensity pattern (i.e. a spectrum), and can be deconvoluted and understood in terms of its component parts. For example particles containing a C-H alkyl bond will tend to absorb primarily at 7900 nm in the IR region. This capacity to identify and analyse the molecular structure of a completely unknown compound is why the technique is so highly valued[7]. Similarly taking a sample of a known spectrum, this approach can be used to detect any impurities present within a sample. This is not however restricted to chemical compounds, and can just as easily be applied to much more complex biological systems. However, with such a large increase in complexity within a sample comes a corresponding loss of resolution; it becomes near impossible to determine the absorbance of individual chemical bonds. Instead broader peak patterns become identifiable corresponding to component parts within a greater macrostructure (e.g. tryptophan amino acid absorbance patterns detectable within a protein). In addition this setup allows for dynamic measurement, directly detecting the changes in sample structure over time further allowing the kinetics of reactions to be examined. A secondary effect that can occur following the absorption of photons is *emission* where the sample re-emits photons as it drops down to a lower energy state, the energy loss dictating the wavelength of the emitted photon. There are however also several mechanisms by which the particle can relax back to its ground state (e.g. dissipation by heat) that do not result in the emission of photons. This explains why there is usually a difference in excitation and emission wavelengths and the released photon is of a lower energy (longer wavelength). Similarly to absorbance, the composition of the sample

determines the emission spectrum, which is in fact the basis of emission and fluorescence spectroscopy[8].

The last facet of this simple setup is *light scattering* and is easily the most complex (which strictly speaking should be expanded to also include effects such as 'stray light' penetrating this closed system)[10]. A common understanding of light scattering when it comes to spectroscopy, and for why it can be grouped with stray light, is that it is seen to act as an artefact that obstructs the collection and analysis of spectral data. Scattering is normally presented as a smooth baseline shift in the absorbance intensity. When incident light strikes a particle, a proportion of its intensity will be diverted away from the initial light propagation direction causing that light to miss the detector (strictly speaking it is more complex than this and will be discussed later on). Therefore as far as the detector is functionally aware, this is acting identically to the loss of intensity caused by absorbance. The principle difference is that for the vast majority of cases the scattering spectrum is not dependent on the chemical nature of the particle, but purely on its physical characteristics such as the particle geometry and refractive index. Additionally, unlike the complex chemical nature of a particle, the physical characteristics of a particle can be precisely measured beforehand and so it can be treated as a predictable independent variable. As such there have been several regimes of theory, developed for a variety of particle shapes and sizes, in order to predict various parameters (such as the angular distribution and intensity of scattered light given off by a particle)[11]. The subtraction of this calculated scattering spectrum should therefore allow for a more accurate quantitative comparison between absorbance spectra.

A novel aspect that is introduced in this work however, is the application of these scattering theories not simply as a reduction in spectral 'noise', but to also act as a source of information about the particle's physical aspects. For uniform hard particles this may be unimportant, since it is relatively easy to ascertain their geometry with other analytical techniques beforehand and the scattering they cause will not change. However, when dealing with soft/flexible particles that are capable of changing size or geometry during the course of an experiment, this can be of great use to track such changes. The capability of tracking dynamic changes to a particle over

time is of great use to understand its behaviour in response to different environments / forces (e.g. osmotic forces, shear flow).

1.3 Dichroism spectroscopy.

One particular field of spectroscopy, one that will be used extensively in this work, is that of *dichroism* spectroscopy[12]. There are two branches to this field, circular and linear, denoting the polarisation of the light used to investigate the same. The former method is used to investigate the presence and behaviour of *chiral* structures within the sample, such as helical secondary structural elements in proteins. Further changes in this structure can be related to changes in the spectral data recorded and analysed. The latter is instead used to investigate the presence and behaviour of *alignable* structures within the given sample, such as long thin fibrous proteins. Due to the requirement for these structures to be induced to align within the sample before they can be detected, linear dichroism is a more recent development and less explored than circular dichroism.

Precisely how LD is conducted can be explained most easily by first considering the light waves that comprise the incident light striking the particle. Any electromagnetic wave, such as that of the emitted light, consists of two transverse waves much like sine waves travelling down the incident light path (the light beam produced by the passing through the sample material to the detector within the machine apparatus), for both electric and magnetic fields. If we first consider an incident 'natural' light beam as a stream of photons, each of those photons possesses an electric wave vector that is perpendicular to the direction of travel and that wave vector fluctuates in magnitude as a sine wave in the same direction. If we look down this beam of natural light the electric field vector of these sine waves is not restricted in its range of rotation around the incident light axis. If we examine these sine waves in regard to a reference axis perpendicular to this incident light axis (commonly selected to be the shear flow axis direction, as defined later), these waves can therefore be thought of as an infinite series of possible angles for each wave vector a photon could result in. The restriction of this orientation of the electric field vector around a

central axis (usually the incident beam direction) to a smaller range of angles, or even a single plane, determines the *polarisation* of that wave.

In dichroism spectroscopy, the polarisation of the incident light waves is restricted in two different manners. Firstly there is linear dichroism (LD), when this infinite series is restricted to that of a single angle (by means of a filter), the photons in the resulting beam all have their electric field vectors in the same direction forming a single linearly orientated plane (or more accurately a small sub-set of angles since it is impossible have a perfectly oriented plane of light)[12]. Alternatively there is circular dichroism (CD), where the light polarisation rotates constantly as the wave propagates down the direction of travel[13]. This is accomplished by taking the sum of two linearly polarised light beams, oriented perpendicular to each other and offset such that they are ¼ of a wavelength out of phase (via a ¼ wave plate). The resultant wave forms a spiral, where the wave vector now no longer varies in magnitude but in direction. These two forms of dichroism spectroscopy (Linear and Circular) form a sub-set of spectroscopy that has been established for decades and precisely how the chromophores within the particle (essentially the part of the particle that are responsible for the absorption) act in response to these polarizations gives rise to different degrees of intensity dependent on the polarization and state of the particle in question. With this technique then aspects of both high and low resolution analytical techniques can start to be seen, since not only can the presence of features within a sample (e.g. amino acids, like Trp) be detected but also information regarding intermolecular interactions and structure can be obtained.

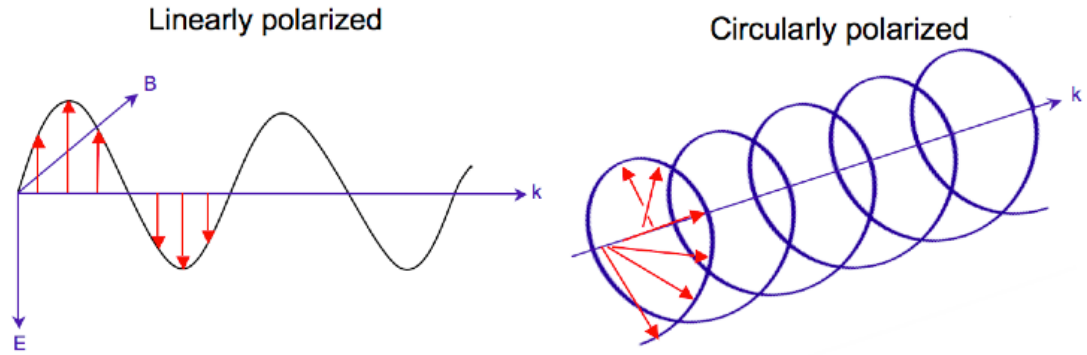

Figure 1.3: Illustration of the sinusoidal wave patterns corresponding to the electric wave vectors of polarised light that comprise the incident beams for both CD (*right*) and LD (l*eft*). Regarding the wave combination; for LD both waves are in phase, and for CD, one wave is 1/4 wavelength out of phase. E is the electric field vector, B is the magnetic field vector and k represents the axis of incident light beam direction.

If we were now to consider an appropriate sample, the classical example to be DNA, we can see how these polarised planes of light interact in each case[13]. From the standard absorbance spectrum we can see that the chromophores within a DNA strand broadly absorbs in the 240–280 nm region peaking at 260 nm. In dichroism spectroscopy the key feature examined is the differential absorbance between samples exposed to light polarised in opposite directions. For example, for circular dichroism the resultant spectrum shown is in fact the difference in absorbance samples exhibit when subjected to left-handed vs. right-handed circularly polarised light. In contrast for LD the difference observed is between absorbance for light polarised horizontally vs. vertically. Depending on how the chromophores (part of the particle that absorbs light) within the sample absorb light with regards to polarisation direction, different spectral patterns can be seen.

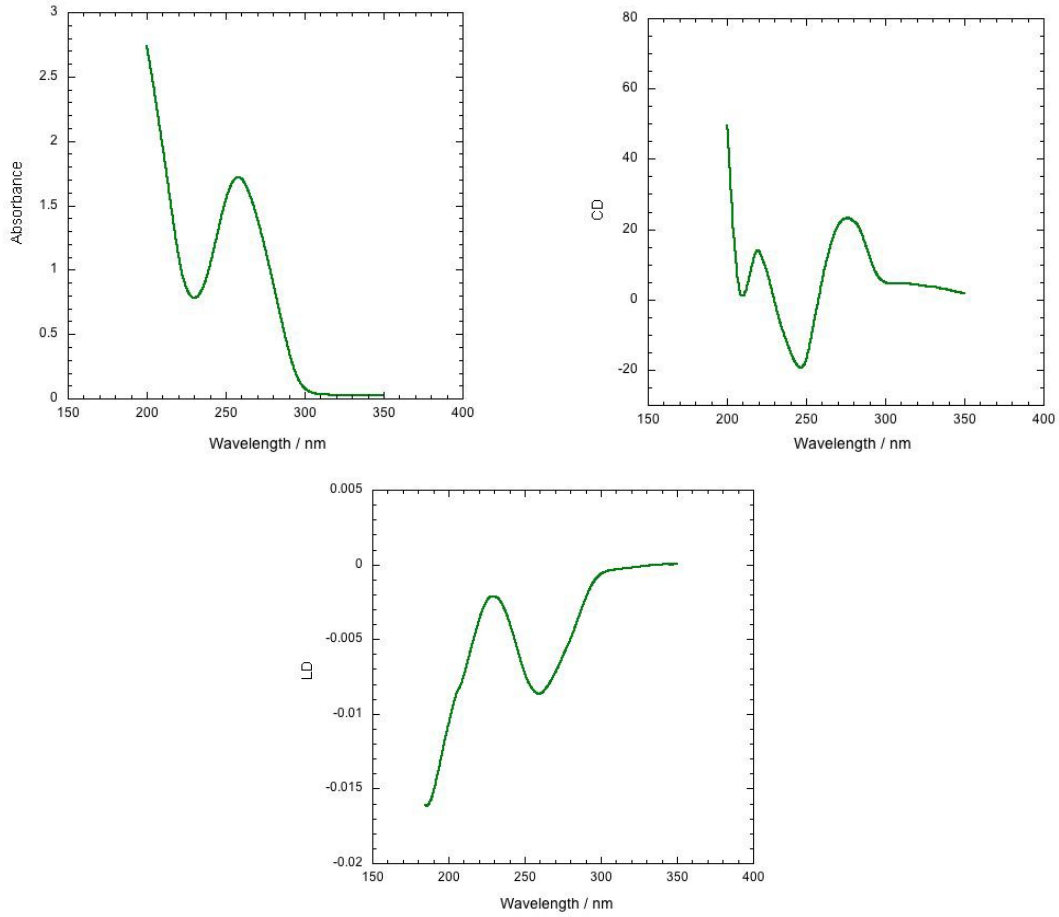

Figure 1.4: Assorted spectra produced by 260 μM calf thymus DNA; Absorbance (Top Left) [pathlength 1cm], CD (Top Right, [path-length 1 cm]) and LD (Bottom, [path-length 0.05 cm]).

An additional step is required for the measurement of LD in particular however, since unlike CD (which simply detect chiral presences within the sample, such as the helical rotation of a DNA strand) there is usually no reason for samples to be oriented in favour of either horizontal or vertical directions. This DNA LD spectrum is therefore produced due of the influence of an induced flow system necessary in order to detect any LD signal at all. Within a sample vessel even if a sample contains molecules, like DNA, that are strongly alignable (as most particles with such an extreme axis ratio tend to be) a LD signal still will not be detected because they will still exist in a random orientation within the solution, and an external influence is required in order to align them. As such, two elements are needed to produce a LD signal, an alignable particle and a method by which to align it. There are multiple methods that have been

used in related studies in the literature that require a means to induce biomolecular orientation.

There are four common methods used for this purpose; thin film orientation, electromagnetic (EM) orientation, gel squeezing, and shear-flow orientation[111]. Each of these alternate methods is suitable for different types of biological particles, an example of which can be most easily seen with EM orientation where the particles are requires to have intrinsic charged dipole properties.

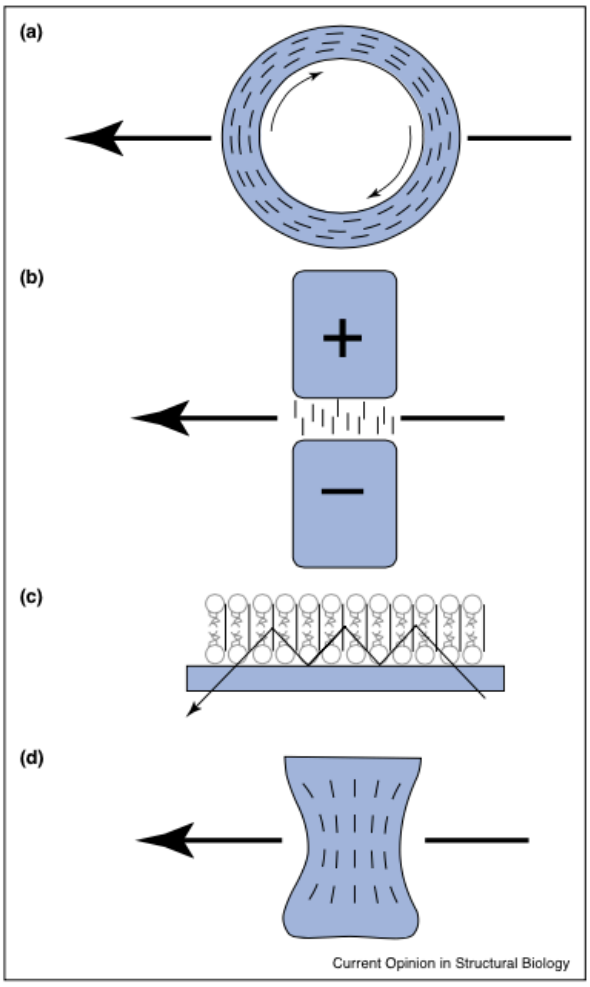

Figure 1.5: Four commonly used methods for the induction of biomolecular orientation: (a) Flow-orientation, (b) EM orientation, (c) Thin-film alignment and (c) Squeeze alignment[111].

Each of these methods also has intrinsic advantages and disadvantages in contrast to each other. For example thin-film may orient sample particles to a greater extent than

others like shear-flow or squeeze-alignment, but often require the drying of the sample (to fix the film to the surface), which may negatively influence the behaviour of certain samples. In addition dependent upon the analytical technique involved, some approaches may be more advantages or practical than others. A practical example of this can be seen in relation to linear dichroism in the work of Bechinger *et al*[112] regarding the polarised infrared attenuated total reflection spectra oriented multi-layered lipid bilayers. In the aforementioned work the behaviour of specific peptides when interacting with the bilayer membrane are examined and their relative orientation analysed. The orientation of various membrane related structures (such as bound or integrated proteins) are typically best examined via this method as opposed to the alternatives, Fig 1.5, as they should orient in the same manner across the entire surface providing a strong prevailing particle orientation which can be detected and analysed using LD.

The method chosen to be used in this work is known as *shear flow*[14]. This setup consists of a cylindrical sample holder (quartz couette), and a central solid quartz rod. When the Couette cell is rapidly rotated the central rod is kept stationary. The resulting shear forces form a rapid flow system within solution inducing any particles within the sample capable of alignment to align in the direction of the flow. The resultant flow-LD calculation takes the difference in absorbance between light polarised either parallel or perpendicular to this flow direction. In addition a difference is also taken between the induced flow samples and those under stationary conditions. This difference essentially baselines the data by eliminates any background noise produced from either the equipment or instrument (since it should be present identically in both shear flow states). The resultant data produced from LD analysis, (and CD using pure water samples), can therefore be thought of as a double-difference.

$$LD = (A_{para} - A_{perp})_{flow-on} - (A_{para} - A_{perp})_{flow-off}$$

Lastly the chromophores in a DNA strand have been observed to absorb light more strongly from light polarised perpendicular to the strands axis of alignment (and so also the flow direction) and consequently the resultant transition sign is negative[13].

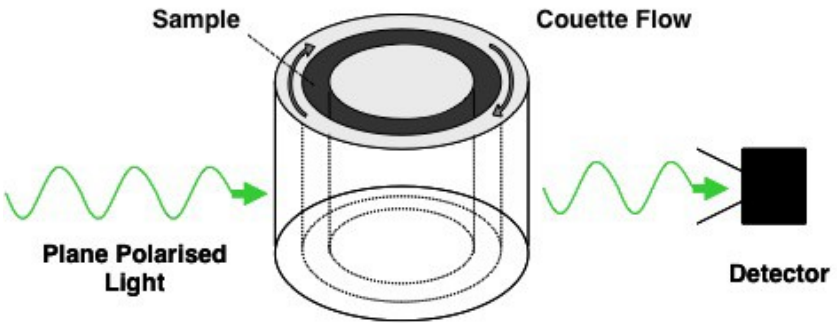

Figure 1.6: Schematic illustrating the shear flow system, standard rotary speeds are 3000rpm.

A traditional dichroism experimental setup therefore includes the light emitter, the incident light polarised either circularly or linearly depending on which is being examined. The sample is then placed in the path of this beam with the detection apparatus positioned behind. For linear dichroism experiments the sample holder is a cylindrical quartz cuvette, within which shear flow is induced (as shown above). Alternatively circular dichroism, since no flow-orientation is required, a rectangular quartz cuvette is simply held in a fixed position in close proximity to the detector apparatus. Stray unpolarised light is excluded from all measurements by means of sealing/covering the internal equipment setup from any sources of external light. A significant aspect for LD regarding multiple-component systems can now be understood from this. Since flow LD will only detect aligned particles within a sample, it makes analysis of detecting particle-particle and particle-medium interactions of selected particles much easier. Although spectra for a multi-component system can be extremely difficult to analyse because of peak overlapping, LD permits the investigation of how the peak patterns of exclusively aligned particles change with the other components within that sample while disregarding the actual spectral contribution from non-aligned components.

Examining DNA CD spectrum, we can see a very different result. Unlike LD, particle orientation is irrelevant however samples absorb circularly polarised light more when they have chiral elements in their structure. This is why the technique has been extensively used in the literature for the purposes of protein analysis since each secondary structure element gives rise to a distinct peak pattern[15]. The CD spectrum of an intact protein can therefore be used for identification since the spectrum should consist of the summation of the CD from each component (in the absence of interactions between components). Regarding DNA, the helix provides the chirality necessary for the signal and both the base composition and structural forms (since chirality is dependent on the structure) influence the resultant spectrum. This is why the technique has been extensively used in the literature for the purposes of protein analysis since each secondary structure element gives rise to a distinct peak pattern. The CD spectrum of an intact protein can therefore be used for identification since the spectrum approximately consists of the summation of the CD from each component. Within DNA the helix provides the chirality necessary for the signal and both the base composition and structural forms (since chirality is dependant on the structure) influence the resultant spectrum. Flow-LD essentially therefore determines if your sample molecule is capable of aligning under flow, and CD determines whether your molecule is 'helical' in nature.

In this work we will primarily be focusing on furthering the field of linear dichroism (LD) expanding on its applicability towards multiple-component systems with the aim of investigating biomolecular behaviour inside living cells. However why focus on LD instead of the alternative spectroscopic alternatives that are currently being used to examine various biomolecules (such IR, Raman or Fluorescence)? In contrast to existing techniques used to examine intact biomolecular samples both fields of dichroism spectroscopy shows several advantages along with a few drawbacks. If we compare these branches of dichroism to fluorescence spectroscopy, for the common example of examining proteins within these systems (as they can exhibit signals for each technique in different situations), this can be better understood. Firstly if we contrast against circular dichroism, although fluorescence spectroscopy requires the samples to be capable of fluorescence, proteins are inherently fluorescent due to

their aromatic amino acid groups. Since both are then capable of returning a spectrum specific to that protein to be analysed, they are very similar from that regard. The key feature is that they are both measuring different features of the biomolecule, either the fluorophore (fluorescent part of a particle) or the chiral structures. This can be observed when dealing with chiral biomolecules that are not inherently fluorescent since the particles must be tagged with specific dyes to be detected via fluorescence. Not only does this only permit the measurement of the concentration of dye, and thus the biomolecule, but it also inhibits further investigation of possible interaction between fluorophores within the sample, that a full spectrum from an inherently fluorescent sample like a protein would demonstrate.

Conversely a similar case can be made for circular dichroism for particles that are fluorescent yet not chiral. Since CD and fluorescence are so closely related, they are often used in tandem to examine the same samples. Linear dichroism however is different. Instead of simply detecting the presence of a particular type of particle, linear dichroism instead detects particles based on their behaviour, namely that they are capable of being aligned. What this means is that if we take a known fibrous protein such as Tubulin, fluorescence spectroscopy will be able to help us quantify how much of it is within the sample. However LD will not return any signal until the proteins have been induced to align in a particular fashion, it's primary disadvantage. Now instead of detecting purely the quantity of protein in the sample, instead the capacity for the protein to be aligned in this manner can be measured. Taken a step further, if the protein were to be embedded into another structure such as a membrane, and the membrane instead induced to align, now what could be analysed is not only how much the protein aligns itself in this environment but also specifically *how* it is aligned. Usually the more asymmetrical, or the higher aspect ratio the particle has the more effective. The main advantage therefore to LD is that it detects a very different phenomenon over another technique such as fluorescence spectroscopy.

Regarding current literature LD has already begun to find great use in this field of protein behaviour, regarding the differentiation between insertion and association of proteins with membrane surfaces[16]. However, when it comes to scaling up towards larger, more complex biological systems there has been minimal research conducted.

Precisely how LD spectra are presented for several systems of increasing levels of complexity (regarding the incorporation of multiple chromophore species) will be investigated in the following chapters and efforts made towards interpretation.

1.4 Biological system components

During the course of this work, analysis of multi-component sample systems were examined with increasing levels of complexity ideally culminating in a complete *living* biological cell. The capacity for LD to not only permit the analysis of kinetics as the cells react to changes in their environment, but also to be mild enough to leave the cells undamaged whilst being analyzed is another notable advantage. Unlike other techniques (several optical techniques are notorious for damaging biological tissues from exposure to extreme intensities of incident light[17]) this advantage permits far longer time-course assays to be conducted on intact biological samples. In order to reach this point however a series of model systems were used as stepping-stones to reach this stage.

DNA and Nucleotides

Nucleotides are one of the most common cellular components, which are present in almost every living cell in various different forms and geometries[18]. They are organic molecules consisting primarily of a sugar molecule (Ribose) attached to a nitrogenous base molecule of which there are 4 different types; Adenine, Guanine, Thymine and Cytosine (there also exists a 5th Uracil, an additional base observed in primarily single-stranded ribonucleic acid RNA). Each of these bases has a different aromatic (ring-shaped) structure in which their conjugated double-bonds permit the absorbance of light (via the excitation of electrons to a higher energy level[19]), essentially acting as a chromophore, and it is this feature that gives rise to the unique absorbance spectrum specific to each nucleotide base. Within cellular systems however these bases primarily exist as part of a larger macro-structure, in which polymers of these bases are formed (linked via phosphate groups) to form a polynucleotide chain. Two of these chains are bound together at the nucleotide bases, each selectively hydrogen bonding to one of the other types (A–G, C–T), and this double strand twists to take on the geometry of a

double helix. This structure is what is commonly known as DNA and is responsible for containing the genetic information necessary for the growth, development and functions within the given cellular system.

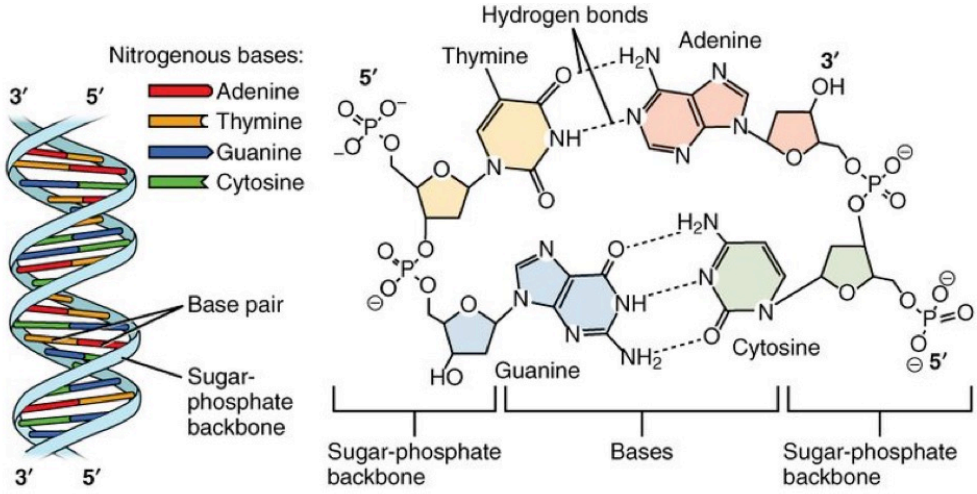

Figure 1.7: [28]Schematic depicting the structural elements comprising the primary 4 nucleotides, and the double-helical DNA structure that they form.

Various sub-structures of the DNA double helix exist in which features such as the direction of coiling, the tightness of the spiral and groove size can all be changed depending on various features (such as high-salt conditions) however the general double-helical geometry remains[20]. If the resultant absorbance spectrum is examined from a DNA sample it is now a composite of the relative weightings and intensities of the nucleotide bases within that strand. The fact that each base pairs exclusively with one other (Uracil is only observed in RNA as single strands and not double helices) simplifies this further since the relative quantities of a paired bases (and therefore the absorbance contribution) will always be identical.

This long fibrous geometry, in combination with a distinctive recognizable absorbance pattern is one of the primary reasons for why DNA samples are such a common example when considering LD spectra and why this spectrum has been examined in great detail in the literature. Its strong uniaxial nature greatly aids in the shear flow induction of orientation, and the reliable repetition of aligned chromophores across the strand gives rise to a correspondingly strong LD spectrum. With this

structure as a baseline, it then also permits the examination of various other molecules (usually too small to shear orient) via their binding to the aligned DNA strand[21]. The subsequent transition sign and LD intensity returns information regarding the orientation of these molecules, and subsequently binding behaviors, respective to the strand position and direction.

Proteins and Amino Acids

The second key component to be examined is that of amino acids, the essential monomers that comprise all proteins[22]. Each set of three nucleotide bases (a codon) on a strand of DNA relates to a specific amino acid that the cell can produce from that piece of DNA. Although there exist 20 standard types that commonly appear in eukaryotic DNA, and hundreds of non-standard variations commonly found in other biological systems (such as archaea or bacteria), only 4 of these standard types are capable of absorbing light and thus give rise to a spectrum. Similarly to DNA, each of these 4 amino acids (tyrosine, phenylalanine, tryptophan and histidine) contains an aromatic ring in its structure that permits it to act as a chromophore[23].

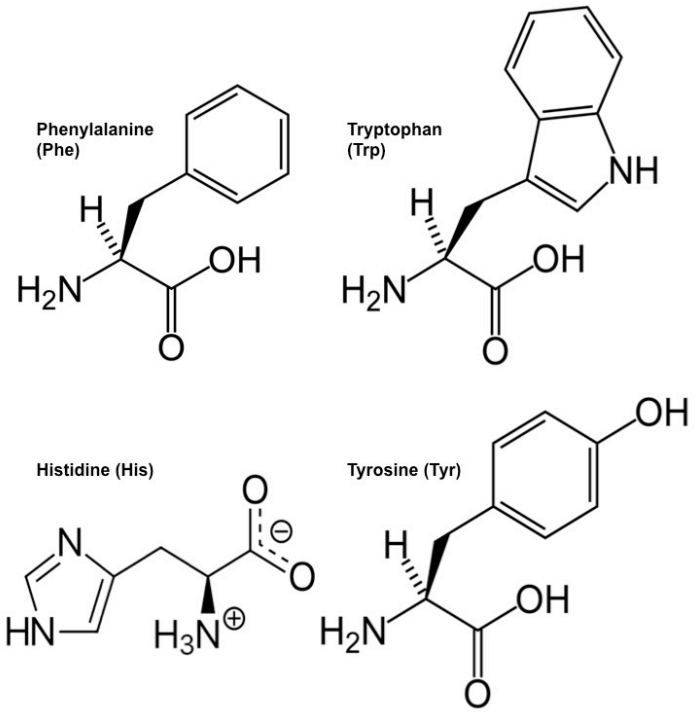

Figure 1.8: Molecular structure of the four standard aromatic amino acids.

However of these, Histidine does not absorb as strongly in the ~280nm UV-Vis region (due to its nature as an imidazole ring), and as such is of lesser importance in this work. The primary structure of a protein is formed from a chain consisting of numerous amino acid monomers; the corresponding absorbance of this chain is therefore a composite of the relative contributions from each type of aromatic amino acid. Proteins naturally fold themselves into what is defined as their 3D secondary structure, based primarily on the patterns of hydrogen bonds present between the amino acid backbone. This is most commonly observed in the forms of alpha helixes and beta sheets, although variations have been observed such as polyproline helices, each of which absorbs in the low UV-Vis ~190–220 region[24,29]. When numerous of these substructures fold together (based on numerous factors such as hydrophobic, ionic, disulphide bonds etc.) the overall protein tertiary structure is formed, then potentially a quaternary structure when several of these tertiary sub-units fit together.

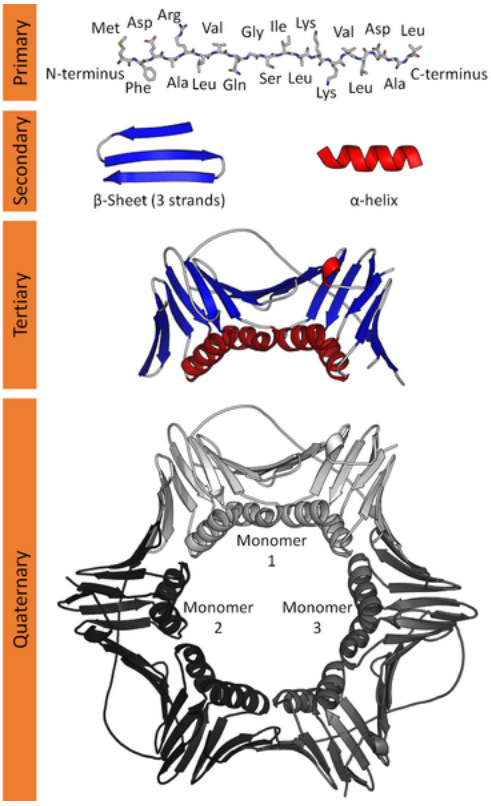

Figure 1.9: [30]Diagram of protein structure, using PNCA as an example.

When considering LD, the corresponding signal is based primarily upon the protein content of the secondary structure components and their relative orientation within the protein. The peak wavelength, transition sign and intensity are variable dependent upon which structure is examined, the quantity of each structure and the orientation distribution relative to the protein position[31].

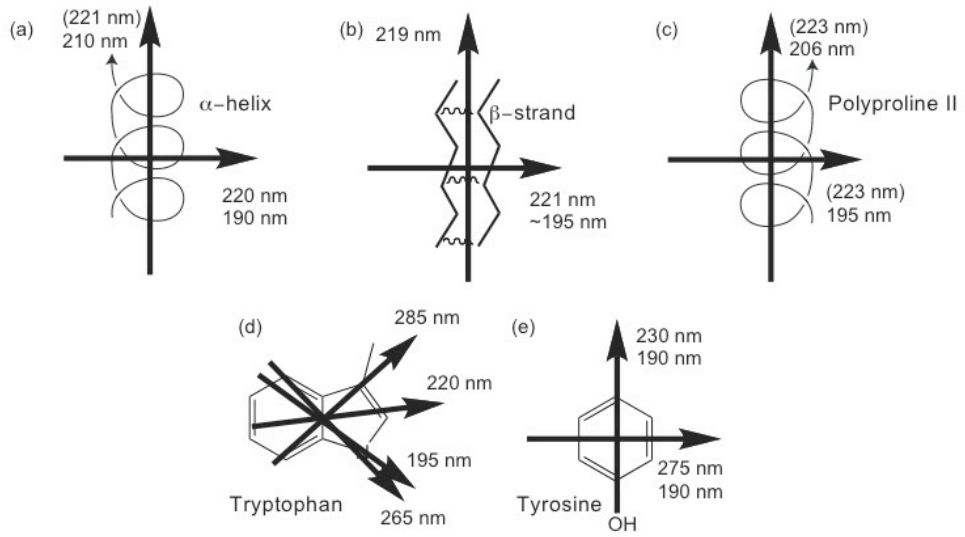

Figure 1.10: [31]Graphical representation of protein secondary structural elements and their absorbance contributions with regards to their orientation relative to incident light direction.

Liposomes and Lipids

Another common biological component to be considered is that of lipids[25]. These are long hydrocarbon chains, essentially fat molecules, and are most commonly linked to phosphate groups via a glycerol molecule to form what are known as phospholipids. These molecules possess the regions of both hydrophilic (charged phosphate head group) and hydrophobic (fatty acid tail) character, an amphiphile. Due to this property when in solution these lipid molecules tend to aggregate in order to minimize contact with the surrounding aqueous environment, forming a bilayer with the fatty acid tails self-associating. This can form as either as numerous small spheres with tails facing inwards (micelle), a sheet (lipid bilayer), or a hollow bilayered sphere (liposome). The latter of these is a close approximation for that of the cell membrane that is found in all cell types.

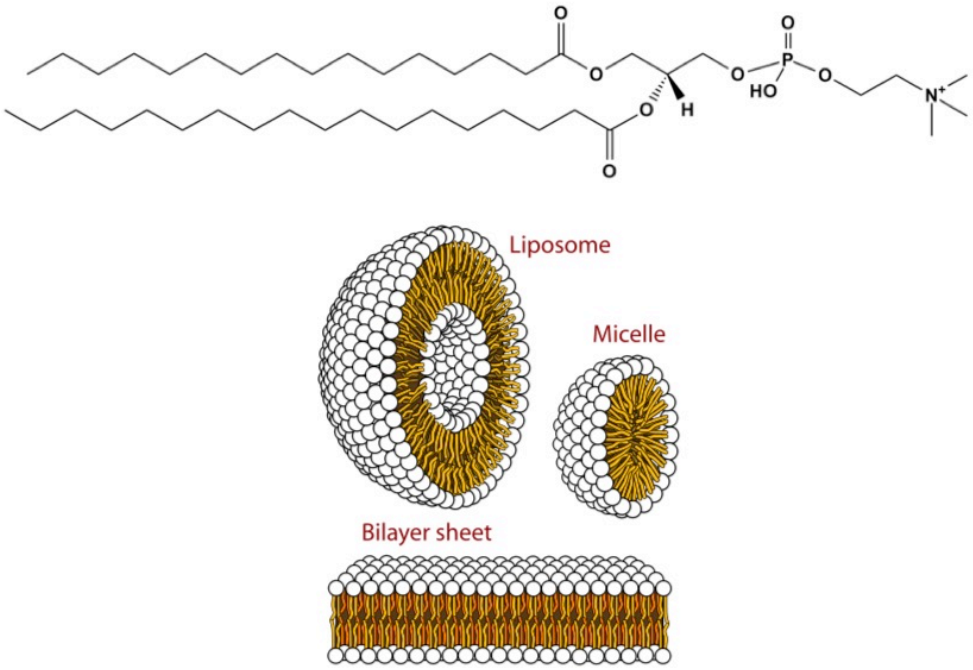

Figure 1.11: Molecular structure of phosphatidylchloline (top) and the associated macromolecules lipid structures formed (bottom)

Although the lipid membrane itself does not strongly absorb light in the UV-Vis wavelength region, it is generally a highly flexible structure that is capable of deformation and alignment under shear flow forces. Since it is such a core structural component, depending upon the cell in question, a vast range of different components are capable of binding to this structure in various manners. Of these the most common tend to be molecules that strengthen and stabilize the membrane (e.g. cholesterol) or membrane associated proteins[25]. These proteins can either be simply bound to the outer membrane, integrated within it or can even form a web-like structure across the inside face of the membrane (cytoskeleton). Of course further components can also bind to these structural proteins, such as sugars (to form glyco-proteins). Any of these associated components that contain chromophores that bind to this membrane can 'inherit' any orientation that the membrane demonstrates un-der flow, returning a corresponding LD signal. Similarly to the case observed for DNA binding components, the intensity and transition sign of the LD contribution from each component returns

information regarding the quantity and orientation of its binding relative to the cellular position.

1.5 Spectral artefacts and scattered light

Another aspect of this work involves the optimisation of spectral analysis and elimination of possible sources of error. These sources either involve errors in experimental setup, e.g. incorrectly calibrated polarisers or an incompletely sealed system that permits stray light to enter the setup or sample issues such as the influence of light scattering which is not as easily characterised and eliminated, and as such to date little research has been conducted regarding the removal of the influence scattered light on *experimental* spectra. Although several fields of theory have been developed discussing the calculation of scattering intensity (and its related angular distribution) for a given particle size and geometry, application of these theories (namely Rayleigh-Gans-Debye and Mie) to improve real experimental data has so far not conducted with any success. Only the simplest approach that of the curve fitting of a non-linear regression to the spectral dataset has been implemented[26].

$$\tau_{LD} = \alpha\lambda^{-\omega} \tag{1.1}$$

In this relationship, the intensity of the scattered light that contributes to the resultant LD spectrum (τ_{LD}), or as otherwise known as the turbidity dichroism, has a dependence on the wavelength of the incident light (λ) to the power $-\omega$ (both α and ω are constants).

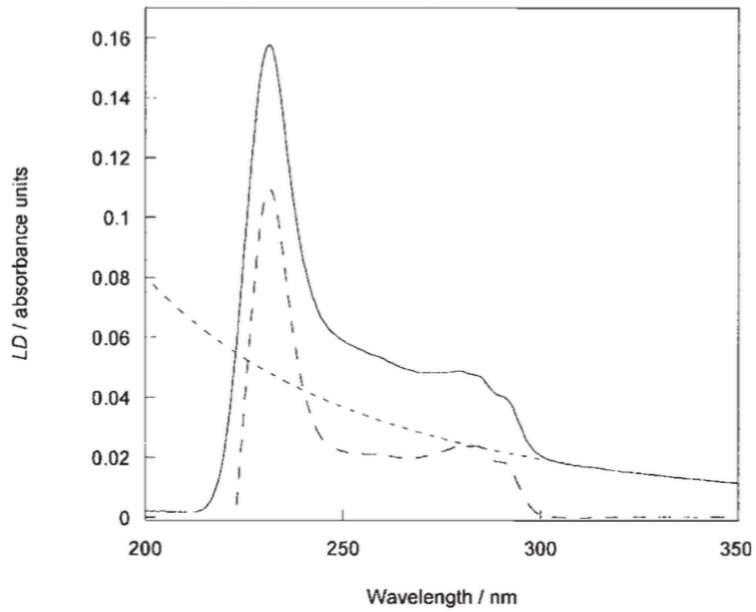

Figure 1.12: [26]Representative flow LD of intrinsic microtubules and the corresponding scattering subtraction.

As one can see this approach on first glance appears quite successful, however, there are several issues with this approach, not immediately apparent present in both approaches to scattering correction using this relationship found in the literature[26]. The first tends to be rather simple, usually that of an approximation, where the correct values for the equation parameters are estimated and iterative repeats are conducted to reach the closest approximation possible. This is possibly the better approach to determine the scattering contribution across the entire spectrum; however, since the scattering relationship rarely perfectly follows that of the regression obtaining very close matches for the scattering under particular peak species can be difficult. Alternatively, the parameters of this scattering equation can be calculated via fitting a non-linear curve to wavelength ranges of the spectra without any absorbance (and so any detected signal should be derived exclusively from scattering) in order to determine the equation parameters, and extrapolating across the entire wavelength range of the spectrum. In contrast, the previous method this approach can lead to more precise fits for spectra with either a single or closely populated peaks since the subsequent accuracy of a fit for a particular peak (or peak distribution) is related to the proximity of the initial fit to that peak wavelength. A further issue is that ideally a

wide wavelength range on either side of the peaks in question would be used to examine the scattering contribution, and when dealing with peaks exclusively at high wavelength regions (within the limits of apparatus) this approach is not too unreasonable however several biological samples (e.g. DNA/protein) have peaks close to the limits of detection which ensure that generally only the wavelength range above that of the peak species can be used to determine the fitting. In any case, this approach leads to close fits for simple spectra, involving minimal peak species (permitting a close proximity fit), however the more that the peak species are spaced across a spectra the more the exponential fitting relationship begins to under-fit (usually presenting as a scattering elimination for the highest wavelength region, with a re-emerging scattering trend at low wavelengths, as shown in Fig 1.12). The fundamental flaw is that for a close fit for a particular peak species it inevitably leads to a worse fitting for other peak species within the same spectrum, precisely because it is calculating the scattered spectrum solely from a localised range.

Since the dependence of scattering on the particle size and geometry has been clearly demonstrated in several fields of theory it infers that the opposite approach should also be possible, that instead of either relying on fitting this non-linear relationship to the experimental data, it should be possible to be calculated independent of the experimental spectrum (given sufficient particle and system parameters), and then subtracted from that spectrum. Conversely it should then also be possible to determine particle characteristics from examining the corresponding scattering curve within for a given absorbance, CD or LD spectrum. Although work has been conducted in this field previously[27] (e.g. Dynamic light scattering, DLS, for the purpose of determining particle size), this approach would allow a far better understanding of particle kinetics during the course of an experiment particularly one that can be characterised via another spectroscopic technique like LD. It therefore seems lacking that the most popular approach currently being applied (commonly found in the provided software within some spectroscopic equipment) is that of a basic linear regression fit, from which no details regarding particle geometry can be ascertained. Although work has been conducted to derive the basic theories for particles of various sizes and shapes (mostly covered by Rayleigh and Mie scattering

theories)[32], little to no research has been successfully conducted with regards to the practical application of these theories toward experimental data. Therefore, the following aspects of this work are to examine the current fields of scattering theory, determine the restrictions to each method and suitability towards the physical parameters related to cellular samples. To complement this, an investigation was conducted into the application of these fields towards the analysis of experimental data and the development of modifications to the existing theory to improve the fitting of scattering curves.

Chapter 2: Theoretical scattering approaches

In the field of spectroscopy collection of accurate and reliable data is of paramount importance. Be it absorption, fluorescence or dichroism spectroscopy, distortion of the desired signal is a significant problem that can occur from a variety of sources. By precise preparation of sample and data collection, outside sources of error can be minimized however what can be done about inaccuracies that come from within the sample? We are referring of course to phenomena such as scattering of the incident light, leading to a misrepresentation of the amount of light striking the subsequent detector. Unfortunately, this is not the sole contributor, other occurrences (such as stray light from an imperfect monochromater) can still occur, however, light scattering is the most pertinent and removal is key to greatly improving quality of a variety of spectral data. Light scattering is typically thought of simply as incident light that strikes a particle and then 'bounces' off, scattering in all directions[33]. In actuality, when a particle is polarisable and is exposed to an incident electric field the electron fields within the particles component molecules are disturbed with the same frequency as that of the incident wave. This results in a separation of charge within that molecule, known as a dipole moment, with the magnitude of that moment being proportional to that of the incident field. In addition the more polarisable the particle is, (i.e. the tendency a particles charge distribution is displaced by an incident electric field) the higher the magnitude of the dipole moment, and this induced dipole moment radiates light in all directions around the particle.

The influence of scattered light within spectroscopic data analysis like linear dichroism is commonly treated as unwanted noise that inhibits any quantitative analysis of experimental data, due to the inability to accurately calculate the scattering contribution and remove it from the polarised absorbance data being examined. However for years alternative fields have been utilising light scattering to investigate particulate samples[27]. One popular example DLS (Dynamic Light Scattering) used in

order to determine the size distribution of particles within a solution commonly used to determine the polydispersivity of prepared solutions. Various instruments and techniques have been used over the years to analyse this particle dependant scattering intensity and to investigate a wide variety of parameters related to the particle[35]. Firstly, exclusively concerning the particle polarisability (in other words its potential to form instantaneous dipoles, and thus scatter light), it is dependent on particle features such as refractive index and molecular weight. In addition to this, features such as particle volume, size and structure further influence this scattering intensity[32,33]. Even when dealing with non-spherical particles, this size dependence instead can be used to determine the radius of gyration of such a particle under the assumptions of random rotation of all particles within a homogenous solution. Then when considering the particulate solution as a whole, further features such as osmotic pressure can also be analysed and being derived from particle concentration can result in the number average molecular weight. Theoretically since all these parameters are being used to determine the scattering contribution within any given spectra, by application of scattering theories the scattering contribution be accurately calculated for given particle parameters, and used to remove scattering from their spectra[32]. Not only this, but with sufficient input parameters, by fitting calculated scattering curves to experimental LD unknown particle parameters can be determined.

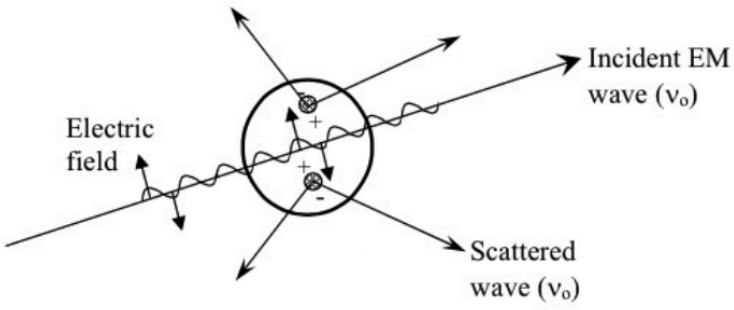

Figure 2.1: Illustration of the light scattering produced by an induced dipole moment after exposure to an incident electromagnetic wave (*Vo* relates to the frequency of the incident light)[33].

2.1 Current application

Regarding formal scattering theory there are two established methods of dealing with spherical particles: classical Rayleigh and Mie theories[32]. The former has a pair of size restriction criteria, so is only appropriate for small, non-absorbing particles:

$$ka = x \ll 1 \tag{2.1}$$

The size parameter (x) corresponds to the product of the particle radius of gyration (a) and the parameter k is defined as $2\pi / \lambda$ where λ wavelength of the incident light. In essence this criteria is fulfilled provided that the particle is much smaller in size than the wave- length of the incident wave (some literature sources further state upper values to be around 5 percent of incident wavelength), for example in the UV-Visible light range (200−700 nm) this work takes place in this would equate to about 10−35 nm. This criterion is in order to make the following assumption that the external field being applied to the scattering particle can be treated as a homogenous field. A secondary condition, Eq 2.2, is that the field applied to the particle should penetrate into and through the particle so quickly that the state of polarisation that the particle is subjected to can be treated as static. In other words, the size of the particle should be much smaller than the wavelength of incident light within the particle (λ/m, where m is the relative refractive index of the particle in contrast to the surrounding medium).

$$|mx| \ll 1 \tag{2.2}$$

If this condition is broken the wave may pass through the particle slow enough that the incident wave is phase shifted and a gradient of phase is established between the inner and outer areas of the particle (this effect is known as the resonance region). The influence of this resonance region on the incident wave as it passes through the particle can also give rise to a range of other systems (e.g. magnetic dipole radiation, quadrupole radiation). The increase in complexity and difficulty in prediction has led to this criterion being upheld as much as possible (theories for non-spherical particles like ellipsoids have not even been developed yet). The latter, Mie theory, has the

advantage of being capable of dealing with particles of much larger sizes than Rayleigh theory however is primarily restricted to dealing with spheres[32]. Although modifications to the theory have been made in the literature to adapt it for non-spherical particles the capacity to deal with different polarisations of incident light with regard to the position and shape of these non-spherical particles has not been fully explored (since the theory is essentially designed for spheres, which have no preferential orientation). This lack of capacity to deal with scattered light from oriented non-spherical particles has excluded it for the most part in this work due to the inapplicability of the theory with regards to LD and CD.

However, what is most commonly used (and unfortunately often incorrectly) is not traditional Rayleigh theory but a much-simplified alternative known as the Rayleigh-Gans-Debye approximation. By making a pair of assumptions on the particle in question the subsequent calculation of the scattering fields become much simpler and larger particles can be examined. The first assumption is that the refractive index *m,* relative to that of the surrounding medium, is close to 1. Secondly that the 'phase shift' of the incident wave when passing through the particle is small enough to have a negligible influence, a being the particle radius of gyration. Normally the restriction in Rayleigh scattering theory is that the particle must be much less than the wavelength of the incident light (λ). However with both these assumptions in place the restriction on particle size is now no longer than the particle must be $\ll \lambda$ but instead that it may be $\ll \lambda/|m-1|$ which, depending on the particle refractive index, can permit much larger particles to be modelled. The current application of scattering theory in the field of spectroscopy, as previously mentioned, is that of a simple non-linear regression fit to a given spectra to remove the scattering 'noise', Eq. 1.1, based off the fundamental equation underlying Rayleigh theory:

$$I = \frac{I_0 F(\beta, \varepsilon)}{k^2 r^2} \tag{2.3}$$

The intensity of the scattered light is dependant on that of the incident light (I_0) and the distance of the scattered light (r) from the point of origin. The function F is dimensionless expression used to describe the particle shape and orientation with

respect to the incident light axis and its polarisation state (β and ε correspond to the polar and azimuthal angles of the scattered light propagation vector in relation to the incident light axis). However, when dealing with spherical particles or under conditions where the polarisation of incident light is not a relevant factor this expression can be significantly simplified. As will be detailed later on, within the derivation for F contains a dependence of the scattering on k^6. When taken into account with Eq 2.3, the a-typical Rayleigh scattering inverse wavelength dependence of k^4 can be observed. Since k equates to $2\pi / \lambda$ this gives rise to the resultant negative exponent for wavelength dependence as seen in Eq 1.1. This negative exponent then can be considered to essentially relate to $-\omega$ in Eq 1.1, resulting in $\omega = 4$ for Rayleigh scattering. An interesting aspect to note is that regarding the alternate Mie theory the exponent of k remains at a constant value of 2 instead, independent of particle size (or orientation since traditional Mie deals exclusively with spheres). Due to this, application of this approach should only be used for spherical particles within the Rayleigh/RGD size regimes (and it is often here that it is most commonly misused thanks to the influence of variable particle refractive index).

Unfortunately, although apparently successful, application of the common non-linear regression fitting approach, Eq. 1.1, can also be demonstrated to conflict with this theory.

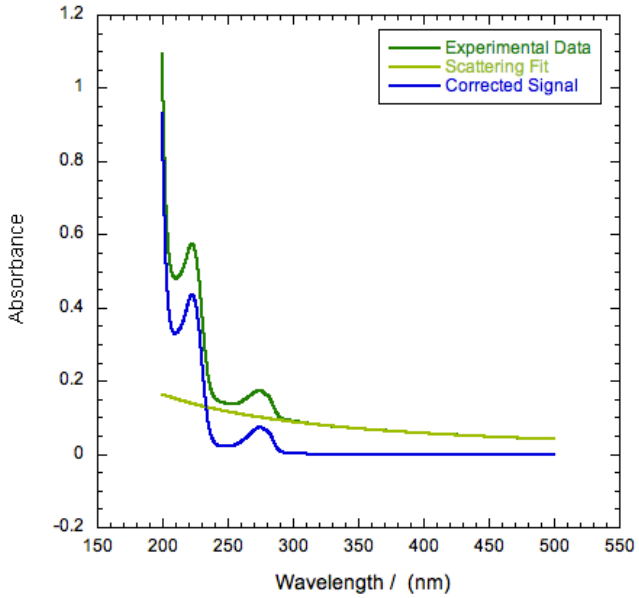

Figure 2.2: Tryptophan UV-Vis absorption spectrum with associated scattered fit via the non-linear regression approach [0.1 mg/ml, pathlength: 1mm]. Scattering was calculated from the 310-500 nm region of non-absorption.

Tryptophan is a perfectly suitable particle for scattering assays such as this, although having a high refractive index (1.485) it's radius of gyration is well under 1 nm, and so it falls easily within even the stricter Rayleigh constraints (randomly spinning tryptophan molecules can be considered to be spherical, provided the radius of gyration is determined). At sufficient concentrations the amino acid demonstrates a distinct scattering pattern that should be able to be fit using the simple non-linear regression approach, (Eq. 1.1 substituting $\omega = 4$). The method to applying this approach is generally to scan over a wider range of wavelengths (outside of known peak absorbance regions) to select a region in which there is no significant peak distribution caused by the particle absorbance. Theoretically, a detectable signal at those wavelengths could only be caused by scattered light (or other artefacts such as stray light, which ideally has been minimized in an optimal machine setup). The non-linear regression is then fit to the longest wavelength region adjacent to the absorbance peak species for the optimal fit. The problem is demonstrated in Fig. 2.2 where the troughs between peaks, which should approach the baseline since minimal to no absorbance is occurring, are moving further up in absorbance intensity instead. Essentially the inadequacy of the fit becomes greater as the wavelength distance between a given absorbance peak grows in relation to the wavelength range the fitting was taken place.

In tandem the exponent of *k* when fitted is actually 1.51 instead of the expected 4. Although initially the fit may appear good, upon closer inspection it deviates strongly from the expected Rayleigh/RGD theory without a definite reason, and because of this causes a corresponding lack of 'long-distance' fitting. This is not unusual, and similar behaviour has been characterised previously in related literature[26] regarding scattering from Tubulin fibres, resulting in exponents of *k* of between 2.8-3.5. Even when attempting to stick to established theory, when particles are approaching the limits of their size criteria, deviations from the dictated wavelength dependence become apparent. A practical example of this can be seen this by way of a

substance commonly used in order to introduce and demonstrate the effect of Mie scattering in solutions (or otherwise used to analyse changes in solution refractive indices), coffee creamer. This essentially is a spherical particulate solution that is usually outside of the Rayleigh size regime, (but can be a wide range of sizes, such that analytical tools such as DLS are necessary to determine individual suspension size distributions).

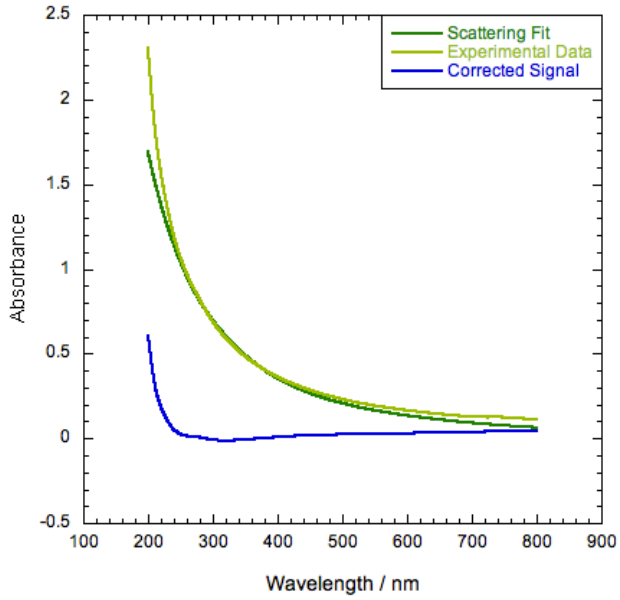

Figure 2.3: Coffee Creamer 2.5 g/ml UV-Visible absorption spectrum overlaid with that of the predicted scattering from Mie-Sphere scattering code, particle radius: 255 nm.

Firstly via alternate analysis via DLS we can determine an average radius of gyration of the particulate solution to be around 255 nm. One of the principal components of particulate products like this are fats, (coconut oil in this case) with a refractive index of around 1.445-1.45[34]. Taking this relative refractive index (1.445 against 1.333 of distilled water) and assuming that like Rayleigh theory that the upper limit for the particle size is 5% of $\lambda / |m - 1|$. Under these conditions the limit would range from 119-476 nm between the incident wavelength range of 200-800 nm. From this we can determine that the particle is hovering around the outside limits of the RGD application, and as an alternative Mie theory was applied. As we can see the fit is quite close, demonstrating the accuracy of using an approach involving a fit that involves an exponent of k of 2. Unfortunately, this does present some problems, firstly that the

particle is not wholly outside of the constraints of RGD theory and yet fits closely with the relationship of Mie to the exponent of k ($\omega = 2$). In addition we can see that it is not a perfect fit and that the fit demonstrates deviation at extremes. Although clearly if this relationship were to follow that dictated by Rayleigh ($\omega = 4$), the overall fit would be far from appropriate. However, an interesting final point to note that although neither Mie nor RGD can perfectly fit the data if ω were to be increased slightly the fit should become steeper and more closely represent the experimental data. For cases such as this, at the limits of the size constraints between two regimes of theory the exact value of this k exponent of the scattered light seems to become vague.

2.2 Rayleigh-Gans-Debye scattering

By direct contrast to experimental data we have shown that both the current scattering correction approach and also the accuracy of the theorized fit from more complex approaches (RGD, Mie), regarding particles close to the postulated size restrictions, are currently lacking. The optimal situation therefore would be to modify the existing theories within the upper size boundary region between RGD and Mie, such that not only does it more accurately represent experimental models but also can be practically applicable in place of the non-linear regression. Since a primary focus of this work is dealing with scattering produced from LD, the differential interactions of scattered light with linearly polarised planes needs to be fully understood in order to make any reasonable modifications (it also would be necessary to understand the resultant scattering intensities for any other spectroscopic fields involving light polarisation). With this in mind, it is of more use to expand primarily upon RGD theory since Mie theory deals primarily with the interaction of non-polarised light spheres, whereas RGD theory has been developed more towards dealing with varied particle shapes and orientations relative to the incident polarisation. Following van de Hulst, we write (see below) in terms of the difference in the squares of the polarized electric fields of the scattered light (E). So we need

$$I_\tau = I_Z - I_Y \propto |E_Z|^2 - |E_Y|^2 \tag{2.4}$$

A general definition by Van de Hulst[32] of the electric field from light scattered from a small particle is defined as follows in relation to an amplitude function *S*, that describes the interaction between the state and direction of the polarised incident light and the orientation of the particle (inversely proportional to the distance *r* from the induced dipole moment). This is then taken into account in relation to the electric field of the incident light described as a spherical outwardly directed wave with *z* and *w* corresponding to the particle-origin distance and angular frequency.

$$E = S(\beta, \varepsilon) \frac{e^{-i(kr-kz)}}{ikr} E_0 \tag{2.5}$$

This is the key part of the general Rayleigh formula, Eq. 2.3, in which the *F* function needed to be expanded upon. As previously mentioned before this function essentially denotes the interaction between the state and direction of the polarised incident wave and the orientation of the particle but is independent of *r*.

$$I_{sca} = \frac{S^2(\beta, \varepsilon)}{k^2 r^2} I_0 \tag{2.6}$$

2.3 Derivation and calculation of turbidity linear dichroism

In order to understand the interaction of polarised planes of incident light with the particle we first need to detail the multiple coordinate systems necessary to express the overall system. Firstly it is necessary to equate the traditional laboratory fixed axis system (*X,Y,Z*) as used in LD; in which normally we define the incident light direction as *X* and the perpendicular and parallel polarisations of that light *Y* and *Z*, to that of a molecular axis system (*x,y,z*). In this we similarly define *x* as the light propagation direction, the *z* axis is that of the particle orientation axis as well as that of the flow orientation axis and *y* is usually taken to be the axis perpendicular to *z* that is best oriented. If the orientation is uniaxial then *x* and *y* are equivalent. Exclusively considering these coordinate systems, we can define the particle orientation in terms of its polar and azimuthal (with regards to the reference *X* axis) angles θ and φ respectively. It should however be noted that this definition of θ is different from the

standard LD use where it is often used to denote the angle between *z* and *Z*). Next in order to calculate the amplitude function *S* we need to consider the scattering vector produced by the induced dipole moment, in terms of its corresponding scattering plane defined by a further axis system (*X, Y', Z'*). In this case *X* is again the direction of the incident light (which is the same as the *X* of the laboratory fixed axis system), *Y'* is perpendicular to the plane defined by *X* and *Z'* the propagation vector of the scattered light (**s**, Fig. 2.4), and makes a right-handed axis system. The relationships between the axes systems required for our calculations and the angular definitions are illustrated in Fig. 2.5. Of particular note are the angles used to define used to define **s**; β the angle between **s** and *X* (polar angle), and η the angle of rotation around *X* that transforms (*X, Y', Z'*) to (*X,Y,Z*).

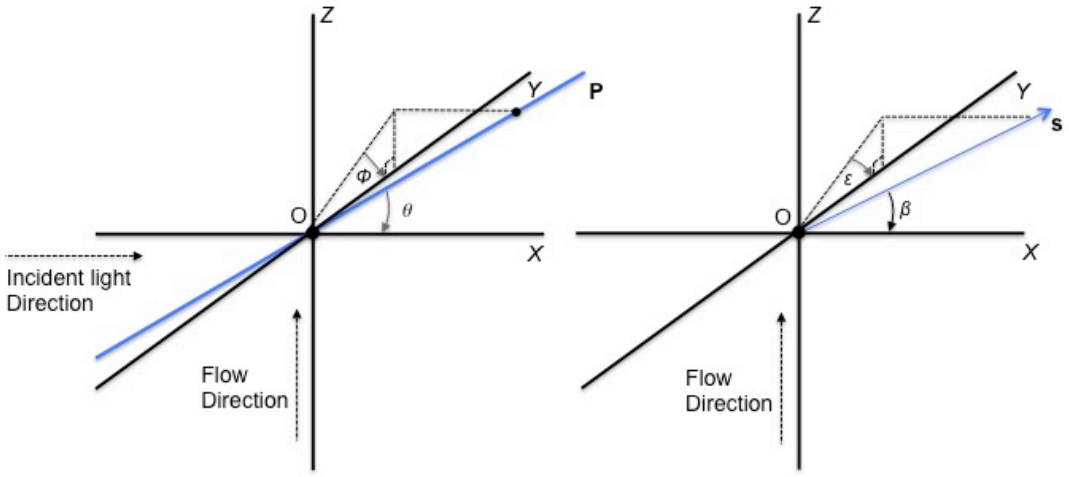

Figure 2.4: Schematic for an LD experiment outlining the scattering vector s and associated polar and azimuthal angles for particle orientation axis **P**(θ, ϕ), and propagation vector **s**(β, ε).

Although the values of I_Z and I_Y, Eq. 2.4, depend on the dynamic polarisability tensor components, retaining the generality of the anisotropic polarisability leads to complex equations that we would end up simplifying in order to parameterize the required calculations using our experimental data. We therefore assume the polarisability of our particles are isotropic with value α (notably for liposomes where the molecular components of the scattering particle are a fairly uniform shell, this is reasonable). For

other systems, where the orientation is either poor or extremely high, the parameterization we introduce below accounts for the anisotropy.

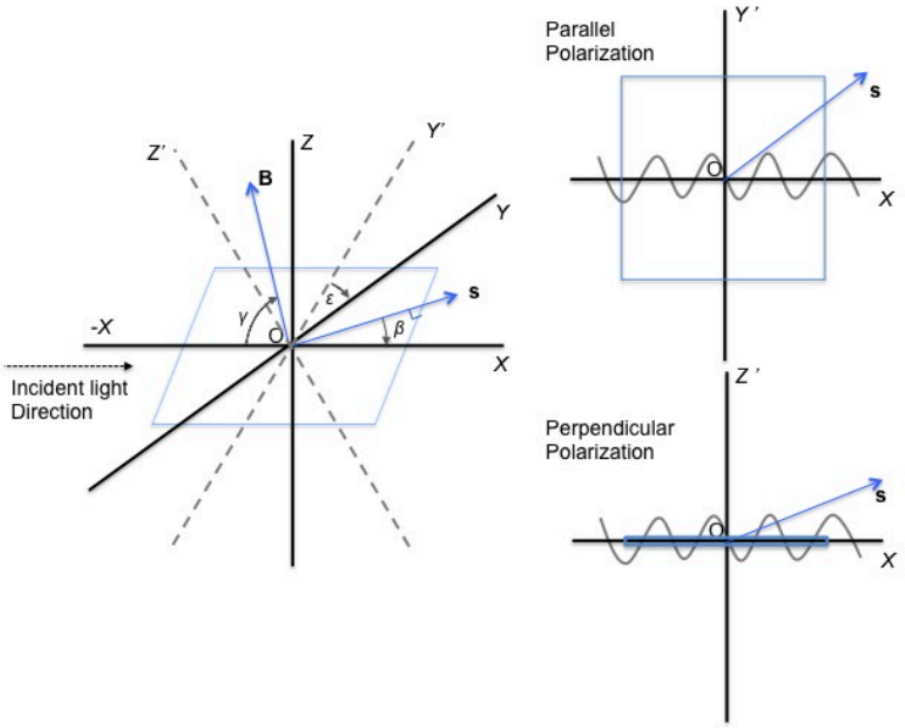

Figure 2.5: Schematic diagram of the scattering plane (*X, Y', Z'*); (a) Plane orientation with respect to the initial *X,Y,Z* coordinate system. (b) Scattered wave polarization in relation to the initial (*X, Y, Z*). (b) Scattered wave polarization in relation to the τ_{LD} axis system. The bisectrix of **s** is given by angle γ bounded by *XOB*.

Following the literature we express the electric field components of the scattered light in terms of scattering amplitude functions S_i (which depends on the scattering angle, particle geometry and polarisability) and the electric field of the incident radiation expressed in terms of the (*X, Y', Z'*) axis system where E is the electric field vector of the scattered light, and E_0 is the electric field vector of the incident light.

$$\begin{pmatrix} E_{Y'} \\ E_{Z'} \end{pmatrix} = \begin{pmatrix} S_1 & S_4 \\ S_3 & S_2 \end{pmatrix} \frac{e^{-i(kr-kz)}}{ikr} \begin{pmatrix} E_{Y_0'} \\ E_{Z_0'} \end{pmatrix} \tag{2.7}$$

In the literature, Eq. 2.7 is commonly found without any explanation of the terms. Since our goal was to calculate the scattering for oriented rods or ellipsoids a level of understanding is required. This function is constructed as a matrix of four values based on a set of values known as the Stokes parameters, commonly used to define the polarisation state of electromagnetic waves. This matrix permits the calculation of amplitude in any given direction as functions of β and ε. For small (compared with the wavelength of light) isotropic particles, within the RGD approximation only the amplitudes S_1 and S_2 are non-zero and equate to the polarizations perpendicular and parallel to the scattering plane respectively (Fig. 2.6). (Note we have chosen to express the S matrix inverted compared with much of the literature so Y and Z components of vectors appear in the usual order.) For this case the S matrix may be expressed as follows:

$$\begin{pmatrix} S_1 & S_4 \\ S_3 & S_2 \end{pmatrix} = ik^3 \alpha R(\beta, \varepsilon) \begin{pmatrix} 1 & 0 \\ 0 & \cos\beta \end{pmatrix} \tag{2.8}$$

Considering the theory laid out in related works[32,36,37], it follows that: k accounts for the S_i amplitude wavelength dependence; α is the isotropic polarisability of the particle relative to its refractive index (m); R is described variously as the inference function, form function, or form vector, which accounts for particle orientation and geometry (we will be referring to it as form function in this work). Since RGD scattering treats every volume element as an independent scatterer, all the waves scattered in a particular direction (β,ε) interfere because of their different origins in space. $R(\beta,\varepsilon)$ therefore represents a phase factor to correct for these interference effects, relating the phases of all the scattered waves to a common origin. For the liposome experiments

considered later on in this work derivations of the both R and α require modification of literature work in order to account for the hollow nature of the particles. For the LD experiment, we need to determine the scattered light vector in the ($Y'Z'$) coordinate system for incident light polarized along either Z or Y. The vectors are (where the subscripts denotes the axis system and the argument denotes the original polarization)

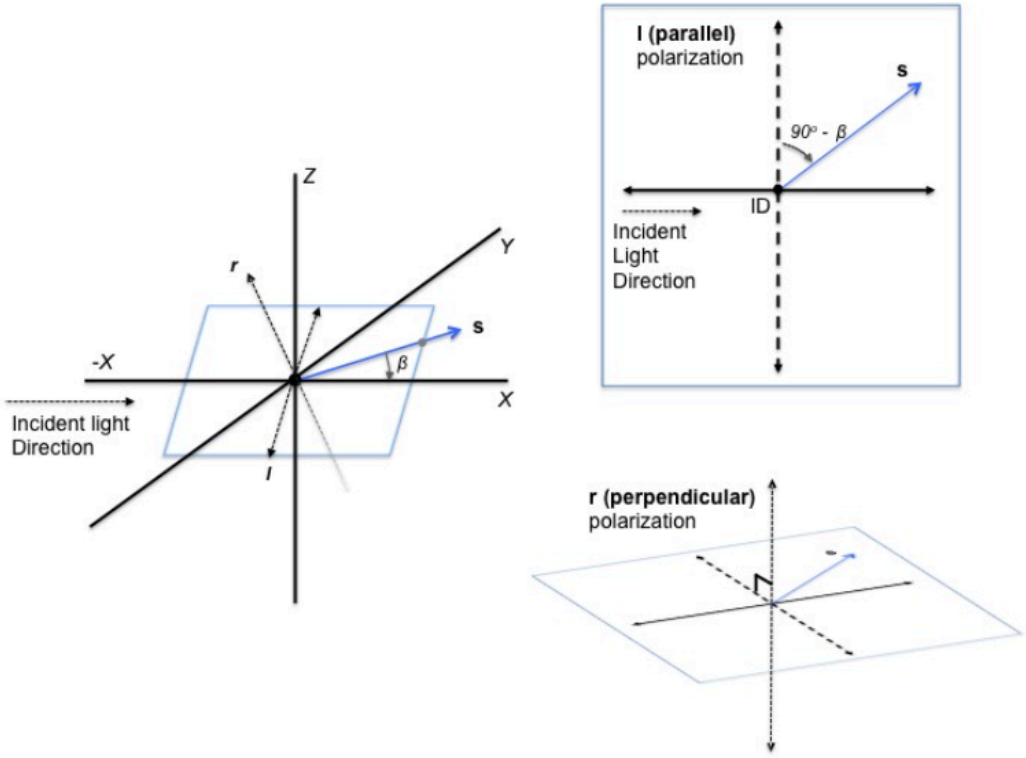

Figure 2.6: Schematic outlining the plane of reference and the origin of the values present within the S matrix; l and r denote the parallel and perpendicular unit vectors with regards to the plane, ID corresponds to the origin of the induced dipole moment as the incident light strikes the particle.

These following transformation matrices transform the (YZ) coordinate system to ($Y'Z'$).

$$\begin{pmatrix} 0 \\ E_{Y_0'}(Z) \\ E_{Z_0'}(Z) \end{pmatrix}_{XY'Z'} = \begin{pmatrix} 1 & 0 & 0 \\ 0 & \cos\varepsilon & \sin\varepsilon \\ 0 & -\sin\varepsilon & \cos\varepsilon \end{pmatrix} \begin{pmatrix} 0 \\ 0 \\ 1 \end{pmatrix}_{XYZ} E_0 \tag{2.9}$$

$$\begin{pmatrix} 0 \\ E_{Y_0'}(Y) \\ E_{Z_0'}(Y) \end{pmatrix}_{XY'Z'} = \begin{pmatrix} 1 & 0 & 0 \\ 0 & \cos\varepsilon & \sin\varepsilon \\ 0 & -\sin\varepsilon & \cos\varepsilon \end{pmatrix} \begin{pmatrix} 0 \\ 1 \\ 0 \end{pmatrix}_{XYZ} E_0 \tag{2.10}$$

From equations 2.5-10 for N particles it then follows that:

$$I_Z = \frac{Nk^4V^2\alpha^2I_0}{r^2} R^2(\beta,\varepsilon)\left[\cos^2\varepsilon+\cos^2\beta\sin^2\varepsilon\right] \tag{2.11}$$

$$I_Y = \frac{Nk^4V^2\alpha^2I_0}{r^2} R^2(\beta,\varepsilon)\left[\sin^2\varepsilon+\cos^2\beta\cos^2\varepsilon\right] \tag{2.12}$$

Next we need to account for the fact that during shear flow not all particles will align perfectly with the flow direction, in practice only a few percent of particles will align sufficient to produce an LD signal. To account for this orientation distribution *f(θ,φ)*, (which leads to the more commonly used orientation parameter *S*), of the particles in the sample we need some way to describe it. As outlined in the next section we implement the Peterlin distribution following McLachlan *et al*[38]. Bringing these aspects together we may now write

$$\tau_{LD} = \int_0^{2\pi}\int_0^{\pi}\int_0^{2\pi}\int_0^{\pi} f(\phi,\theta)(I_Z-I_Y)\sin\beta\,\mathrm{d}\beta\,\mathrm{d}\varepsilon\sin\theta\,\mathrm{d}\theta\,\mathrm{d}\phi \tag{2.13}$$

Another condition is that for the majority of spectroscopic setups, and almost exclusively for LD, there is a localised detector positioned after the sample. As mentioned previously any scattered light that enters this detector will be treated as transmitted light and disregarded. Since this is the case we need to adjust the above formula to account for this solid angle of non-detection that is present between the induced dipole moment and the detector aperture (μ).

$$\tau_{LD} = \frac{1}{4\pi(\cos\mu+1)} \int_0^{2\pi} \int_0^{\pi} \int_0^{2\pi} \int_{\mu}^{\pi} f(\phi,\theta)(I_Z - I_Y)\sin\beta \, \mathrm{d}\beta \, \mathrm{d}\varepsilon \sin\theta \, \mathrm{d}\theta \, \mathrm{d}\phi$$

(2.14)

2.4 Parameters for τ_{LD} calculation

In order to evaluate Eq. 2.14, we need a method to determine a number of terms and the process for evaluating them are outlined below. As mentioned previously, we will be using liposomes as model particles in order to validate this approach for application under experimental conditions. This needs to be taken into account in the following section since the definition of several terms are dependent on various particle parameters.

2.4.1 Polarisability, α

Mikati *et al*. avoided calculating α by only determining the ratio of τ_{LD} and τ_A [37]. When α is required in RGD calculations the simple uniform $((m-1)/(2\pi))dV$ is often used for isotropic particles with a refractive index close to 1. Liposomes usually do have a similar refractive index to that of the surrounding medium, however, in any work involving hollow particles (as in liposomes), where the refractive index of the particle center is not identical to that of its outer shell, the polarisability is not constant and α needs to reflect this. Application of theory from Yoshikawa *et al* regarding scattering from spherical shells can be applied here to refine α [39]:

$$\alpha^2 = Vf\frac{m_1^2-1}{m_1^2+2} + (1-Vf)Vf\frac{m_2^2-1}{m_2^2+2}$$

(2.15)

where Vf is the volume fraction of the lipid in the particle, m_1 and m_2 are the complex relative refractive indices of respectively the shell and medium inside of the particle.

2.4.2 R, form function for solid ovoids and rod-like particles

The form vectors $R(\beta,\varepsilon)$ depend on the particle shape, size, axis-ratio and orientation. We used the RGD expressions from Van de Hulst *et al* for two cases: solid ovoids, with long and short semi-axis lengths of a and b respectively, and rod-like particles of length l, and diameter d. K_o and K_r denote the phase shift of the particle (ovoid and rod

respectively) in relation to the particle position and polar/azimuthal angles (β, ε) [32]. For solid ovoids:

$$R(\beta,\varepsilon)=\left(\frac{3\sin K_o}{K_o}-\frac{3\cos K_o}{K_o^{\,2}}\right) \tag{2.16}$$

where

$$K_O = 2k\sin\frac{\beta}{2}\left[b^2+\left(a^2-b^2\right)\cos^2\gamma\right]^{1/2} \tag{2.17}$$

and γ is the angle between z (the particle axis) and the vector that lies on the bisector of X and the scattering vector, **s** (the so-called bisectrix, expressed XYZ coordinate system).

$$\boldsymbol{B}=\left(-\sin\frac{\beta}{2},-\cos\varepsilon\cos\frac{\beta}{2},\sin\varepsilon\cos\frac{\beta}{2}\right)_{XYZ} \tag{2.18}$$

so

$$\cos\gamma = -\cos\theta\sin\frac{\beta}{2}+\sin\theta\cos\frac{\beta}{2}\cos(\phi-\varepsilon) \tag{2.19}$$

Alternatively, for rod-like particles:

$$R(\beta,\varepsilon)=F\left(kd\sin\frac{\beta}{2}\sin\gamma\right)E\left(kl\sin\frac{\beta}{2}\cos\gamma\right) \tag{2.20}$$

where

$$F\left(K_r\right) = 2\left(\frac{\sin K_r}{K_r^3} - \frac{\cos K_r}{K_r^2}\right)$$

(2.21)

and

$$E\left(K_r\right) = \frac{\sin K_r}{K_r}$$

(2.22)

Technically, as can be seen from Eq 2.17 and 2.20, a dependence on k is also incorporated into its form function R. However this is a relatively minor influence and not sufficient to cause such a dramatic departure from the k^4 relationship dictated by Rayleigh theory.

2.4.3 Form factor *R* adjustment required for hollow particles

To adjust the form factor R to account for hollow particles such as liposomes or e.g. tubulin, we must relate this to the original generalization for these R parameters from phase factors:

$$R\left(\beta,\varepsilon\right) = \frac{1}{V}\int_{-\infty}^{\infty} Be^{iK}\,dp$$

(2.23)

This integration represents slices of the particle perpendicular to the bisectrix, of area B and thickness p (equating to $2b$ for ovoids, and d/l for rod). Thus to account for hollow particles, the factor B is scaled by $(1\text{-}q)$ (q equating to the ratio of 'empty' interior to full particle radius). This difference factor can be taken out of the integral resulting in the following R adjustment:

$$R_{solid}\left(\beta,\varepsilon\right) = \left(1-q\right)R_{hollow}\left(\beta,\varepsilon\right)$$

(2.24)

2.4.4 Peterlin-Stuart probability density function

The Peterlin-Stuart probability distribution function $f(\varphi,\theta)$ is generally deemed to be a

reasonable approximation to reality for the degree of sample alignment in LD experiments. This function permits the calculation of the orientation parameter (commonly defined in LD related literature as *S*), for a given molecular axis ratio, pathlength and shear flow parameters. In related works by Strand and McLachlan *et al* (in similar coordinate systems) calculation of this function has already been accomplished[38,40]. The strict definition of this function, $\psi(s)ds$, is the probability that a particle will be found in the solid angle ds around the orientation axis **s**. The following expression is the normalization condition for ψ, as a function of *t* is therefore:

$$\int_0^{2\pi}\int_0^{\pi}\psi(\theta,\phi,t)\sin(\theta)d\theta d\phi = 4\pi \tag{2.25}$$

so that $\psi/4\pi$ corresponds to a probability density. We choose *t* to be infinite, as it simply needs to be long to reflect plateau at maximum value of the experiment. Although not stated, presumably this is why *t* is excluded from ψ in both Mikati and Meeten *et al*[36,37].

2.4.5 Incident light intensity distance relationship

Lastly, previous works have failed to explain exactly how the relationship of incident light intensity (I_0) to the distance the scattered wave is from the scattering center (*r*), is calculated and for an accurate calculation of the actual scattering underlying a given spectrum, rather than a ratio, determination of this relationship is crucial[41]. The problem, and what is likely to be responsible for this lack of detail in previous works, is the difficulty in ascertaining a value for this parameter in a given machine setup. Determination of I_0 for a particular emitter although complex is still possible, however, practical concerns; such as the degree to which the incident beam strikes the particulate suspension (any loss of beam focus will reduce incident light intensity by an indeterminate amount) and how the incident beam must be treated as if it strikes the suspension non-uniformly, render it difficult to obtain a highly accurate value. The more pertinent point however is that if we consider the classical LD experimental setup of light source-sample-detector it is practically impossible to calculate a value for *r*. The experimental setup simply measures the difference in polarised light that strikes

the detector from the emitted, scattered light being detected as any that misses the detector. Therefore, the distance that the scattering vector travels to miss the detector is of no relevance. In this work we parameterize I_0/r^2 via the fitting of a scattering curve to an experimentally derived LD spectrum with known liposome deformation and orientation.

2.4.6 Wavelength dependence, bridging RGD-Mie theory

According to Rayleigh and RGD theory, as shown above, the relationship that a particle has with the wavelength of the incident light has a k^4, or λ^{-4}, dependence. However in both this practice and in previous works it has been shown by simply linear regression that this power relationship does not fit the experimental trends displayed. Instead the relationship that is demonstrated is far closer to that of classical Mie theory, a k^2 dependence. Particles that are approaching the limits of the size restriction outlined by RGD theory, and barely under the minimum for Mie theory would not unreasonable to see elements of both in effect. In other works by Yoshikawa et al regarding liposomes (of sizes 170-300 nm) these two theories have been contrasted, in Eq. 20-22 of their work[39]. The main differences in the approximations for each approach are the particle shape factors, since Mie is primarily restricted to spherical particles whereas RGD allows for asymmetrical particles, and a constant term. Since our approach already allows us to take into account any unknown constants (stray light, inhomogeneity etc.) into the determination of our unknown I_0/r^2 term, this can be incorporated into the same term. Therefore by allowing the exponent of k to vary by power 2, and taking into account this constant term whilst using the RGD particle shape definition, what we instead implement is a quasi RGD-Mie theory instead of strictly classical RGD.

2.4.7 Computational integration

In order to perform the required integrations, we initially attempted proceeded symbolically but run-times proved impractically long for the repeat-use necessary to fit a scattering curve to an experimental dataset for variable deformation parameters. Instead the calculation was approximated numerically using the rectangular rule as shown below:

$$\tau_{LD} \sim \sum_{kk=1}^{N} \sum_{ll=1}^{N} \sum_{mm=1}^{N} \sum_{nn=1}^{N} f(A,B)\, \Delta I(A,B,A1,B1)\ \cdot G \cdot H \cdot G1 \cdot H1 \tag{2.26}$$

where: $A = (kk - ½)G$, $B = (ll - ½)H$, $A1 = (mm - ½)G1$, $B1 = (nn - ½)H1$, $G = 2\pi/N$, $H = \pi/N$, $G1 = 2\pi/N$, $H1 = (\pi - \mu)/N$. Here f denotes the orientation distribution function, ΔI denotes the integrand of Eq. 2.14 and we define μ as the solid angle between the scattering center in the sample and the outer limits of the detector. It was determined that N=5 was sufficient; any further increases simply increased processing time with no noticeable alteration in scattering curve.

2.5 Conclusions

In this chapter we have covered the core theoretical approach behind Rayleigh-Gans-Debye theory regarding the calculation of scattered light for particles of various geometries (rod, ovoid and hollow particles). This has then been investigated regarding its application towards LD, taking into consideration the particle position and orientation with regards to the polarisation of the incident light. In preparation for application towards biological samples such as cells, modelled as liposomes in the following chapter, the field of Mie theory was considered in terms of the k exponent. Variability in this parameter has been observed in related literature, and a hybrid RGD-Mie approach was incorporated when considering the particles that exist within both the RGD and Mie size regimes. Our theory was then coded into a custom program and corresponding GUI for the scattering correction of a given dataset, provided particle parameters. To optimise this approach and determine its suitabiliy towards biological samples a model system was then required, that of liposomes under flow.

Chapter 3: Light scattering from lipid vesicles under flow

3.1 Overview

Liposomes have been commonly used for over a decade as simple models for cell membranes[42]. Despite this, their behavior in a variety of experimental conditions, such as under flow-induced shear stress, is not well understood. To complicate matters further, biological membrane bilayers contain a wide variety of different lipids, and other components, all of which can influence the behavior of the membrane in a given experiment[43]. It is generally assumed that liposomes distort into some kind of rod or ovoid shape in flow and in recent unpublished work (conducted within our research group) by Norton *et al*[53], they modeled these liposomes as a cylinder with hemispherical caps. The onset of flow therefore requires changes in either liposome surface area or internal volume or both. From the perspective of flow-aligned spectroscopic techniques in this work our focus is on linear dichroism (LD) and the more we understand about the response of liposomes within shear flow, the more information we can get about how lipid-binding small molecules (such as peptides and proteins) are positioned with regards to a membrane. However, when samples scatter light the desired absorbance LD is conflated with a scattering/turbidity contribution (since a LD signal is generated by measuring the flux of unabsorbed photons that reach the detector). Norden *et al* have previously examined the detrimental influence of light scattering on the detection and analysis of absorption spectra, including linear dichroism, within in the UV-visible region in the literature in depth[45]. They discuss the difficulties of quantitatively modeling light scattering, in essence this is because classical scattering theory assumes that particles are isotropically oriented and solid, and the anisotropic and hollow nature of liposome particles makes them difficult to model with this theory. In Norden's work they chose to match the refractive indices of the lipid vesicle contents and the surrounding medium (via the addition of sucrose), thus lowering the relative refractive index, which is proportional to scattering intensity.

This allowed them to measure an accurate LD spectrum of membrane-oriented tryptophan down to ~220 nm (much of which was previously obscured by scattering). Unfortunately the approach taken by Norden *et al* does not solve the scattering interference problem at lower wavelengths where sucrose absorbs. However, recent (unpublished) works by Norton *et al* conducted within the same research faculty offer an alternative perspective on the situation with the use of calcein to assess the volume change for liposomes of different lipid composition when subject to Couette flow induced shear stress (and collected the corresponding LD spectrum from those lipid compositions)[53].

Calcein is a self-quenching fluorescent dye, and when it is concentrated inside liposomes, its fluorescence is almost completely quenched, but if it leaks out of the liposome, thus becoming diluted, its fluorescence switches on[46]. Under LD flow conditions, these liposomes are stretched due to the shear stresses present (and in relation to the intensity of the shear rates) altering its internal volume. In this work we combined this volume-loss assay with results from our scattering modeling approach taken in the previous chapter, in order to correct the corresponding LD spectra. The Rayleigh-Gans-Debye (RGD) approximation has been used in the past to model light scattering in a number of contexts. We have applied this theory to LD data, establishing the equations for both LD and absorbance, rather than simply determining the ratio of the polarized and unpolarized signals. In doing this we have accounted for the hollow nature of liposomes, and corrected small errors that arose in the Mikati application of the RGD approximation which did not matter for the ratio implementation[37]. In addition, we achieve an indirect visualization of the shapes that liposomes adopt in flow, as well as an estimate of the LD orientation parameter, S. S is a parameter describing the degree of orientation: S=1 for perfect orientation and S=0 for no orientation.

3.1.1 Scattering correction code implementation.

As mentioned in the previous chapter, it was postulated that when particles reach a particular boundary between the size/refractive index restrictions of RGD and Mie they might present a change in the dictated wavelength dependence relationship. Extensive

testing has shown that for vesicles of ~100 nm in diameter, this wavelength relationship of k^4 as dictated by RGD theory is indeed insufficient[26]. This is supported in previous works where curves fit through linear regression on shear flow aligned tubulin microtubules were also unable to be fit with this fourth power relationship.

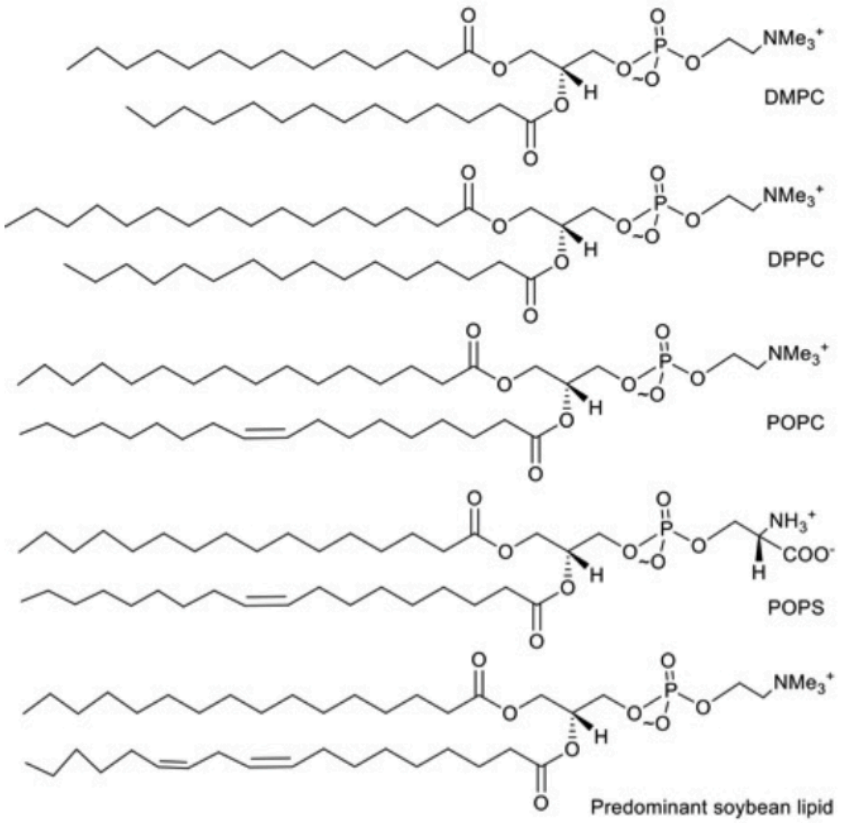

Figure 3.1: Lipids used in the calcein leakage study, with the exception of BTLE, which is a composite variety of lipids.

Taking into considering that our experimental approach already allows us to take into account any unknown constants (stray light, inhomogeneity etc.) into the determination of our I_0/r^2 term, this can be incorporated into the same term. So instead of a k^4, wavelength dependence, instead fits were conducted with a k^2 dependence with much greater success.

We found that calculation of I_0/r^2, where r is the distance of the scattered wave from the scattering center and I_0 is the incident light intensity, was not sufficiently accurate for our purposes, as we could not allow for the divergence of the light beam

or the reflections from parts of the optical system. Any sample inhomogeneity caused further error. We therefore used an alternative approach in which we used a well-behaved sample to parameterize I_0/r^2 as described in Results. By fitting a calculated scattering curve with variable I_0/r^2 to an LD spectrum with a known particle deformation/axis ratio (provided by the calcein leakage assays), I_0/r^2 for our instrument and experimental configuration was obtained. This would need to be repeated for different instruments and configurations. The calculations for τ_{LD} were coded in MATLAB for ovoid geometries with input parameters given in Table 3.1.

Table 3.1: Vesicle scattering correction program input parameters used to model the experimental setup.

Input Parameter	**Value**
Lipids per vesicle	8.17×10^4
Lipid membrane thickness/nm	4
Capillary volume/μl	83.25×10^{-6}
Capillary outer diameter/mm	2.9
Capillary inner diameter/mm	2.4
Shear rate/s^{-1}	1.8×10^3
Medium refractive index	1.33
Vesicle refractive index	1.42
Instrument Parameters	**Value**
Incident light wavelength range/nm	230–750
Distance from detector/cm	3
Detector radius/cm	1.5

The integrals of Eq. 2.14 can be performed either symbolically or numerically, but symbolic integration is time consuming and impractical for the repeat runs required for fitting turbidity LD curves to spectral data. We therefore used the rectangular rule (for M rectangles) to numerically integrate them, and successfully reduced the runtime for the program without any noticeable difference in the accuracy of the fit, as was previously done by Mikati *et al*[37]. Standard run-times were between 10 and 15 minutes for M = 5 in each variable (values for M under 5 did not improve the calculation) on a MacBook Pro. Operation of the code was relatively simple, requiring parameters: liposome long axis / nm, lipid concentration / mM, and refractive indices of the particle and the medium (in addition to any changes to the instrumental setup parameters in

Table 3.1). The outputs are τ_{LD} and the associated liposome parameters (*S*, percent leakage, axis ratio, semi-axis lengths). Successive runs are usually required for a good fit with run-times at roughly 4 min. In addition the design of a simple GUI that incorporation the final interactions of scattering calculation and correction was conducted in order to permit ease of use, Fig. 3.2. The code used in the implementation of this GUI for the scattering calculation of various particles is shown in Appendix A4.

3.1.2 Application

In order to calibrate the scattering fit for a particular machine setup, firstly a liposome LD spectrum of a known geometry under flow (established via calcein leakage studies conducted by Norton *et al*[53], Fig 3.5) must be selected for the purposes of determining I_0/r^2. POPC was used in this work. Since the exact determination of the total intensity of light being emitted by the machine and consequently being collected by the detector is difficult to measure (i.e. the value for I_0/r^2) an alternative method was devised. As demonstrated previously (section 2.1) since samples only absorb at their specific wavelengths there is a region at a higher wavelength range where no absorbance occurs (e.g. Fig 2.2, 300+ nm) and any remaining trend can be attributed to scattered light. Therefore the correct value of I_0/r^2 can be obtained by gradually altering its value until this long wavelength region in the liposome LD spectra (~400-500 nm) was changed from sloping to form a flat line parallel to the x-axis for the calibration sample. The value was then finely adjusted in an attempt to flatten regions of the lower wavelength spectrum that do not have any absorbance peaks present. This only needs to be done once per instrumental set-up. Once a suitable I_0/r^2 value is set, other samples can be fit in the same manner, using the long axis of the liposome as the variable. When the fits are completed the liposome parameters including *S* axis ratio and percent volume loss (as portrayed in Table 3.2) can be determined.

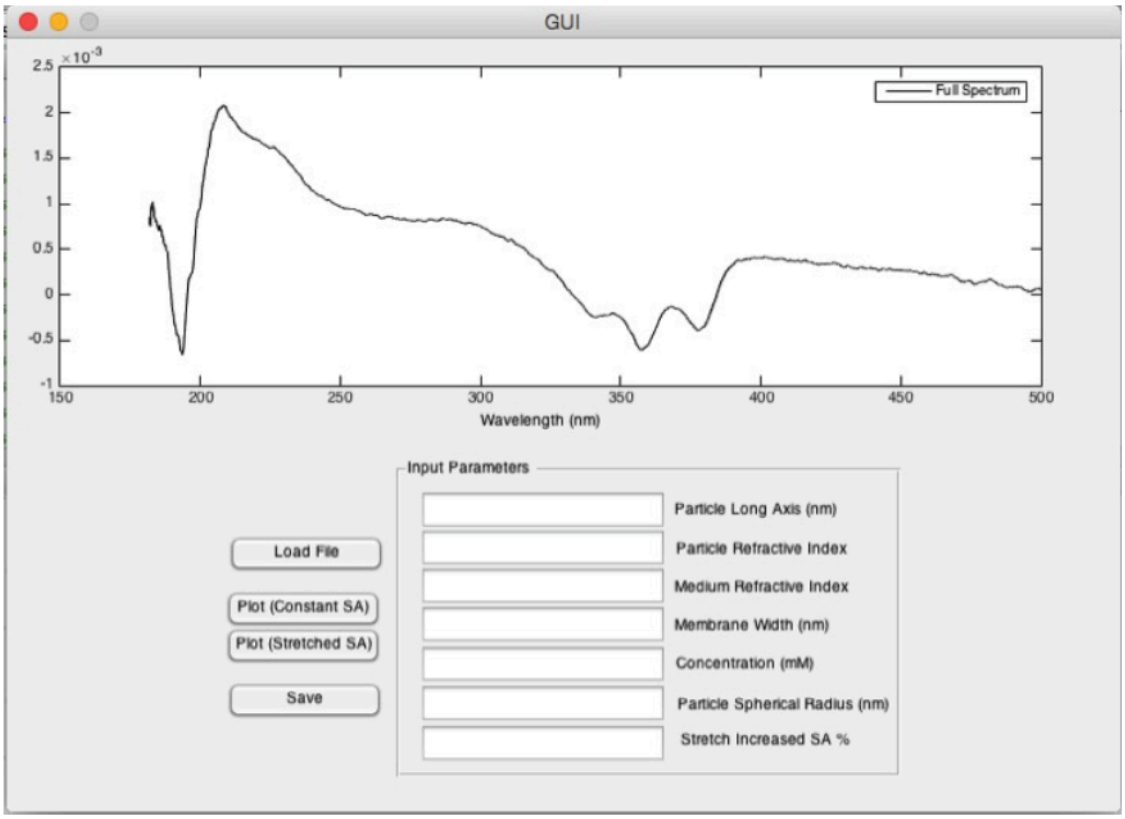

Figure 3.2: Demonstration of the created GUI for the purpose of scattering correction for deformable spheroidal particles with alternate mode to permit membrane stretching, and various particle specific input parameters.

3.2 Results

Calcein has previously been reported to emit its strongest fluorescence around 520 nm, with this figure being universally accepted. However, as shown Figure 3.3, the peak wavelength of the emitted fluorescence varies in a concentration-dependent manner. At high concentrations the fluorescence intensity is small with maxima at ~564 and 525 nm, whereas at low concentrations the maximum shifts to ~536 nm. The presence of 2 peaks in the higher concentration solutions (>20 mM) is probably due to two environments for the fluorophores probably corresponding to two different stacked geometries (J and H aggregates)[47]. The wavelength of maximum fluorescence plotted as a function of concentration (Fig. 3.3, bottom) gives a means of identifying calcein concentration in the solution. Between 10-45 mM there is an approximately linear relationship between $1/\lambda$ and the concentration.

$$\lambda_{max} = -7x10^{-7}[calcein]^{-1} + 0.0018 \quad (3.1)$$

At concentrations, above 50 mM, the fluorescence is very weak and the solutions are very dark. In the context of liposome leakage, the wavelength dependence of calcein fluorescence has the advantage over the usually used intensity measurements of directly enabling a quick estimate of liposome integrity.

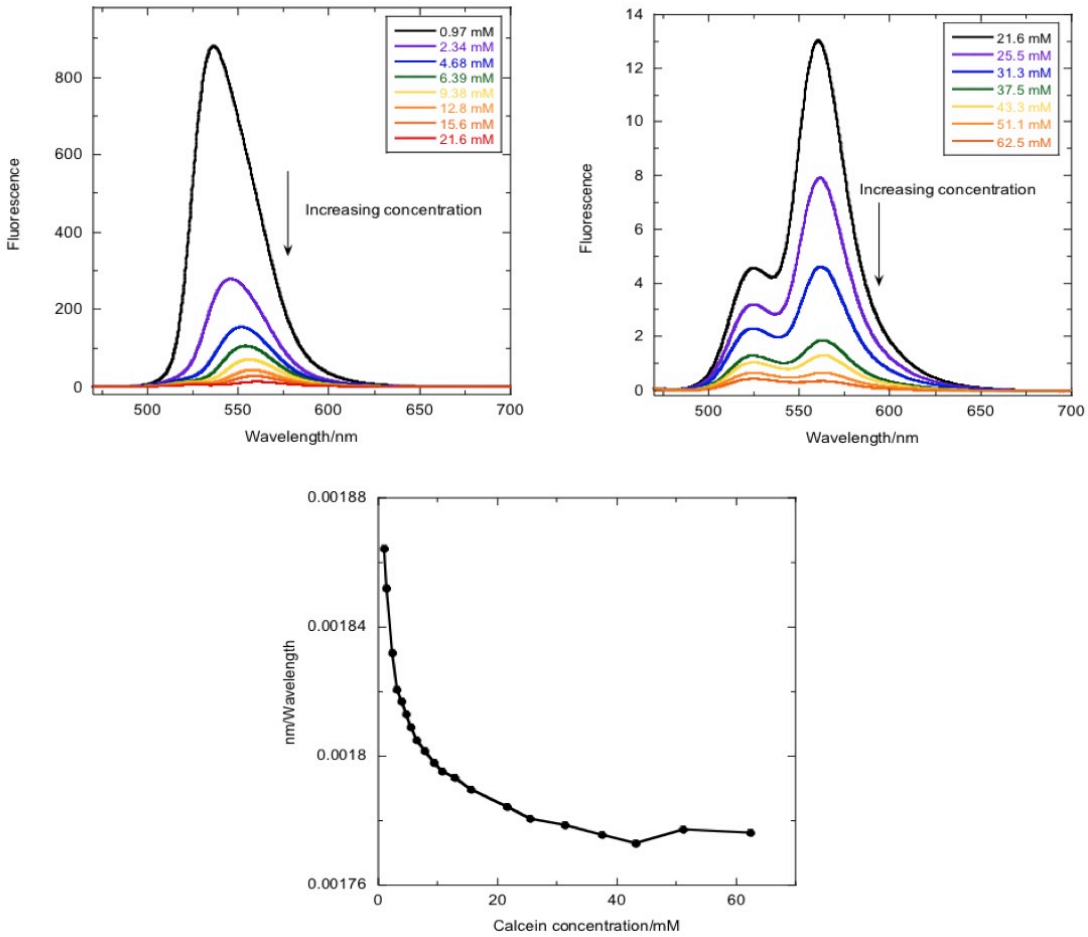

Figure 3.3: (a) Emission spectra for calcein excited at 460 nm as a function of concentration. (b) Concentration of calcein against maximum of emitted fluorescence.

3.2.1 Leakage from liposomes at steady state and flow

Prior to these leakage studies a series of stop/start shear flow time-course experiments was performed by previous members of the research group (unpublished, Lloyd *et al*[52]) measuring either pure fluorescence or combined fluorescence and light scattering (by means of a filter to remove scattered light), produced from calcein filled liposomes in order to probe the mechanism of leakage. When calcein was only present at high concentration inside the liposomes, its fluorescence is approximately zero, however, when it leaks out the overall calcein concentration is lowered and has increased fluorescence (Eq. 3.1). Regarding the changes pure fluorescence (Fig. 3.4, left), there is a clear fast (<1 s) switch between intensity gradients when the shear flow is changed. However, when we measure the combined scattering and fluorescence intensity (Fig. 3.4 right), with each flow stop there is a decrease in signal followed by an instant recovery as flow starts. Flow transformations such as tank treading, tumbling or trembling should cease with the flow, and therefore should not demonstrate this phenomenon. In addition, since scattering changes indicate changes in geometry, and those transformations do not change the existing shape of the liposome significantly, they should not cause significant changes in scattering intensity. We therefore can conclude that what we are observing is deformations of the liposomes under flow, as they elongate from a near-spherical shape under stationary conditions to ellipsoidal. The slow timescale presumably reflects the molecular rearrangements in the liposome membrane, most likely involving a recovery of liposome contents via slow diffusion of medium through the lipid membrane.

Another feature of the fluorescence-only data of Fig. 3.4 is that there are two intensity gradients depending on whether flow is on or off. This implies that there is a different leakage mechanism for each state. Initially our intention had been to ascertain the extent of deformation from the difference in leakage under flow on/off conditions. However, this is not possible if a separate leakage mechanism exists for the two conditions. Further, the change in fluorescence during the flow-off times is a constant gradient (of leakage) independent of the recovering state of the liposome in contrast to the scattering + fluorescence data. Based on these analyses, the extent of deformation via leakage should be determined exclusively from flow-on data.

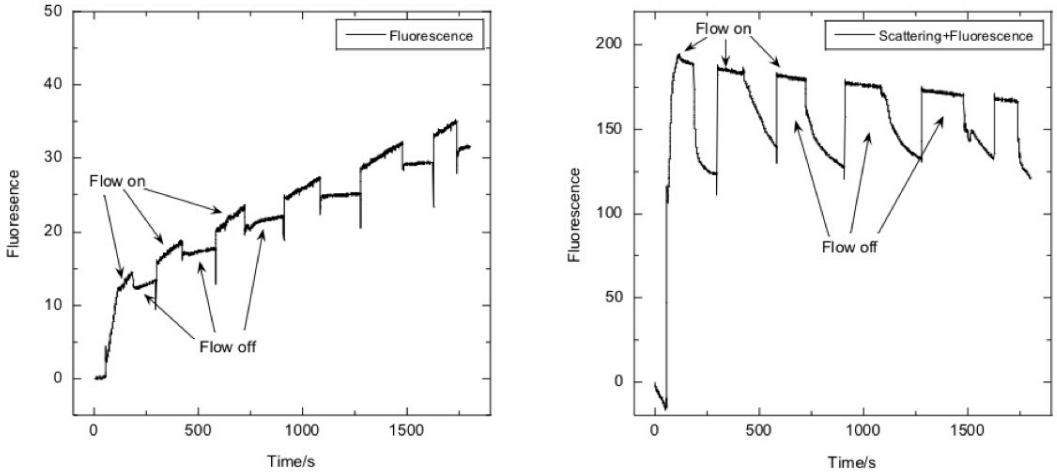

Figure 3.4: Couette shear flow on (3000 rpm)/off: (left) fluorescence and (right) fluorescence + scattering time-courses, for calcein (50 mM initial concentration inside liposomes) filled soybean PC liposomes (20 mg/mL) [52].

3.2.2 Quantification of leakage from liposomes

In the work by Norton *et al*[53], liposomes were prepared with the lipid contents, as summarized in Fig. 3.1. Liposomes were then loaded into a micro-volume Couette LD cell and fluorescence was measured for 30 minutes, with or without rotation at 3000 rpm (Fig. 3.5). The lysed reference was applied to scale leakage measurements over the time course to normalize the data for the amount of dye in the sample, as this cannot be controlled at the chromatography stage. It was particularly noticeable that for pure DMPC liposomes a lower amount of dye (and therefore of liposomes) was present in the final sample, which necessitated fitting of the data for Fig. 3.5. DMPC raw data is included in Appendix A.1.

It is apparent that most of the stationary liposome samples leak to some degree and all samples leak more under flow. One liposome preparation, pure POPC, retained most of its integrity whilst stationary and exhibited only a small volume loss of 3.6% under steady shear flow. Soybean PC and BLTE were also fairly stable for stationary and flowing samples, with 6% volume loss. DMPC by way of contrast leaked most of its contents within 500 s when stationary, and much more quickly in flow. As the most reliable sample we therefore used POPC liposome preparations as the experimental standard to determine experiment and instrument parameters for the scattering

calculations discussed below. However with regards to fitting vesicle spectra and ascertaining the volume loss explicitly caused by the distortion of the vesicles under flow what needs to be considered is not simply the POPC volume loss under flow of 3.6%, but rather the difference in flow and non-flow leakage of 1.4%.

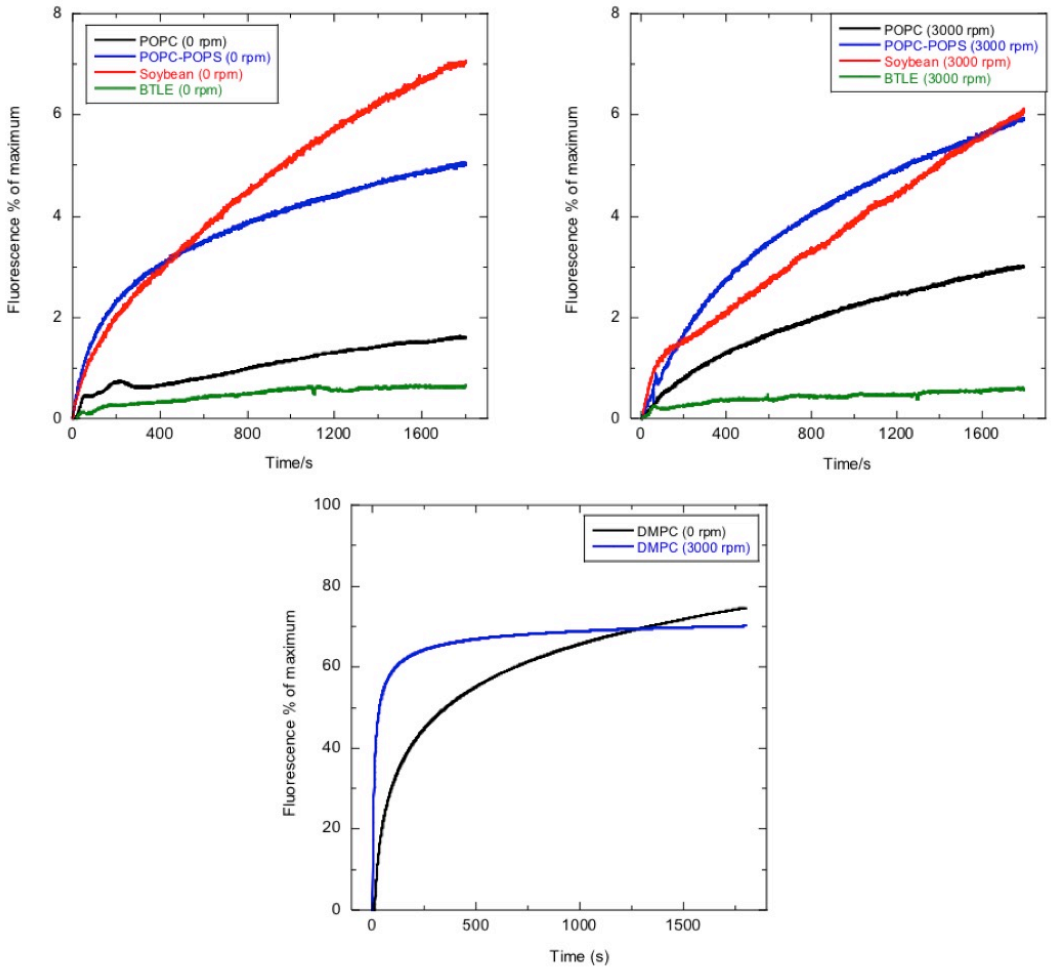

Figure 3.5: Fluorescence of calcein leaked from a variety of liposomes preparations (Figure 3.1) with and without the influence of shear flow as indicated in the figures. a) Stationary samples. b) Samples in Couette flow. c) Traces for pure DMPC liposomes fitted to a curve, since measured values had poor signal: noise. Initial calcein concentration inside liposomes 50 mM, lipid concentration 20 mg/ml, pathlength: 0.5 mm.[53]

3.2.3 Liposome volume change in Couette flow

Once we know how much volume is lost from a liposome, if we know the geometry of the flowing particle, we can translate that into geometric parameters. We assume that liposomes are spherical at rest and can be represented as an elongated ovoid when in shear flow (Fig. 3.6). Then, if we make the preliminary assumption that the surface area stays constant when the liposome is distorted in flow (i.e. the lipids are packed to the same density) but the volume changes, we get an upper bound for the volume lost for different degrees of distortion. Conversely, we get a lower bound if we assume no volume change but a surface area change. Liposomes, as shown previously (Fig 1.11) can be considered to be spherical when stationary and when deformed or stretched under shear flow can be treated as rigid ovoids/prolate spheroids. If we then model the liposomes as such, we can estimate S (particle orientation parameter) for different degrees of distortion (using the theory demonstrated in Chapter 2). Table. 3.3 summarises the relationship between volume loss and S for constant surface area (SA). A small distortion from spherical corresponds to a small loss of volume and low orientation and conversely for a large distortion. In previous work regarding soybean PC orienting in flow with bacteriorhodopsin, our experimental estimate of the orientation parameter S for the liposomes was ~0.03 (3% of liposomes have their long axis aligned with the direction of flow)[26,54]. We use this value here as the DPH solution absorbance includes both membrane bound and significant free analyte. When S~0.03, this corresponds to an 11% loss of volume ($V \sim 4.67 \times 10^3$ nm^3) in order to maintain constant SA. Comparison with the data in Figure 3.5 therefore shows that the POPC, soybean PC and BTLE liposomes must expand their surface area in shear flow as their volume loss is smaller than this value. In order to account for this discrepancy in volume loss between Table 3.2 and the experiment values, we have to correct our preliminary assumption to allow for a combination of SA and volume change. Therefore the shape of the flow-induced ellipsoid is deduced to be intermediate between the lower limit of distortion where the surface area of the liposome is held constant and the upper limit where the volume is held constant. DMPC loses far more

than 11%, though this is at least in part due to leaky membranes as DMPC liposomes leak significantly even when stationary.

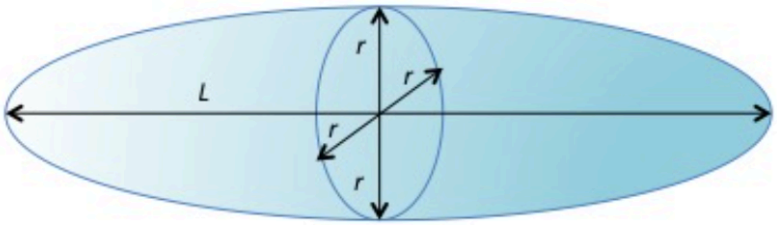

Figure 3.6: Ovoid model of liposomes used herein: length *L*, radii of both other axes are identical and denoted *r*.

Table 3.2: Example values of orientation parameter *S*, and volume *V*, calculated according to for ovoids of length *L*, and radius *r*, with the same surface area as a sphere of radius 50 nm and volume 524,000 nm^3. This makes an upper bound for volume change induced by shear flow

***r* / nm**	***L* / nm**	***V* / nm^3**	**% *V* Loss**	***S***	**Axis Ratio**
49.0	104	$5.23x10^5$	0.001	0.018	1.06
45.0	121	$5.12x10^5$	0.02	0.020	1.34
42.0	134	$4.96x10^5$	0.05	0.024	1.60
38.0	154	$4.67x10^5$	0.11	0.030	2.03
35.0	171	$4.39x10^5$	0.16	0.038	2.44
32.0	191	$4.09x10^5$	0.22	0.05	2.98
26.0	240	$3.40x10^5$	0.35	0.09	4.62
20.0	316	$2.65x10^5$	49	0.17	7.90
15.0	423	$2.00x10^5$	69	0.29	14.1
10.0	636	$1.33x10^5$	0.75	0.44	31.8
5.0	1270	$6.67x10^5$	0.87	0.69	127

3.2.4 Liposome LD spectra

LD spectra collected for liposomes comprised of the lipids, as shown in Fig. 3.1, were prepared with diphenylhexatriene (DPH) included in the membranes as a spectral reporter (Fig. 3.7)[53]. DPH absorbance occurs between 300 and 400 nm with little signal between 200 and 300 nm. It is a known fluorophore that can intercalate with lipid membranes, primarily parallel to the lipid fatty acid chains. DPH is a long thin molecule whose film LD spectrum in polyethylene (Fig. 3.7, S~0.5) demonstrates that the 360 nm region is polarized along the long axis of the molecule. Since the lipids do

not absorb at 360 nm, DPH acts as a marker to detect the orientation of lipids via LD, with the negative signal seen at 360 nm indicating DPH is indeed inserted parallel to the membrane normal. The magnitude of the DPH LD relative to the absorbance indicates the degree of orientation of the liposome. Unfortunately there are no data available regarding levels of DPH take-up by liposomes, particularly those of different composition and concentrations, so if we assume all the DPH is inserted parallel to the lipids we will therefore only get a lower bound for the liposome S. Several examples of liposome spectra are shown in Fig. 3.8-10, additional DMPC and replicate BTLE spectra are shown in Appendix A.1. While the LD signals of the DPH are fairly apparent in each case, it is clear that what we are measuring is a combination of A_{LD} and τ_{LD}. It was therefore an ideal system to test any scattering protocol.

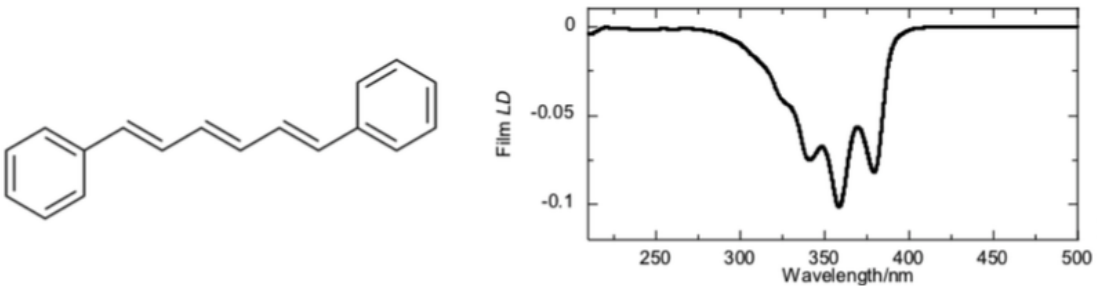

Figure 3.7: Molecular structure of the fluorescent chromophore DPH and its stretched film LD spectrum dropped from a concentrated solution in $CHCl_3$ onto pre-stretched polyethylene film.

3.2.5 Scattering Correction

Previous works within the same research group attempted to correct for scattering in LD spectra using the equation as demonstrated in Eq 1.1. Although it had been previously used with apparent success, we have been concerned about the wide variation of values for g that are required even for similar spectra, in addition to potential for heavily over-correcting at low wavelengths (<230-240 nm)[26].

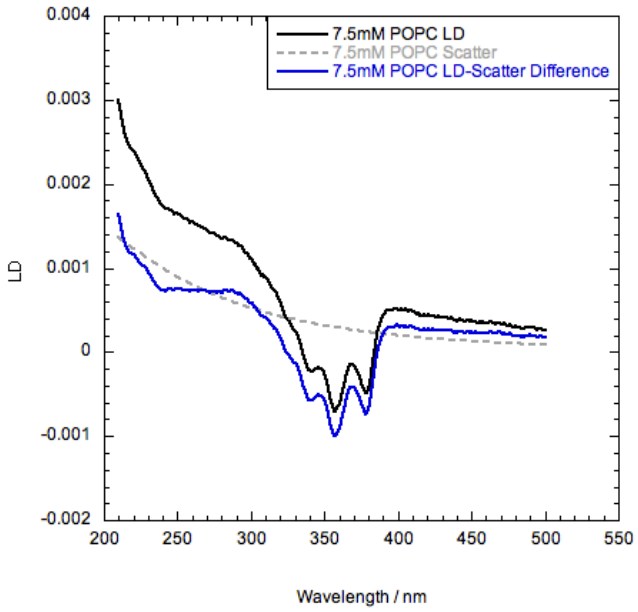

Figure 3.8: Representative LD spectra from POPC liposome preparations, (7.5 mM), with fitted scattering curve for a set volume loss of 1.4%. Samples were prepared containing DPH (1%w/w) with associated fitted scattering curves and corrected spectra for constant surface area. Pathlength: 0.5 mm.

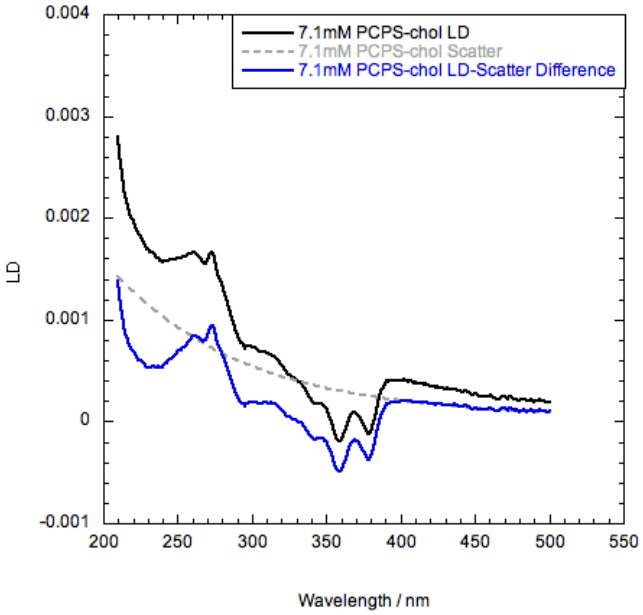

Figure 3.9: Representative LD spectra from POPC/POPS/cholesterol liposome preparations, (total concentration 7.1 mM, mixed at a 75:10:15 ratio). Samples were prepared containing DPH (1%w/w) with associated fitted scattering curves and corrected spectra for constant surface area. Pathlength: 0.5 mm.

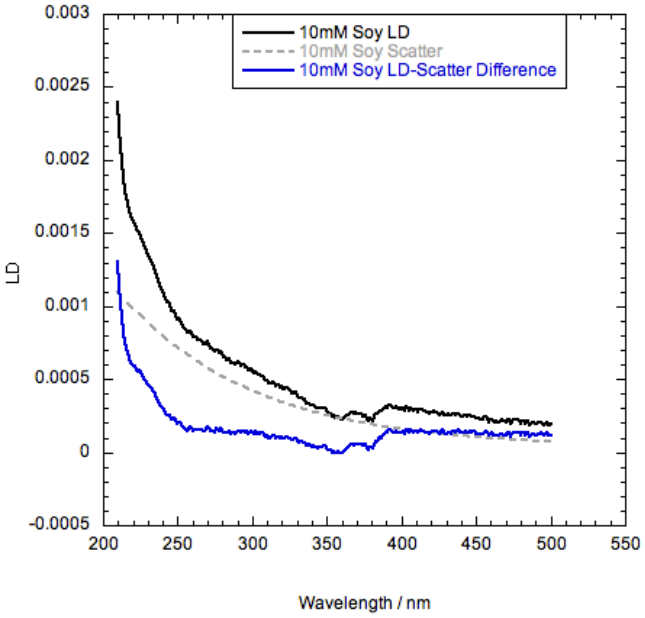

Figure 3.10: Representative LD spectra from Soy-PC liposome preparations, (10 mM). Samples were prepared containing DPH (1%w/w) with associated fitted scattering curves and corrected spectra for constant surface area. Pathlength: 0.5 mm.

Table 3.3: Examples of calculated liposome deformation parameters for several liposome varieties, with concentrations changed by serial dilution. Samples denoted [1,2] indicate repeated identical preparations. Top: Constant surface area; Bottom: surface area expanded such that soybean PC had a value of 0.03 for S. POPC (10 mM) samples were used as the standard to calculate the instrument parameter, I_0/r^2, as outlined in the text. Actual % volume loss determined by the difference in maximum % volume loss in Fig 3.5 for each lipid between flow states.

Lipid	**Conc. /mmol**	**Diameter /nm**	**Length /nm**	**Axis Ratio**	***% V loss***	**Exp. % V loss [53]**	***S***	***Average NRMSE %***
POPC	7.5	91.99 (+/-0.10)	116.5 (+/-0.22)	1.266 (+/-0.01)	1.401 (+/-0.07)	1.406	0.0195 (+/-0.09)	2.60
POPC/POPS /chol	7.1	91.29 (+/-0.08)	118 (+/-0.18)	1.293 (+/-0.01)	1.655 (+/-0.06)	0.8839	0.0198 (+/-0.001)	2.35
Soy PC	10	95.08 (+/-0.05)	110 (+/-0.11)	1.157 (+/-0.00)	0.549 (+/-0.02)	-0.1552	0.0184 (+/-0.0001)	6.55
BTLE [1]	10	73.29 (+/-0.00)	160 (+/-0.00)	2.163 (+/-0.00)	12.45 (+/-0.00)	-0.071	0.0327 (+/-0.001)	1.33
BTLE [2]	10	96.05 (+/-0.26)	108 (+/-0.54)	1.124 (+/-0.02)	0.357 (+/-0.10)	-0.071	0.0182 (+/-0.00)	6.76

Lipid	**Conc. /mmol**	**Diameter /mm**	**Length /mm**	**Axis Ratio**	***%V loss***	**Experimental *% V loss*[53]**	***S***
POPC	7.5	78.45	160.2	2.042	1.403	1.406	0.0365
POPC/POPS /chol	7.0	75.63	168	2.221	3.904	0.8839	0.0403
Soy PC	10	84.80	144	1.698	-3.542	-0.1552	0.0300
BTLE [1]	10	-	-	-	-	-	-
BTLE [2]	10	87.31	138	1.581	-5.210	-0.071	0.0280

We therefore implemented the RGD-derived approach outlined above and detailed in the ESI with POPC data to provide liposome deformation and instrument parameters (Table. 3.3). In order to obtain a measure of the accuracy of this approach for the different liposome variants, a method to measure the RMSE (root mean squared error) was devised. As mentioned previously in wavelength regions that contain no absorbance peaks, such as the 400-500 nm region in Fig 3.8-10, the deviation from a flat line (aka no contribution from absorbance or scattering) can be attributed to the influence of scattering. In that case the deviation from this flat line from the resultant scattering subtracted, or 'corrected', spectra should demonstrate the relative closeness of the fit to this 'perfect fit' (aka those regions demonstrate a perfectly flat line after the scattering has been removed). Once calculated for each liposome sample, and averaged over each non-absorbing region, the RMSE was then normalised with regards to the range of their LD data (Table 3.3, Top).

The fixed SA (surface area) fit (Table. 3.3 Top) represents the lower limit (regarding axis ratio and S value) in which the liposomes do not significantly stretch under flow, and have a surface area (SA) equivalent to that of a 100 nm sphere (validated via DLS measurements). We then allowed the SA of POPC to increase with the volume loss held equal to what was experimentally observed until S = 0.03 for that of Soy-PC, however for the most extreme case, BTLE [1], fitting proved impossible. These limits were used to calculate I_0/r^2 in Eq. 2.14 by fitting to the experimental data, allowing us to determine values of $5x10^{-12}$ for constant SA, and $1.05x10^{-12}$ for stretched POPC SA (7% SA increase). Since the lipid-specific variation in SA due to shear flow is unknown at this current time, all liposome samples were then treated as if they stretched to reach the same SA increase as the POPC standard with differing volume (Table 3.3, bottom).

3.2.6 Discussion

The approach taken above is that of a modified version of the standard Rayleigh/Mie scattering theory. However by virtue of the restrictions necessary for the theory to function it is limited in the nature of scattering particles it can accurately predict. Unfortunately for application regarding many biological systems, in several key areas

these limitations either prevent the calculation of scattering or greatly increase the complexity in using this approach, which will be outlined in brief. Firstly and least importantly there is the basic geometry of the particle, when dealing with highly flexible particles or that of rigid particles with shapes outside the basic forms (sphere, spheroid, discoid, rod). In general however this has the least impact, primarily because not only can more complicated form factors be determined but approximations can also be drawn from calculable shapes, so this rarely completely invalidates any calculation. More concerning however is the refractive index and polarizability of the particle. As mentioned in the Rayleigh size restrictions, once the particle's refractive index exceeds a set limit the phase shift is no longer small and it begins to matter where the incident wave interacts upon the particle, in essence no longer treating it as a single point. Although technically the hollow ovoid vesicles examined in the previous chapter are not purely isotropic in nature, however they are close enough such that they can be treated as such by the assumptions taken in the scattering calculation (i.e. that the lipid membrane and internal contents refractive indices are both separately homogenous, that the particle overall refractive index can be determined by an average depending upon the volume fraction of the hollow interior as done in related works). If for example a particle had a strong anisotropic polarizability (e.g. via a gradient dependence of refractive index relative to position within the particle instead of a uniform value) this would invalidate the Rayleigh approach.

In addition one of the simplest and the most significant factors regarding the Rayleigh and Mie approaches is that of size. As we have briefly mentioned both Rayleigh and Mie deal with particles of different sizes[39], however the restrictions are not precisely defined and the extent to which the accuracy of the fit falls off when the limits are approached or exceeded does not appear to have been fully explored. Unfortunately the restrictions of both theories are vague enough that this leaves a sizeable grey area regarding particle size and refractive index in which both are technically applicable and yet neither is entirely sufficient. Although for the purposes of consistency and fair testing, and since there is no method yet developed to determine the exponent of k in this 'grey' between the values of 4 and 2, the fittings previously conducted had to be conducted all for the same value (optimally found to be

2) even in this case there is noticeable room for improvement. If we consider the datasets for each lipid type, if the intensity is normalized and the DPH absorbance peak distribution disregarded the inherent scattering wavelength dependence can be observed. For the smaller particles like Soy-PC the shape of the scattering distribution can be seen to have more of a Rayleigh (k=4) character, as opposed to that of larger particles like BTLE which have more of a Mie character (k=2). Similarly upon taking a closer examination of the normalized RMSE in wavelength regions of non-absorbance, this can be seen to support this. The degree of error when fitting particles like Soy-PC can be seen to be noticeably greater at 6.55%, in contrast to those of POPC at 2.35%, indicative of the fitting conducted with k=2 resulting in a better fit for POPC versus Soy-PC. If we then consider the possibility of the liposome membrane stretching under flow, analysis of the results in the latter part of Table 3.3 also reveals that the stretching of vesicles is not a uniform affair. Taking into consideration the assumptions we have made to determine parameters for our RGD implementation for LD and any batch-to-batch variation, we can see that the scattering corrections of Fig. 3.8-10 for a range of different liposome/DPH LD spectra with different concentrations suggest that our pragmatic solution works for each liposome to a different degree. This is clear by the variable change in the estimated volume loss in contrast to those calculated for constant surface area liposomes (and regarding the experimental results obtained by Norton *et al*).

As previously mentioned, research conducted by Rodger *et al* has determined the value for Soy-PC liposomes to have an orientation value S of 0.03. If we then refer to Table 3.2, this should theoretically corresponds to a volume loss of ~11%. However in the experimental results determined by Norton *et al* for each lipid type this value appeared to be considerably lower than expected, each with <1% (with the exception of DMPC). Our model outlined in this chapter likewise estimates for liposomes that do not stretch, the volume loss from liposome deformation to be of similarly low values (with the expect of an outlier in one of the BTLE samples). Even if we were to take the raw % volume loss only from the vesicles under flow and disregard the contribution from the non-flow samples (aka the volume loss due to non-flow driven mechanisms) the highest % loss recorded (POPC and the POPC-POPS mix at ~6%) is still far below

this theorized value. However in the case that the vesicles are permitted to stretch, this makes more sense. By allowing the liposomes to stretch, the total volume of the liposome also increases allowing the liposome to deform to a greater extent whilst reducing the volume lost required for that deformation. In fact by taking in the surrounding solution as the liposome deforms, the result can actually be a net increase in volume which may explain the negative results observed in some of the experimental data and that of the calculated stretched liposomes. That each modelled liposome demonstrates a different change in volume loss to the same stretching impetus is also indicative of different stretching behaviours present dependant upon the type of lipid comprising the liposome in question.

Lastly rod-shaped fits were also attempted for the same liposome data sets as shown in Table 3.3, however, although similar fits could be obtained at higher vesicle concentrations, rod-fitting did not work well at low concentrations and was there- fore rejected in favor of purely ovoid scattering. In general for a given liposome preparation we found that the accuracy of the fit increased in direct proportion to the lipid concentration. However, we found batch-to-batch variations. This was particularly noticeable for BTLE (Table 3.3 BTLE [1] and [2]) and to a lesser extent soybean (data not shown), which demonstrate high consistency for repeat samples made with the same batch of liposomes, but variability between different preparations. The single lipid samples in general behaved consistently between batches (though the DMPC signals were very noisy). Lastly it should be noted that for most lipid samples <5 mM concentration the LD spectral intensity is not sufficient to distinguish the scattering contribution for fitting (as observed by scattering fittings collected on unpublished LD data collected by Norton *et al*). The positive aspect of this however is that a scattering correction is also less necessary at those lipid concentrations.

This problem becomes more extreme, and very noticeably in the field of LD, when these limits are greatly exceeded. When dealing with large particles relative to the incident wavelength the scattering calculation now needs to take into account separately the diffraction, reflection and refraction[32]. This is because when considering an incident beam of light it matters whether the light directly impacts the particle (reflection & refraction) or passes alongside it (diffraction). Considering reflection, due

to the large particle size what can also occur is a phenomenon known as total internal reflection (TIR)[48]. The light may emerge after a single reflection or after an indeterminate amount of reflections within the particle. Since the vectors of the scattered light needs to be determined in relation to the detector aperture, it becomes nigh impossible to state the overall scattering intensity angular distribution for an experimental setup. Although to a lesser extent for our purposes, since back-scattering is less relevant, another feature in diffuse reflection (reflection that can occur at many angles instead of a single one, as with specular reflection), comes into effect[49]. Lastly although diffraction has a significant impact on the scattering, theoretically it should have little to no effect for the purposes of LD. Diffraction theory as defined by van de Hulst is described as having the same state of polarization independent of the particle[32] (aka there is no difference in the intensity of diffracted light produced from parallel and perpendicularly incident light). In the theory this translates to the amplitude matrix (*S*) having values such that $S_1 = S_2$, which returns a null result when taking the difference in parallel and perpendicularly polarized incident light for LD determination and as such as such it is a non-factor for the purposes of LD scattering correction.

This can be easily demonstrated in recent works done by related parties within our research group in which the LD pattern for growing diphenyl-alanine particles were examined[55]. These particles start off nucleation at a very small level, but rapidly grow to tens of microns in diameter and millimeters in length (far beyond RGD theory)[50].

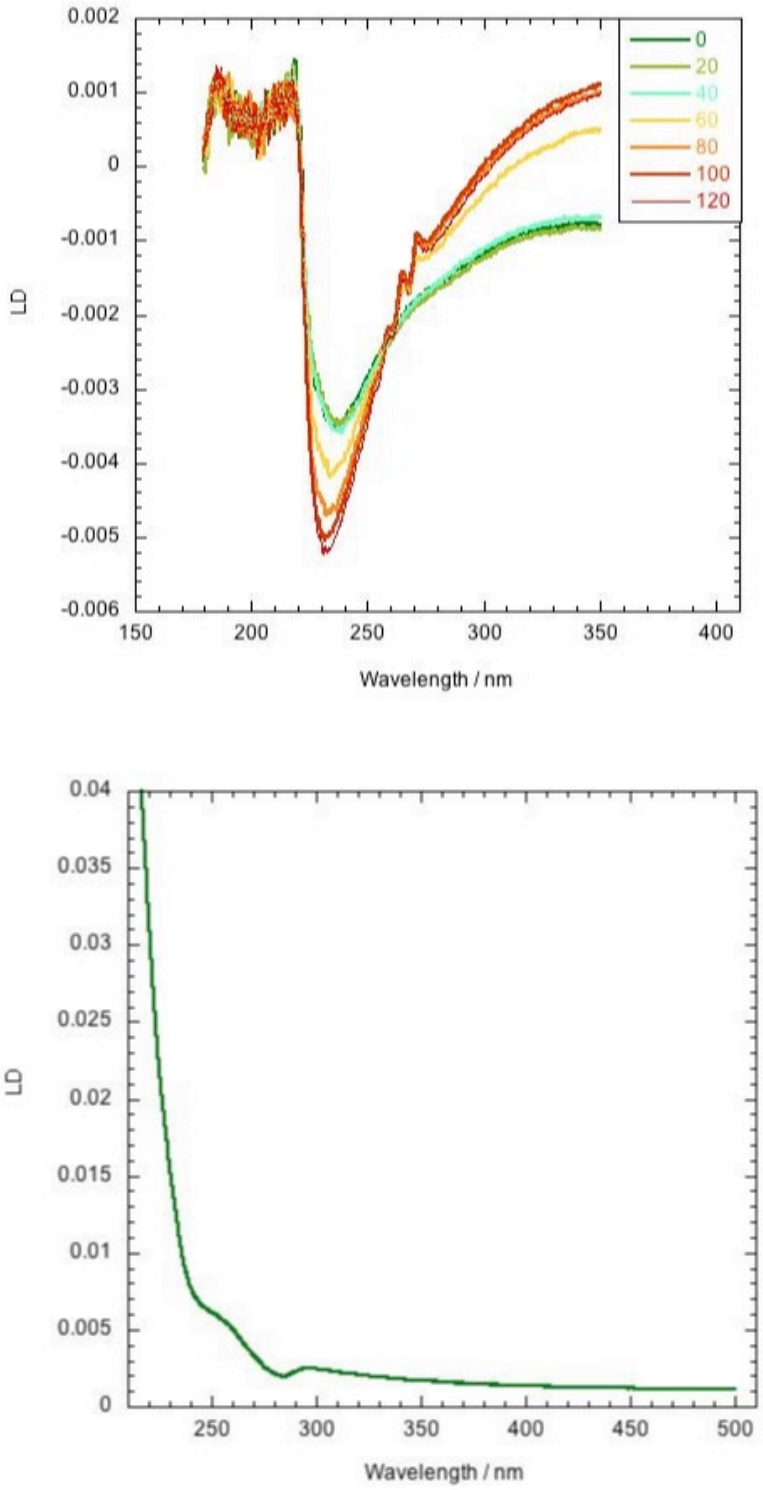

Figure 3.11: Representative LD plots for diphenylalanine (top) and FtsZ (bottom) flow orientated fiber particles. Legend for diphenylalanine denotes time (mins) since the initiation of fiber growth[55].

In contrast we can also examine LD spectra collected similarly on FtsZ fibers[55], which grow to only a few hundred nm in diameter (slightly outside RGD in the UV-Vis region). As we can see although both fiber samples are technically outside of the RGD limits, there is still the recognizable wavelength dependence indicative of RGD/Mie theory (dependence upon on the exponent of k to the $2^{nd}/4^{th}$ power) present within the FtsZ fiber (although more accurate fitting would prove quite difficult). In stark contrast there are the diphenyl-alanine fibers, which demonstrate a clear departure from this trend that becomes exacerbated with time as the fibers grow. This 'inverse wavelength dependence' behavior appears to depart from previously examined trends. It is severely unlikely that such uniaxial particles would align significant against flow orientation, and such that without a severe departure from established LD theory cannot be understood in terms of our current scattering theory. It does seem strange however that despite the interference caused by 'multiple scattering' from the many internal diffractions occurring within the particle that such a clear angular distribution such that is appears after the LD polarization difference is taken. One possible alternative is that the LD signal is derived from the much smaller nucleation particles[51], however that does not yet explain the clear inverse trend. It is apparent however that when considering the practical application of scattering theory when dealing with large uniaxial particles and polarised light that this field of research is underdeveloped, particularly when it comes to the application of more complex spectroscopic techniques such as LD.

3.3 Conclusions

In this work we have implemented a quasi RGD-Mie scattering theory approach developed to calculate the scattering contribution within liposomal LD (aka. turbidity linear dichroism) and removing its spectral influence. This then enables an accurate analysis of linear dichroism spectra even in the presence of significant scattering[32,36,37]. We have found that once the scattering model (including instrument and experiment parameters) has been established it can be applied to a range of liposome LD data. A by-product of the spectral correction is that we also determine the degree of

deformation and volume loss in the LD experiment, without the necessity of designing and performing a matching calcein fluorescence assay. In this work we selected a stable set of liposome deformation data to act as a standard from which to calculate instrument parameters and thus τ_{LD} for any lipid system collected in that instrument configuration. Here we calculate *S* directly following McLachlan *et al*[38]. Other applications may require an alternative determination of *S*. Our approach was examined using several sets of pure liposome LD spectra and in each case was capable of simultaneously eliminating background scattering and determining values for the degree of deformation, volume loss, and the orientation parameter *S*. Thus we have been able to calculate the true absorbance LD spectra of light scattering samples, rather than being limited to simply contrasting the resultant overall LD intensity across different samples for a much rougher qualitative analysis.

We also further developed a calcein fluorescence intensity assay (first put forward by Norton *et al*) to measure volume loss from liposomes when stationary and when deformed under shear flow. Calcein fluorescence not only enhances significantly with dilution as is well established but also shifts from 525/563 nm to 536 nm. $1/\lambda_{max}$ can be used to determine calcein concentration below 45 mM with fluorescence depending approximately linearly on concentration between 45 mM and 10 mM. Leakage depends upon the type of lipid and the duration of flow, with the shorter chain DMPC exhibiting the highest degree of leakage. Liposomes made from POPC, the mixed soybean PC, and BTLE (brain extract) lipids, all performed well in stationary and flowing conditions. Addition of cholesterol however reduces stability; therefore for flow LD experiments we recommend POPC or natural lipid mixtures without cholesterol. In addition, the results of this scattering modeling approach, in tandem with the experimental work conducted by Norton *et al*, seem to indicate the presence of liposome stretching occurring, and the extent this occurs is specific to each lipid type. To further develop this technique, an investigation into the stretching mechanisms for different liposome lipid compositions would be of great use. It should be noted that our approach is not purely limited to LD, although modification of the theory would be necessary to apply the work to calculate scattering from either pure absorbance or circular dichroism.

Considering the LD produced by biological samples such as cells, as liposomes are most apt to mimic the behavior of in flow, this scattering approach should prove to be of significant use. The scattering produced by both individual components, such as tubulin, and the cells themselves can be expected to all contribute towards the resultant LD spectrum. As can be seen in the following work, in order to fully comprehend a complex cellular LD it is not only necessary to collect and understand the absorbing contributions from each component within a given LD spectrum but it is also necessary to be capable of scattering correction for each case. Another possibility exists that for future work is that by fitting the scattering for each component, the individual orientation parameters for each component and even parameters for the entire cellular system could be ascertained (i.e. liposomal *S* and flow deformation parameters).

Chapter 4: Minimal component systems

In order to breakdown and fully comprehend a given LD spectrum, several issues need to be identified and analysed. If we were to take a specific biological system and analyse it via LD, the resultant spectrum would consist of a composite spectrum constructed from each of the absorbing components within that system. However each component will not necessarily have the same position, much like how membrane proteins can be oriented either parallel to the membranes surface, within that system, (nor will each system orient to the same extent). This causes various degrees of component alignment unique to a given system. If we may make the assumption that for a biological system with high aspect ratio (as is required to produce an LD signal) the long axis of that system is aligned with the flow direction, that system may still also freely rotate around any other symmetry axes in flow. Depending upon the geometry of that system the dynamics of these rotations will further influence the component alignment of that system. The overall component alignment can become even more complex when considering systems such as vesicles are examined where phenomena such as tank-treading or tumbling may occur, and consequently any absorbing components that are membrane anchored will present either null or greatly altered signals[56]. Tank-treading is where the membrane rotates around whilst the vesicle position remains constant, whereas tumbling is simply the rotation of the entire vesicle.

The intensity, and indeed the transition sign, of any given peak (or contribution to an overlay from multiple peak species) within a cellular LD spectrum can be assigned to a particular component and describes the overall average alignment of that component within the system. Although it is difficult to break down the component peak intensity into every influencing factor without pre-determined variables, simply the capacity to identify and assign peaks to system components serves to confirm features such as the presence of component anchorage within the system, (since any

'free-floating' components should return a null LD signal). Since the overall intensity of a given peak within an LD signal is also dependent on additional features (as will be explained below, with the influence of spectra artefacts such as scattered light and internal refractions, which introduce complications), full assignment and analysis of components is difficult to conduct without extensive preliminary work regarding the individual component absorbance spectra. To start with the focus of this work is ideally placed on the identification and assignment of peak species within a multiple-component / cellular environment and the identification of any further potential complications that may occur.

4.1 Experimental materials and protocols

All spectra were measured using equipment from the Jasco line, and temperature controlled (Jasco Analytical Instruments, Inc., UK, Essex). Absorption spectra were measured using a Jasco V-660 UV-VIS spectrophotometer. Circular and linear dichroism spectra were measured using the Jasco J-815 and J-720 spectrometers. Fluorescence spectra were measured using the FP-6500 fluorometer with excitation wavelengths at 240 and 265 nm. For erythrocyte examination, separation was conducted using a Force 7 Fisher micro-centrifuge, and cell count images were measured in quadruplicate via an Auto M10/EX-DEMO-UNIT cellometer (Peqlab, Germany). Biological reagents used to compile the data library were primarily supplied by Sigma Aldrich, UK (namely the nucleobases, amino acids, haemoglobin and purified calf thymus DNA). Similarly chemical reagents and solvents used (ethanol, phosphate buffered saline) were also supplied by Sigma.UK. M13 DNA was prepared by members of the Biophysical Chemistry group, and fission yeast from the Biology department, (University of Warwick, UK) and used as received. Lastly erythrocyte studies were conducted on 25ml preparations of defibrinated horse blood from TCS Biosciences, UK.

Table 4.1: Standard scanning machine parameters for the measurement of absorbance, LD and CD within the UV-Vis wavelength range.

Min Wavelength / nm	180
Max Wavelength / nm	750
Data Pitch	0.2
Bandwidth	≤ 2.0
Scan Speed / (nm/min)	≤ 200

For each member of the data library (amino acids, nucleotides, DNA and M13 phage), CD and most crucially ultra-violet - visible (UV-Vis) absorbance spectra were taken using purified 18.2 MΩ water as the solvent. All nucleobase samples were taken using 1 mm path-length cuvettes with concentrations as noted in Figure 4.3. All cuvettes used in these studies were constructed from quartz instead of alternative materials such as glass, which interferes with spectral recording. Aromatic amino acid spectroscopy was conducted, for a range of concentrations between 0.01 and 1 mg/ml for each of L-Tryptophan, L-Tyrosine and L-Phenylalanine. With regards to path-length, samples were taken using either a 1cm or 1mm cuvette as specified. Purified haemoglobin samples were treated in a similar manner using 12 μM solutions to establish the absorbance spectrum and 6 μM spectra for the majority of the CD spectrum (180-360nm, path-length 1mm), the latter recorded primarily to verify protein integrity. However, above 360 nm higher concentrations of 43.3 μM (Mr ~ 16500) were necessary to achieve a significant signal.

During Gaussian spectrum fitting all library absorbance and CD spectral data were converted using the Beer-Lambert Law to ε for UV-Vis absorbance, and Δε for CD, where ε is the wavelength-dependent molar absorptivity coefficient with units of $M^{-1}cm^{-1}$. This allows us to disregard concentration as a factor since all spectra taken from the same sample should be identical.

$$Absorbance = \varepsilon . pathlength . concentration \tag{4.2}$$

In general however, CD spectra were collected purely in order to confirm peaks present in the absorbance spectra, and also to potentially uncover additional peaks missed. Collection of spectroscopic data for both calf-thymus DNA and M13 phage required no additional special preparation. The A-DNA conformation was prepared from calf thymus B-DNA stock solution (1 mg/ml, in purified water). Purified water was added first (3.3 ml) to 0.584 ml of this stock DNA solution followed by slow addition of pure ethanol (to a total of 19.4 ml) with careful stirring (to avoid precipitation), to make an 80% ethanol solution at 30 μg/ml DNA. The stock solution was diluted to 30 μg/ml with purified water for the control B-DNA conformation[63].

4.1.1 Cell preparation

Fresh defibrinated equine blood (screened for viral and other pathogens to ensure sterility) and fission yeast samples (stored in simple growth media) were stored at 4 degrees and used as received. Equine RBCs were initially isolated from the blood stock solution by centrifugation at 600g for 10 min at room temperature. Volumes were such that there was a ratio of 1:2 with regards to blood:buffer (e.g. 100 μl of blood required 200 μl of buffer)[57]. After the supernatant was removed via careful pipetting, the RBC pellet was resuspended in cold isotonic PBS (0.9% NaCl, 5 mM phosphate buffer, pH 7) by trituration (passing the surrounding solvent over the pellet repeatedly via micropipette, within the preparation vessel) and then re-centrifuged at 600g for another 10 min. The cell pellet was then washed with PBS buffer thrice to completely remove the plasma and buffer layers (washing twice was acceptable if the supernatant was almost clear after the second wash). The final preparation of washed RBCs was resuspended in isotonic buffer at 0.5, 1 and 2% PCV (Packed Cell Volume, volume of blood cells in a given volume of solution). Lysed red blood cell samples were prepared by simply diluting a given concentration of cell pellet into phosphate buffered purified water.

Fission yeast samples were prepared in a similar manner as the intact RBC samples however the yeast cultures were of a much lower cell concentration compared with blood stocks, despite having been grown to the limit possible without inducing stress reactions (grown in 50 ml vessels). Therefore in order to obtain sufficient

quantities of cells to form the final cell pellet, increased quantities of yeast media was required (4ml of yeast media versus <1ml for blood). The resultant cell pellet formed from 4ml of this media was then suspended in 200 μl of purified water to create a stock solution and successive dilutions were taken as specified.

4.2 Analysis method: Component Gaussian decomposition

In general when dealing with systems that contain more than one absorbing component, analysis of the peak contribution that each component has within that spectrum can be alternately simple or complex. Simple systems, comprised of either pure absorbance or CD exempting complications as will be discussed in the following subsection, result in spectra that should be directly comparable to a summation of the spectral peaks produced by its components (e.g. any chromophores for absorbance, chiral chromophores for CD). A weighting effect would then also be applied for each component spectra with regards to its concentration within that system, (i.e. concentration correction according to the Beer-lambert Law). The latter more difficult systems are typically LD and complex CD, which cannot be simply calculated from the individual spectra of its component molecules (since typically the component molecules are too small and not sufficiently uniaxial to flow align). The difficulty arises by having components that have similar transition wavelengths, or by having numerous components within that system many of which will change their spectral characteristics upon interacting with another molecule. Instead it must be constructed from the absorbance spectra peak shape and pattern for each component (after all LD spectra are constructed from absorbance difference spectra). For example, determination of whether a peak for one component has wavelength shifted when several others of the same or similar wavelength overlay its absorbance peak.

Despite the above complexities, it is valuable to endeavour to relate multicomponent spectra to those of the component parts. A method therefore is required for which to quantitatively break down a multi-component system spectrum into parts that can be assigned to each component, which may then be analysed. In this work the approach taken when dealing with multicomponent systems was to mathematically decompose each dataset into a set of Gaussian peaks[58]. This approach

was then also taken to the pure absorbance spectrum from each absorbing component within that system (i.e. the 'component Gaussians'). The contribution from each of these component Gaussians can then be overlaid onto the main set of Gaussians that comprise the entire dataset. Not only does this method allow for the analysis of any changes to component behaviour when placed in the system (e.g. peak shifting, intensity changes) but also for the examination of unknown systems. Theoretically once an initial database of component Gaussians is constructed (as is demonstrated elsewhere for aromatic amino acids and nucleobases), given a known content of a particular component, the corresponding peak contribution will then return information regarding both the component composition and orientation relative to that of the overall system.

4.2.1 Software implementation

All spectra were fit with a number of Gaussian curves relying on the curve-fitting toolbox within the software package *Matlab*. The term 'fitting' here is used to denote the minimal number of Gaussian curves, and the associated parameters to define the curves, required to imitate the original spectrum when taking a sum over all Gaussians (the appropriate number as determined by space-scale filtering, mentioned below, at a 10% threshold standard deviation). Firstly the wavelength parameter was converted to frequency (necessarily this was applied to all LD spectra) to improve fitting of the Gaussians. In short this is because the key parameter related to an absorbed photon is the frequency (since that's the connection to energy via Planck's Law), and it is the energy of this excited transition that is Gaussian distributed. Since it is this frequency function that follows the Gaussian distribution, taking the same function in wavelength space (essentially fitting the absorbance as a function of wavelength, which is how the absorbance/LD machine outputs its results), results in peaks that are technically no longer Gaussian.

Initial parameter values were estimated from each respective absorption spectrum then optimised via the use of a Trust Region algorithm, a sub-set of the non-linear Least Squares family of algorithms[59]. The general approach from this family of algorithms is to determine a set of parameters (which in our case are the three

parameters belonging to the Gaussian function for each Gaussian in our fit) that minimises the sum of the squared errors (residuals) when fitted against the actual data. The trust-region essentially improves the optimisation by approximating the function for a particular data point on the curve with a simpler version that applies within a small neighbourhood around that point. Next a trial step can be made by minimising the sum of squares within that neighbourhood, from that data point. This is applied iteratively until no further improvement can be made.

4.2.2 Space-scale filtering

In order to accurately determine the correct number of Gaussians to assign for a particular spectrum (since assigning an arbitrary number would easily lead to over-fitting and confuse analysis of the final LD spectrum) a process known as 'space-scale filtering' was used in order to analyse the cumulative contribution of multiple Gaussians within a spectrum[58]. The technique first employs a Gaussian low band-pass filter in order to smooth the data, and then calculates an approximation of the second derivative of the resultant data. Logically each Gaussian present in the signal should then present itself as two x-axis zero point crossings (exceptions are possible when Gaussians means are very close, or there is a large degree of disparity between their sizes). The wavelength position of all zero-crossing points for each value of the standard deviation can then be plotted against each other. This is known as a scale space image (SSI), Fig. 4.1[60]. At very low absorbance intensities, 305-350 nm Fig 4.1, there is a degree of signal fluctuation that is negligible in contrast to the rest of the spectrum. However when the second derivative is taken, this fluctuation results in a dense 'false-positive' region of zero-point crossings. When examining the resultant SSI therefore a threshold needs to be set which disregards standard deviations below it, so that only peaks of a set intensity are considered. This is conducted by allowing the initial smoothing kernel that the smoothing algorithm uses to have a very low standard deviation initially in order to capture the full un-smoothed signal. The standard deviation of the kernel is then steadily increased to remove Gaussian contributions from the spectrum until the required threshold is met.

The peak and trough wavelength values corresponding to each Gaussian in the spectrum dataset can then be extracted. Calculation of this SSI therefore essentially acts as a guide for an appropriate number of Gaussians present within a given absorbance spectrum. Despite not being capable of precisely stating the peak positions (most likely due to the influence of the underlying baseline scattering contribution) the approach can also provide some good starting values for their parameters (i.e. initial estimates for the peak wavelength for each Gaussian) which to feed into the algorithm necessary in order to fit a given spectrum. Once the correct number of Gaussians (and initial parameters) is obtained for a given spectrum, that spectrum can then be reconstructed in terms of Gaussians peaks by means of the *Matlab* Trust Region algorithm as mentioned above, Fig 4.2.

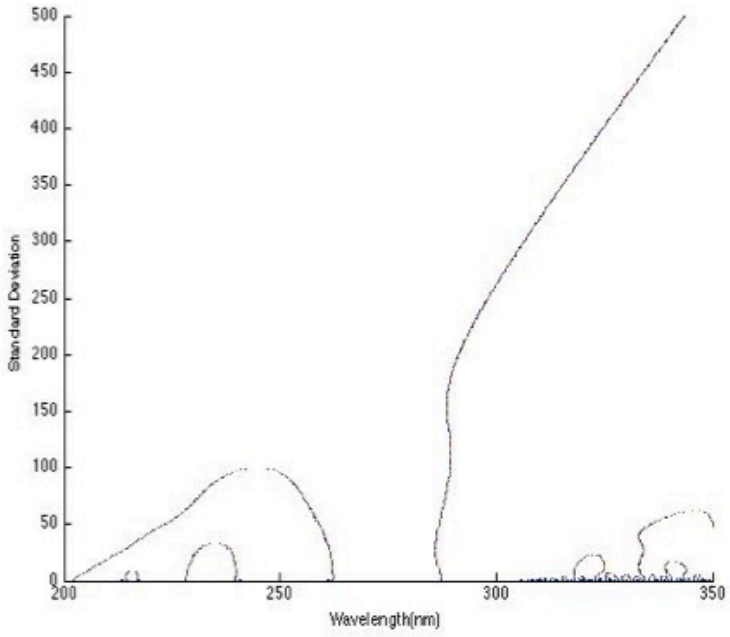

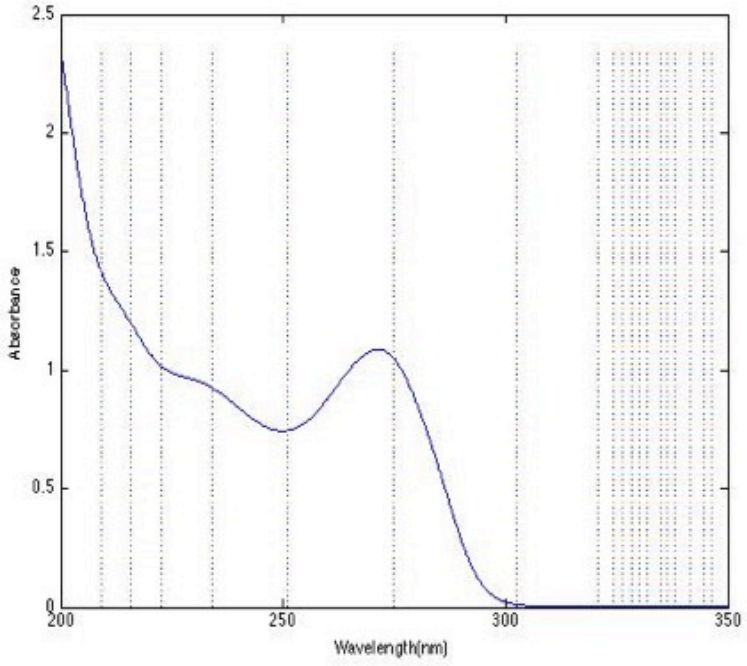

Figure 4.1: *Top* Space Scale Image of CMP (UV-Vis Absorption Spectrum). *Bottom* UV-Vis Absorption spectrum of cytosine with peak Gaussian contributions labelled (vertical lines).

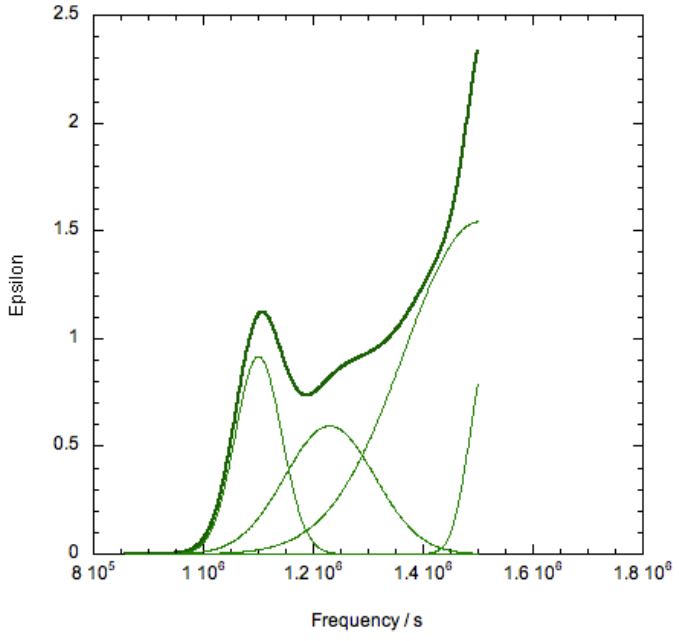

Figure 4.2: Example of the Gaussian fitted curves (Bold) and component Gaussians (Hairline), for CMP absorbance spectra.

The limitation to this modelling concept as a whole is that at this point in time this cannot be used as a quantitative process without application of the equation below, Eq 4.2, in order to convert the raw LD data to the isotropic absorbance (that can then be simply converted to ε via the Beer-Lambert Law, Eq. 4.1):

$$\mathrm{LD} = \frac{3}{2} A_{iso} S(3cos^2\alpha - 1) \tag{4.1}$$

One difficulty with this approach is that the value for S (orientation parameter) for the sample is an unknown since the relative orientation for each component is unknown. When analysing spectral data in the following sections from multi-component systems this approach was applied.

4.3 Complications

The topic of DNA helices, particularly in the field of LD and flow orientation, has been well documented in the past[20]. Because of this, it presents the perfect example in order to outline some of the potential difficulties regarding analysis of any absorbance-based spectra as a composite of the component peak intensities. In general, when dealing with mixtures of particles, the corresponding absorbance or circular dichroism (since no shear alignment is required) spectrum of the mixture can be reconstructed from the spectra of the component particles within the mixture that absorb (given the concentration weighting of each particle type). However, it has been well established in the literature that certain inter and intra-particle interactions can cause changes in a particle's spectrum. This can easily be seen when analysing a phenomenon known as 'hyper/hypo-chromism', essentially a change in the absorbance intensity of a sample. In this instance the concentration of a chromophore (absorbing part of the sample) within a system influences the resulting absorbance spectrum of that system[109] (similar to what was demonstrated with the self-quenching of fluorescence with calcein in Chapter 3)[46]. Using the system of a DNA strand as an example (as is demonstrated

below), it has been observed in the literature that variable peak intensities result dependent upon the distance taken for one rotation along the DNA helix (i.e. the 'tightness' of the DNA coil)[20]. This is due to the altered distance between the nucleotide bases (DNA chromophore) within the strand. Another subsequent effect that has been observed is that the resultant CD spectrum cannot be accurately reconstructed from the individual CD spectra from the DNA strands nucleobase composition, although the effect regarding LD has not been fully explored. This needs to be clarified and the impact of possible intra/inter particle interactions on the overall LD spectrum understood.

4.3.1 CD nucleobase – DNA calculation discrepancies

Since calf thymus DNA has been fully characterised, the exact composition of the strand in terms of component nucleotide weighting is known (~60% AT and 40% GC). The next step is to obtain the corresponding component nucleotide absorbance and CD spectra, collected in an identical manner (to minimise discrepancies caused by variations between experimental setups).

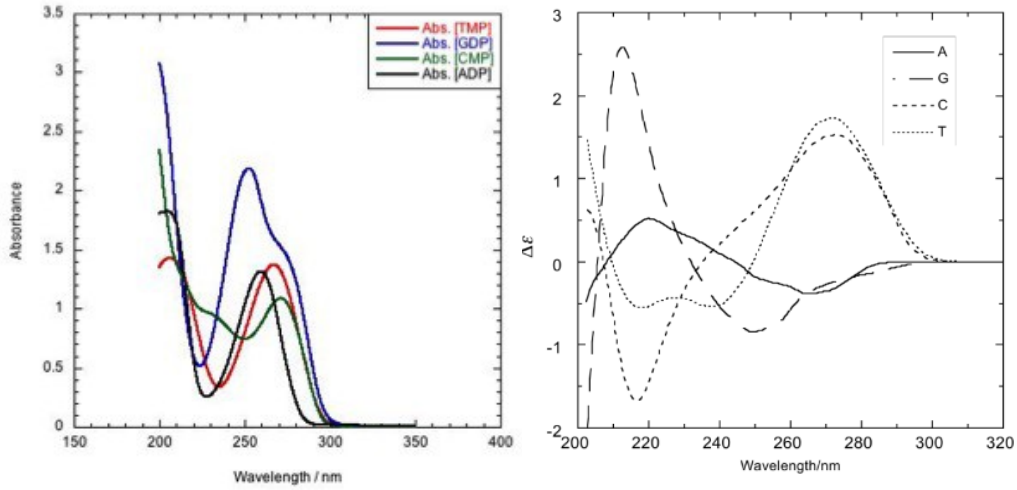

Figure 4.3: Component spectra for each of the DNA nucleotides, *Left* Experimentally collected absorbance data (GDP 216 µg/ml, ADP 118.5 µg/ml, CMP 175.2 µg/ml, TMP 217 µg/ml, pathlength = 1cm). Samples were concentration corrected and zeroed at 350 nm (absence of absorbance). *Right,* Literature representation of the CD spectra given from each of the pure nucleotide bases.

Each nucleotide component has its inherent chirality granted by the ribose sugars, and these sugars contribute negligibly to the resultant absorbance above 200 nm[54]. The corresponding bases each have their own set of transitions from which the resultant absorbance spectra arise.

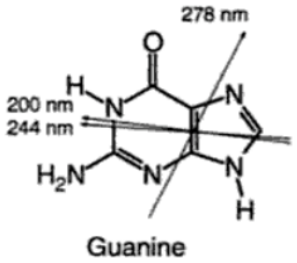

Figure 4.4: Literature estimated transition moments for the nucleotide base, Guanine[61].

Most of the component absorbance peaks, Fig 4.3 (*left),* are represented in the corresponding literature CD spectrum (with only minor peak shifts) with changing sign of the transitions occurring for some peaks, such as the ADP peak at 256 nm. Regarding the collection of experimental CD data collected from each component, Fig 4.5 (*left)*, there are noticeable differences with the 'ideal' literature values[61]; resolution is lower and some CD peaks are not detected, most noticeably those corresponding to the transition wavelengths from GDP. Unfortunately, in general the sensitivity of CD suffers greatly when dealing with particles with a low intensity absorbance, as can be seen by the spectra of highest resolution being AMP/CMP (the two bases with the highest CD peak intensities within the ~220-350 nm range). Although this can be bypassed via the use of higher concentrations, current equipment limitations prevent this (extreme absorbance leads to a significant drop in the accuracy of detection).

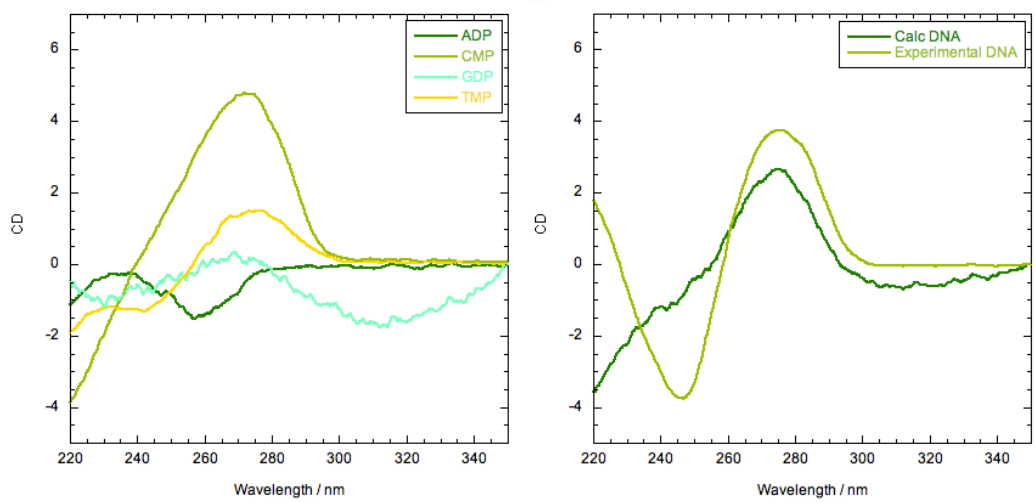

Figure 4.5: Contrast of the calculated DNA CD to actual DNA CD spectra. (GDP 46µg/ml, ADP 118.5µg/ml, CMP 175.2µg/ml, TMP 217µg/ml, DNA 260 µg/ml, pathlength = 1cm with the exception of GDP which was 1mm to optimise recordings). Samples were concentration corrected and zeroed at 350nm (absence of absorbance).

After concentration correction, and according to the nucleotide weighting of the calf thymus DNA strand, a CD spectrum was calculated based on the CD spectra produced from each individual nucleotide and plotted against the equivalent CD spectrum of an intact DNA strand. As evident, calculation of a CD spectrum of helical DNA based on individual nucleotide data is not particularly successful. Although the primary peak position has been correctly assigned a considerable loss of resolution regarding the peak shape, such as the loss of sub-peaks as observed at ~280 nm, Fig. 4.5 (*right)*. In addition, the calculated spectrum does not demonstrate the large positive to negative peaks as seen in the DNA strand, instead simply decaying in intensity, as the wavelength decreases. The latter of these effects are caused by a phenomenon known as exciton-coupling occurring between all of the overlaid nucleotide bases within the DNA strand, generally represented by a pair of distinct paired positive and negative transitions[62,54]. When the chromophore region in a molecule is excited (as is the case in our absorbance and dichroism spectroscopy), we can view it as an electron jumping to a higher energy level leaving behind a corresponding electron hole. The bound state of an electron and electron hole (via the attractive Coulomb force between them) is known as an exciton. When there are two or more of these chromophore

species in close proximity within the particle (such as the nucleobases within a DNA strand) these excitons can 'couple' together. In this case, their individual peak transitions interact and can form two distinct bands of opposite transition sign in LD and CD also. This is also a significant factor regarding LD, in which exciton coupling can also occur, complicating analysis further.

An example of this exciton coupling can be seen in the DNA CD spectra where there is a clear negative peak at ~ 245 nm and positive peak at ~260 nm, Fig. 4.5 (*right*). As shown in the literature spectra, Fig. 4.3 (*right*), there appear minimal peak intensities for each component significant at this wavelength, although there is a strong CMP peak between them at ~255 nm. The CD spectrum of helical DNA is influenced by interactions produced via the stacking of the aromatic bases in the 3D geometry of the DNA strand, however since these interactions are dependent on distance and geometry, isolated nucleotides cannot produce this effect. Therefore the corresponding CD spectrum produced by a given DNA strand is influence by both the sequence of bases comprising it, but also by the geometry of the strand itself. In general however, studies in the literature have demonstrated[54] that the intensity of a given DNA spectrum has a stronger reliance upon the geometrical state of the strand (e.g. the shape and tightness of the coil) than the actual nucleotide base sequence. To demonstrate this effect upon the CD spectrum, DNA samples which were primarily of the B-DNA form were mildly dehydrated via a dilute ethanol solution in order to widen the radius and lower the rise/turn of the DNA helix (to more closely represent the A-DNA form)[63].

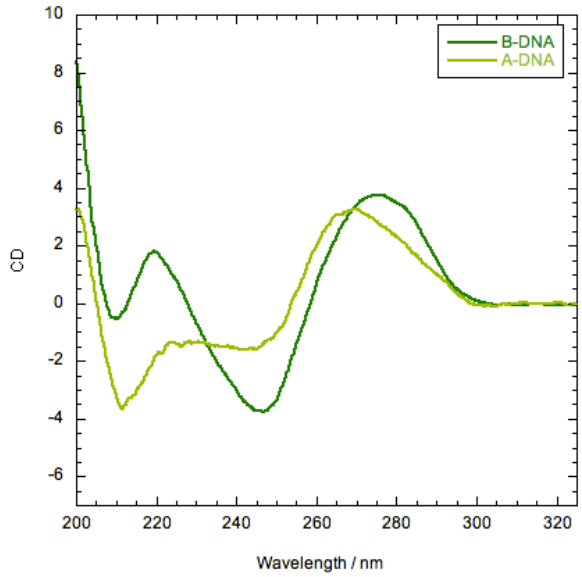

Figure 4.6: Representative CD spectra for both A (30ug/ml) and B (260ug/ml) isoforms of DNA. A-DNA was concentration corrected via the Beer-lambert Law, to be equivalent to B-DNA), Samples were zeroed at 350nm (absence of absorbance), pathlength = 1cm.

As expected, we can see that although the peak positions have remained mostly untouched (with only a minor upward frequency shifting of the exciton coupled peaks) between the two forms the shape of the curve is greatly different thanks to the change in DNA polymorph changing the behaviour of the exciton coupling between nucleotide bases. Features such as the altered helical twist, sense, pitch, and base inclination all serve to alter the relative base orientation, in addition to the decreased inter-base distance as the polymorph shifts from B to A. Lastly regarding the application of DNA for LD, due to its long semi-rigid nature it aligns strongly under induced shear flow and its component nucleotides strongly absorb, resulting in a distinct and reliable LD spectrum (the model system of use in this work being that of Calf Thymus DNA, Fig.1.4).

4.4 LD fitting and component peak assignment

Spectra (LD, CD and absorbance) were collected from several systems of increasing complexity with regards to the number and variety of component chromophores. To begin with an examination of calf-thymus DNA spectra was carried out, a system that can be considered to be consisting of a single component (nucleobase) albeit in four

variations. Next was a virus, M13 phage, in which the system now also includes elements of a protein coat contributing to the spectrum[64]. Then preliminary spectra were collected from blood cell samples, the simplest variety of mammalian cell. This introduces the structural membrane-related elements of cells without the complex internal organelle structures (e.g. DNA, ribosomes, mitochondria etc) that cells usually comprise, instead predominantly containing the protein *hemoglobin*[65]. Lastly there are those of fission yeast, essentially standard eukaryotic cells that are sufficiently uniaxial under flow to give a measureable LD signal[66]. The initial LD and absorbance spectra for system were decomposed into its individual Gaussians, as were the spectra from each of its components. The resultant matching between these two sets of Gaussians then allowed for a closer investigation of peak shape and position matching within these systems.

4.4.1 Calf-thymus DNA

The Gaussian space-scale fitting approach was applied to calf-thymus DNA spectra reported previously, Fig 1.4. This method permitted a direct contrast of component fitting regarding LD data against that of the simple CD fitting. Each nucleobase was fit with minimal Gaussians (SSI set to 5% std. deviation for data with absorbance intensity above 0.05) and a composite absorbance spectrum was calculated based on the same 60/40 nucleobase pairing ratio. Since for this initial contrast the orientation values are unknown, therefore LD intensity and transition cannot be analysed, data for both the composite nucleobase and DNA spectra were normalised between values of 0-1 (consequently converting the LD transition sign to positive to more accurately compare peak positions). This approach should still permit the accuracy of peak and shape matching from the fit to be analysed, and determine the extent effects such as π - π^* stacking (electron orbitals related to aromatic base stacking) influences the composite. The composite spectrum was compared against both the DNA LD spectrum and its equivalent fitted absorbance (as a form of validation). Although it was expected that the same π - π^* stacking influence responsible for the inadequate fitting with regards to CD would occur again here (e.g. peak shifting, or relative peak amplitude changes), it would appear that LD seems to be influenced to a lesser degree

by base stacking interaction compared to the CD spectra. The calculated curve, Fig. 4.7, resembles the actual absorbance data collected for calf thymus DNA and closely matches both the primary 1.15 Hz peak value and shape present in the LD spectrum, Fig 1.4. Higher frequency data however can be seen to be much harder to fit (as has also been demonstrated in equivalent CD calculation) since that is approaching the detection limit for absorbance (200 nm = 1.5×10^6 Hz) on the equipment.

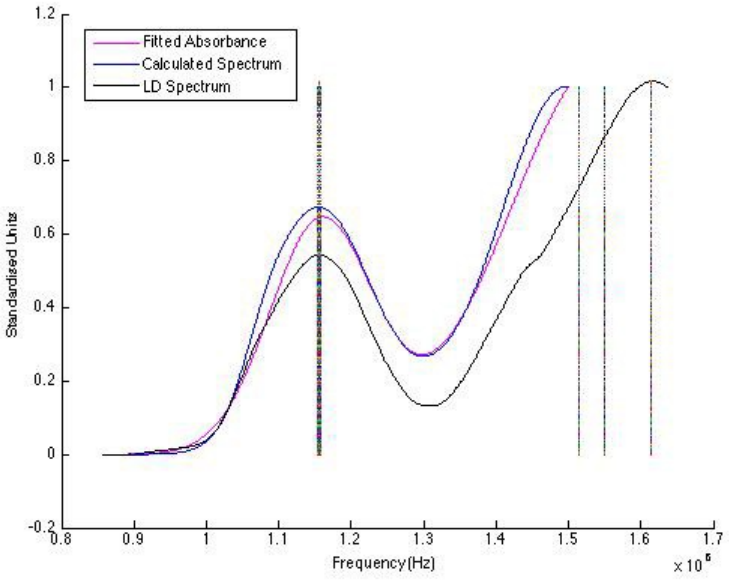

Figure 4.7: Overlay of the normalised calf-thymus spectra from composite nucleobase absorbance fitting (magenta), and DNA absorbance (blue) and LD (black). Vertical lines represent peak values.

4.4.2 M13 Phage

M13 is a strain of virus from the phage family that infects only bacteria[64], (most commonly examined using *Escherichia coli* as a host). The phage primarily consists of a capsid, constructed from numerous coat proteins, Fig 4.8, with the viral genome (DNA) held inside the capsid (there are additional proteins related to the infection process, such as the membrane adsorption protein gp3[67], however, they are present in considerably smaller quantities) and so the phage may be treated as a simple 2-component DNA/protein system in this work.

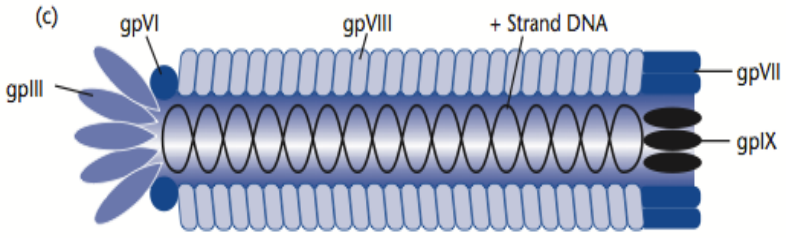

Figure 4.8: Schematic depicting M13 bacteriophage and key capsid proteins[78].

In order to apply our fitting approach firstly the component spectra database mention above must be extended to now take into account the far-UV (~180-280 nm) absorbing amino acids (aromatic Trp, Tyr, Phe) and so absorbance/CD spectra were collected (Appendix A.2). In a similar fashion, the aromatic amino acid component spectra can be broken into component Gaussians and the peak positions of each determined. When overlaid onto the M13 phage LD spectrum this can then return a map of the component contribution within the sample, Fig 4.9 (additional work-up could also be conducted in order to display the relative peak intensities on this map.

In addition the M13 absorbance spectrum can also be fit in a similar manner to calf-thymus DNA (as shown previously, Fig 4.7). This approach permits the analysis of the peaks within a given spectrum in terms of the various contributions that comprise its individual component chromophores for situations where multiple chromophore signals may overlap and complicate analysis. In addition, by comparison between the relative intensities of the component Gaussians required for the production of a given M13 peak the relative contribution from each can be analysed (in relation to component concentration and orientation). Additionally by correlating the main signal peaks from the absorbance onto the LD we can determine another instance of exciton coupling for the peak at 1.1×10^{6} Hz (273 nm), which due to the broadness of the peak was not immediately obvious upon visual inspection, (Appendix A.3).

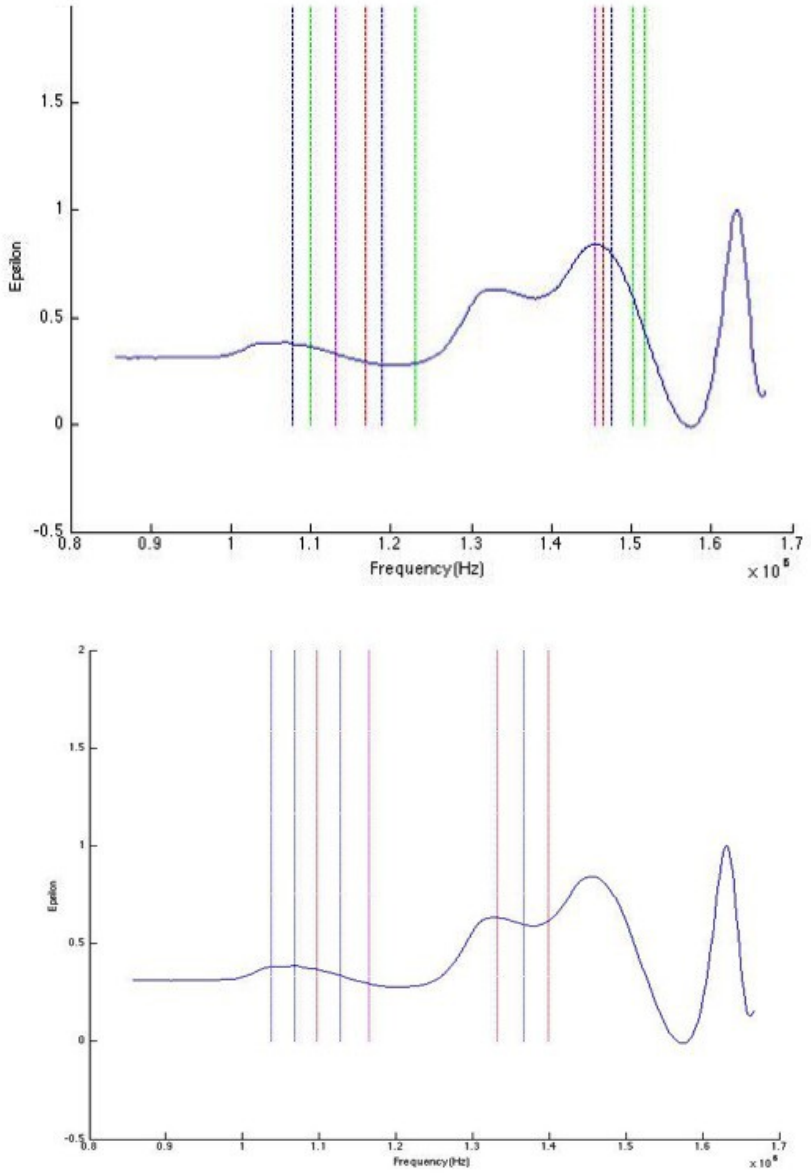

Figure 4.9: Spectra overlay of M13 LD with peak component Gaussian values represented by vertical lines; *Top*, [Trp (Blue), Tyr (Orange) and Phe (Magenta)]. *Bot*, [GDP (Blue), ADP (Red), TMP (Magenta) and CMP (Green)].

4.4.3 Red blood cells (RBCs)

Under ideal circumstances the next stages would be to introduce variation in protein consistency of the capsid coat in a virus of the same structure, to analyse the shifting of peak intensities and position, however, the time investment that would be required to accomplish this was unfeasible. Since this is the case, an alternative was explored in the field of mammalian cells, namely red blood cells. Regarding the standard

mammalian erythrocyte, such as human blood cells and those from equine sources as used in this work, the basic geometry of the cell is that of a biconcave disc with a thick rim (torus-shaped) and a dumbbell shaped cross-section[68]. The primary purpose for this shape is to facilitate the transport of the cells via blood (laminar) flow and the transport of oxygen due to the increased surface area[69].

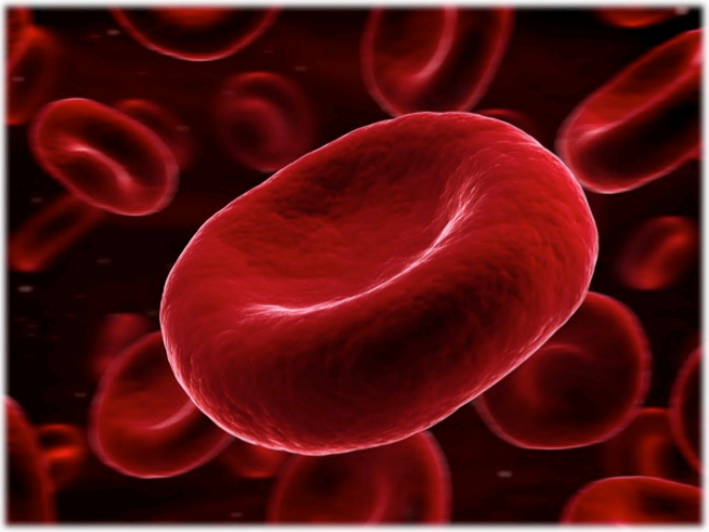

Figure 4.10: Graphical representation of red blood cell in flow[77].

Aside from its usual geometry, red blood cells present a typical mammalian cell membrane, with the exception of a few specialised structural membrane proteins (e.g. Band III)[70]. Additionally inside the cell there exists an extensive cytoskeleton protein network spanning the interior surface of the plasma membrane[71]. Although these structures exist within all cells, in order for red blood cells to perform their biological role they must demonstrate high levels of both flexibility and durability. Since the cells lack any sort of cell wall, this biconcave geometry must be maintained by the internal cytoskeleton at all times despite the variable shear rates present in differing blood vessels.

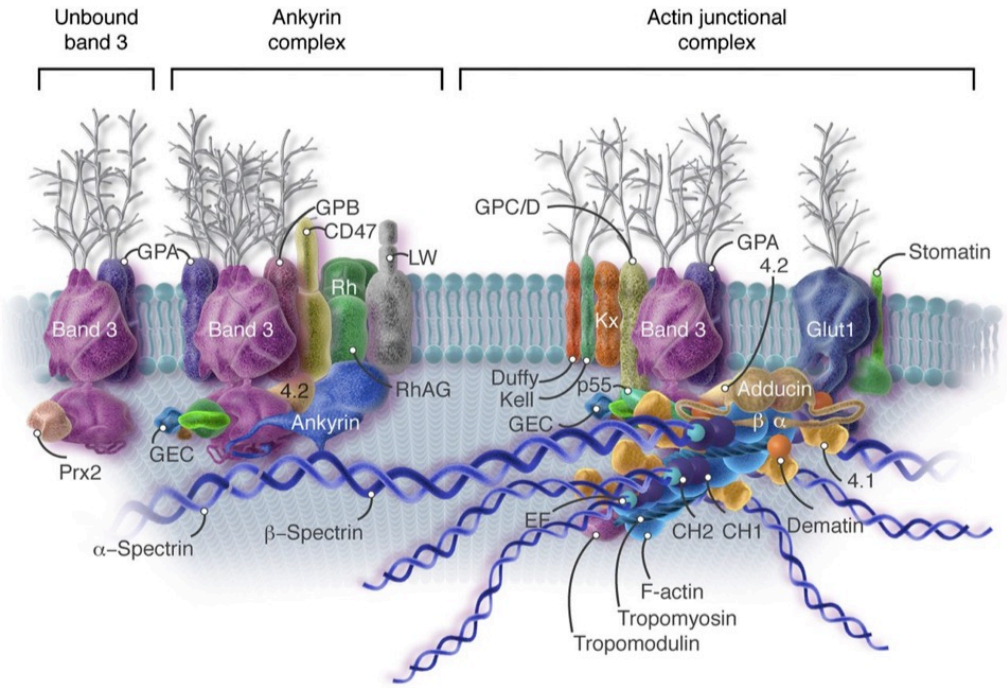

Figure 4.11: Demonstrating of a red blood cell plasma membrane with a variety of integral and structural proteins.[72]

However, aside from these membrane related structural proteins discussed above, Fig 4.11, the bulk cytosol of red blood cells have been shown to contain little else other than a plasma solution extremely rich in the metallo-protein hemoglobin. There are no internal structures present such as organelles or any significant proportions of DNA. Regarding the resulting LD spectrum, the only components that should be present in the LD spectrum should relate to the phospholipid bilayer and related structural components. Essentially what erythrocytes permit, over the use of an alternative mammalian cell, is to examine the extent to which associated structural components influence the spectrum, without further complications from the internal environment. In addition, the biconcave geometry of the cell should aid in the ease of shear flow alignment by virtue of having a more extreme axis ratio that most other cells (resulting in a more intense LD spectrum). Erythrocytes are highly deformable permitting safe transfer within blood capillaries, but also when the cells are stretched under shear flow this not only ensures membrane integrity but also a greater degree of alignment. The extent to which both of these facets influence flow orientation has already been studied in the literature[68,69].

RBCs can be essentially considered to be another 2-component system, the primary components being the membrane associated and related structural proteins (e.g. glycoproteins, cytoskeletal elements), and the highly concentrated internal hemoglobin environment (which studies in the literature suggests is also likely to demonstrate associations with membrane related proteins, such as Band 3[73]). There is the potential additional component of membrane lipid absorbance, but is unlikely to be of sufficient intensity to be noticeable above 200 nm.

4.4.3.1 Component: Hemoglobin

Regarding component orientation, the primary source of LD signal should be originating from membrane associated molecules instead of the protoplasm, since cellular alignment (and therefore membrane alignment) is crucial to preventing a null LD response and given any detectable LD can be assumed to exist. If the cells within the sample were to favour free-rotation over flow orientation the average orientation of all components would become uniform and thus return no noticeable difference in absorbance of vertical/horizontally polarised light. LD appears to be influenced by inter-particle effects (such as pi-stacking, as demonstrated with DNA) to a lesser degree in contrast to CD and as such that the various protein components can be understood in terms of the previously collected aromatic amino acid spectral database. However hemoglobin contains the pigment heme that, thanks to its porphyrin ring, presents a spectrum which both absorbs more intensely (with regards to the ~180-350 nm protein secondary structure absorbance), at more numerous peak wavelengths and over a wider wavelength[58].

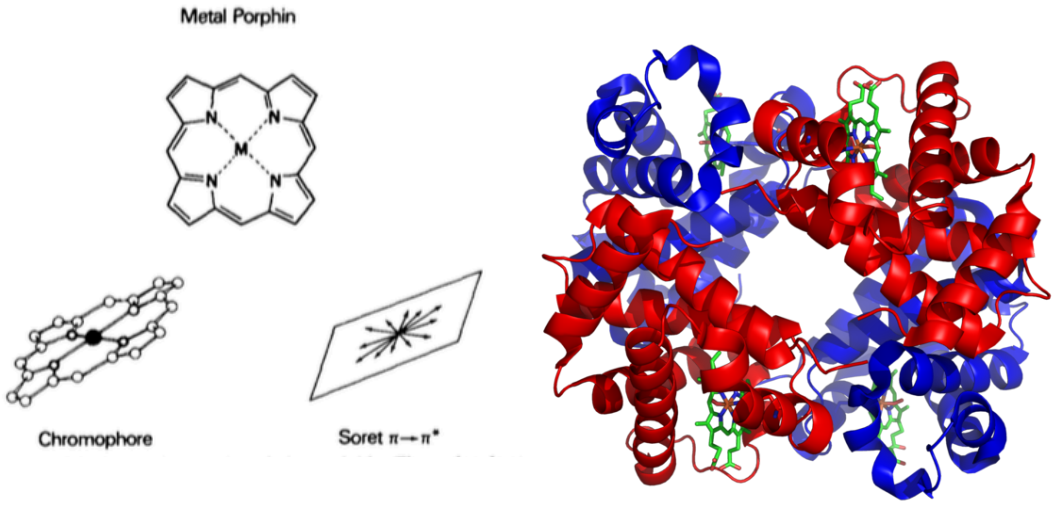

Figure 4.12: Illustration of the core square planar form of the porphyrin based heme chromophore (and the plane in which the primary Soret π – π* bands absorb) and as part of its parent protein hemoglobin (*right*), [Source PDB, 1GZX, porphyrin rings are defined in green][65].

Despite being documented in the literature[65], in order to have a reference spectrum for hemoglobin peak shape and positions for use in this work and in order to be capable of contrast relative peak intensities, hemoglobin spectra were collected. Samples were sourced from lysed fresh red blood cell solutions due to the red blood cell cytosol being comprised of a highly concentrated hemoglobin solution. Red blood cells do not have a cell wall, upon dilution in purified water the cells rupture releasing a rich hemoglobin solution into the surrounding solution. Since we are extracting directly from fresh cell stocks, the protein will still be oxygen bound and present the oxy-hemoglobin absorbance spectrum[75].

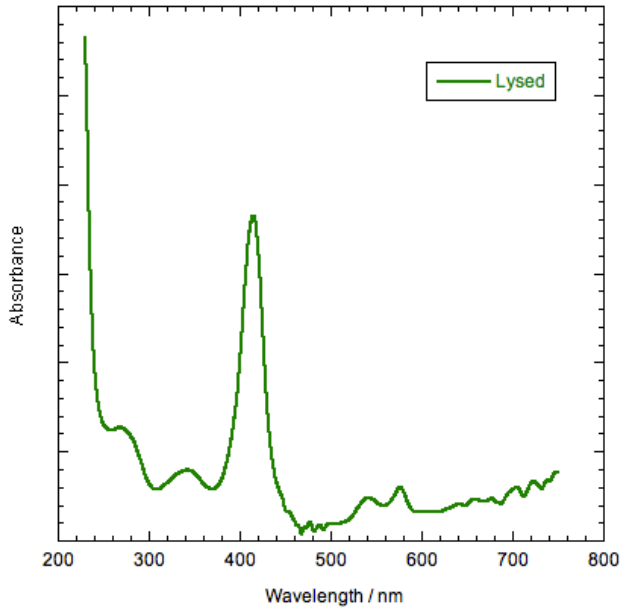

Figure 4.13: Representative absorbance spectra for lysed cell preparations [conc. 1.5% PCV, pathlength = 1mm].

The spectrum of Fig 4.13 can be broken down in terms of its peak transitions[74]. Firstly there are the far-UV peaks at ~200–350 nm commonly denoted as the N and M bands. Then there are the Soret (or B bands) in the near-UV to visible wavelength region at ~ 400–436 nm. Lastly are the Q bands in the visible region at ~490–650 nm. The latter two, the B and Q bands, are of most importance to this work because they both correspond to the $\pi - \pi^*$ electronic transitions and are outside the protein absorbance regions. The Q band exhibits a weak absorbance intensity and it corresponds to a transition to the first electron excited state and by way of contrast the B band demonstrates a stronger intensity corresponding to a transition to the second excited state. These states correspond to different energy levels that electrons can reach when excited by incident light, (the first state being of a lower energy level than the second). From studies into the absorbance from hemoglobin crystals, Fig. 4.12 (left), the intensity of both B and Q band transitions relate to the plane of the *heme* group within the protein. Hemoglobin, characterised as a 'planar absorber', has been shown to absorb light at B/Q transition wavelengths to a greater degree when the incident light is polarised parallel to this *heme* plane[65]. Since these both share the same transition polarisation (aka positive LD peaks), albeit of different intensities and wavelengths,

they then also share the same increase in absorbance when polarised light is oriented parallel to the plane of the heme chromophore.

The intensity of the B and Q bands are also very sensitive to the various different forms of hemoglobin. This is most commonly observed for the different oxygenation states, as the binding of oxygen aids in the fitting of the iron atom within heme ring to assume the observed square planar structure[65]. In the absence of bound oxygen, the iron atom is too large to sit perfectly within the heme plane. The influence of changes such as this can be most clearly seen in the literature when contrasting the peaks observed in the B and Q-band regions, Fig 4.14.

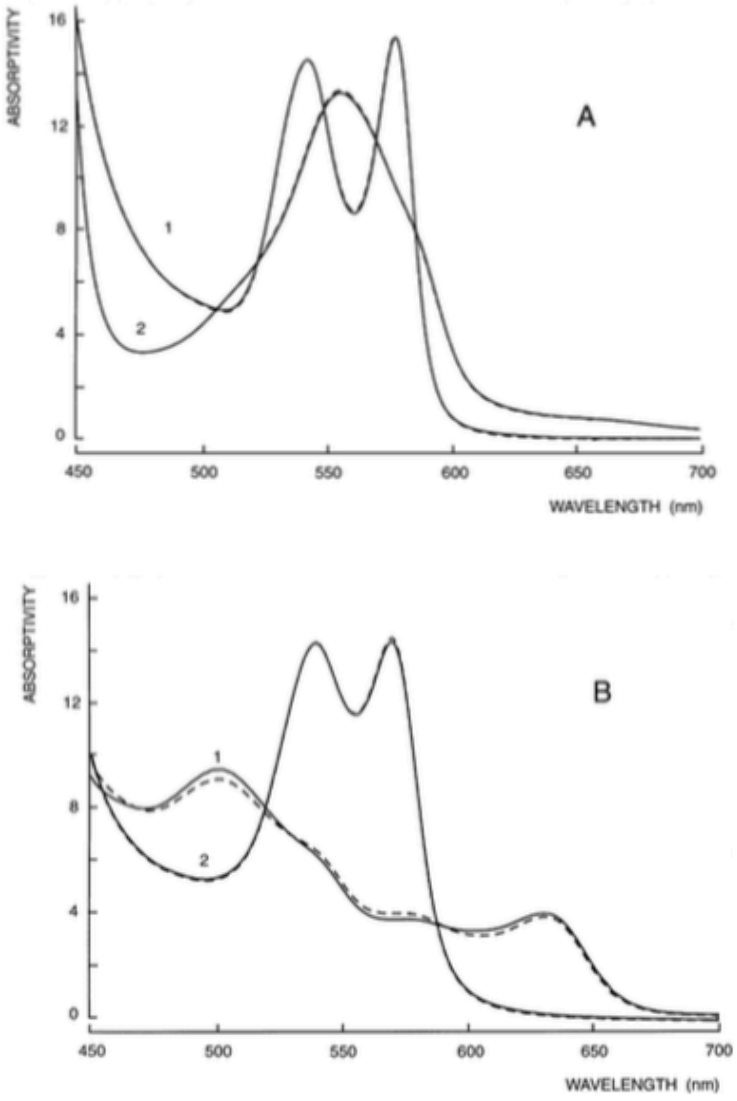

Figure 4.14: Literature absorption spectra of the common derivatives of bovine (—) and human (– – – –) hemoglobin in the visible range. (A) oxyhemoglobin (1) and deoxyhemoglobin (2); (B) methemoglobin (1) and carboxyhemoglobin (2)[75].

Ideally however, when collecting component data the sample should contain exclusively oxyhemoglobin, which can be obtained sourced from lysed fresh samples as conducted in this work or either preserved and powdered. Each has its own advantages and disadvantages: powdered samples run the risk of alterations to the protein structure occurring as a result of the preservation process, alternatively lysed samples suffer from residual membrane or plasma remaining in the solution (since it difficult to remove red blood cell ghosts, empty RBC membranes, via centrifugation due to their light weight). Initially pure powdered samples of 'oxyhemoglobin' were obtained from Sigma, UK and the spectra recorded (resuspended in purified water).

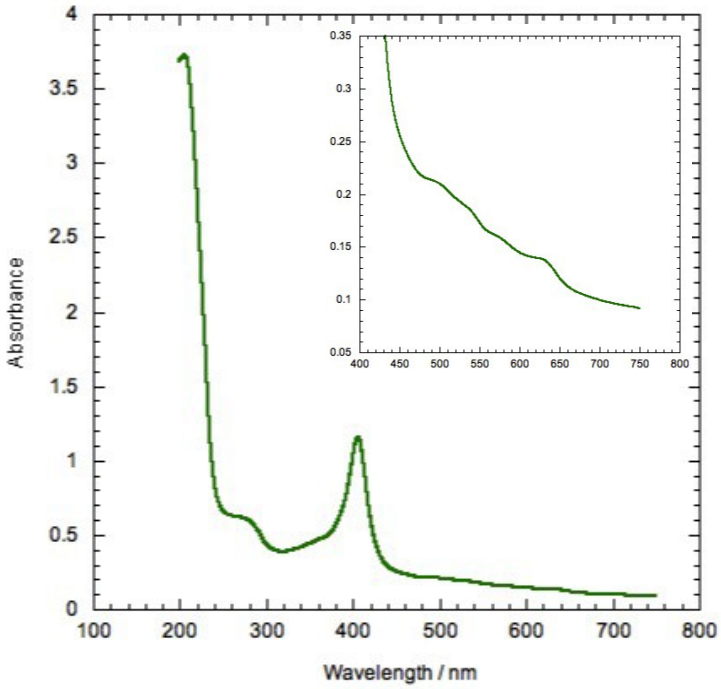

Figure 4.15. Absorbance spectrum for powdered haemoglobin suspensions; *Left*, full spectrum. *Right*, expansion of the hemoglobin low intensity region containing the porphyrin Q-bands.

The spectra displayed in Fig. 4.15 collected on solutions made from powdered 'oxyhemoglobin' appear to portray the characteristic peaks stated in the literature for the Soret band peaks found in oxyhemoglobin. However, the lack of the distinct twin

Q band peaks in favour of an equally intense quadruplet, and the shifting of the Soret band from 415 to 405 nm suggest that sources of powdered hemoglobin (by nature of its preparation, and suspended in solution) are in fact aquo-methemoglobin thanks to oxidation due to the drying/preservation of the protein. This demonstrates the inherent risk behind preservation protocols when using reactive metal-binding proteins.

Therefore in order to obtain the necessary hemoglobin component spectra this necessitates the sourcing of fresh hemoglobin prepared instead from lysed cell samples. Although this is less ideal due to the imprecision inherent in concentration determination from cells of indeterminate concentration (despite knowing cell density of the samples under examination) the same peak position and shape comparison, regarding the hemoglobin absorbance peak contribution to the resultant RBC LD spectra, should be possible as demonstrated for M13 and DNA. An advantage however is the capacity to contrast a given cell suspension directly to that of its lysed absorbance. This allows for a direct examination of any inter-protein effects occurring as a result of the close protein packing within the cell. However, this potential residual contamination is a concern for future work if attempting to relate relative component peak intensities to the extent of orientation.

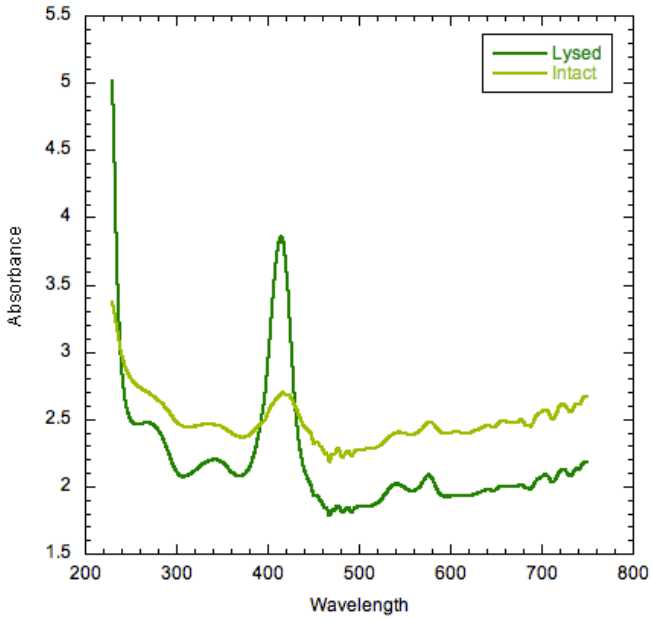

Figure 4.16: Absorbance spectra for intact and lysed cell preparations, (lysis by replacement of cell buffer with purified water.) [conc. 1.5% PCV, pathlength = 1mm]

As demonstrated in Fig. 4.16, both intact and lysed samples match peak reference values for oxyhemoglobin, however, a couple of interesting aspects can also be seen from the intact (non-lysed) red blood cell control sample. Firstly there is the change in absorbance baseline across the entire UV-Vis wavelength range. This can be attributed to a change in light scattering that is caused by the extremely densely packed protein suspension within each cell. As demonstrated in Chapters 2–3 the intensity of light scattering is linked to both the size and refractive index of the particles in question. Relatively large cells representing regions with a high concentration of refractive protein will cause a more intense scattering than a lysed sample (disperse dilute protein suspension). An additional factor is that of hypochromism which in this case is caused by the extreme proximity between the *heme* groups (the protein chromophores) between each protein within each cell, causing a corresponding reduction in the absorbance measured[66].

4.4.3.2 Preliminary LD spectra

It was hypothesized that the LD spectrum produced by red blood cells would demonstrate a spectrum that consisted of peaks in the ~240–300 nm range corresponding to the membrane-related aromatic amino acids, and small quantities of membrane-bound hemoglobin (at least compared to the bulk cytosol). Preliminary studies collecting red blood cell LD spectra proved not only to be different from the hypothesised outcome, but also to be extremely variable regarding transition sign and intensity. Even when examining repeat preparations made to 'identical' concentrations (measuring in 'packed cell volume', PCV, the volume ratio of cells to buffer solution) demonstrated high variability in peak intensity (as well as peak transition sign in some cases). Improvements to both sample preparation and data collection protocols proved to substantially decrease this variability resulting in the reliable negative transition spectrum shown in Fig 4.17. Regarding data collection, care was taken to ensure the position of samples within the instrument and shear-flow duration/speed was kept identical between samples. Optimising sample preparation was conducted by the preparation of concentrated cell suspensions to draw from instead of preparing

samples directly from the blood cell pellet stocks to reduce cell adhesion to the measurement apparatus (allowing a more accurate determination for cell concentration).

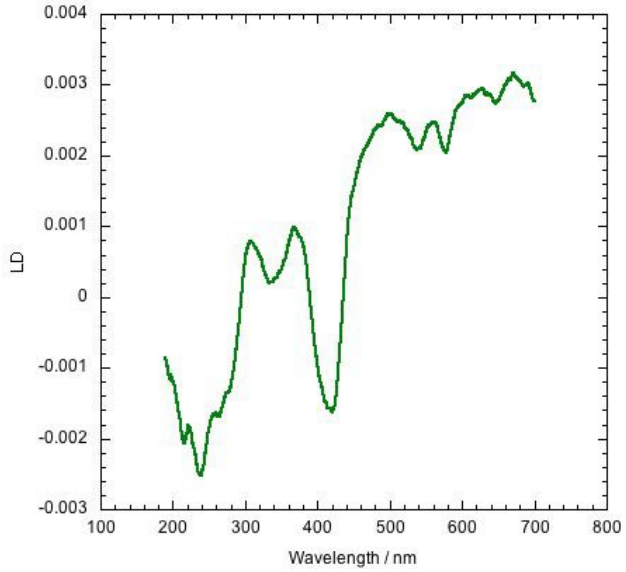

Figure 4.17: Shear-flow difference LD spectrum collected from an erythrocyte cell preparation in PBS buffer. [conc 3% PCV, pathlength = 0.5mm, position 29cm]

As shown in Figure 4.17 peaks present within the RBC LD spectrum match those of the oxyhemoglobin absorbance spectrum with entirely negative transition sign, (with the B and Q bands demonstrating the highest peak definition, corresponding to the $\pi - \pi^*$ electronic transitions). In addition, the intensity of the hemoglobin peaks is such that little else can be ascertained regarding the spectral contribution from any components other than hemoglobin. There is also a distinct negatively trending baseline as wavelength decreases, which again is likely due to the influence of light scattering from the cells in suspension. A more in-depth analysis was then taken into the source of this negative transition sign, regarding the individual flow state spectra. RBC samples were examined, and LD recorded, either in a flow-off state, or immediately after the initiation of shear flow.

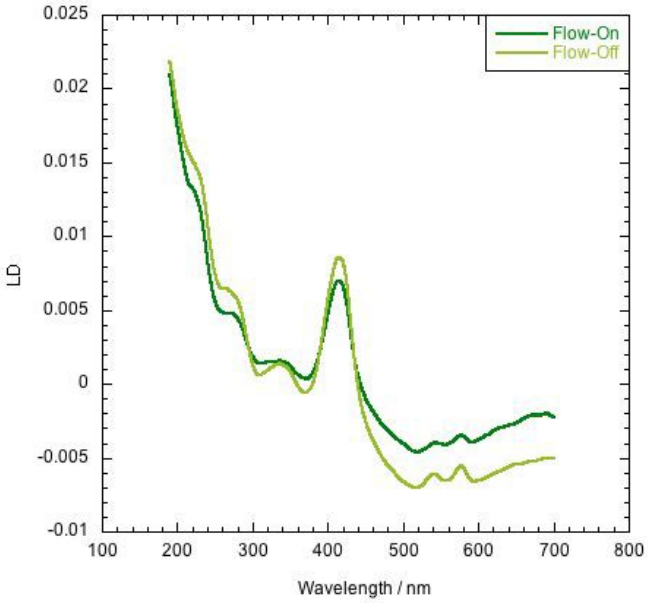

Figure 4.18: Representative flow state LD spectrum from an erythrocyte cell preparation in PBS buffer. [conc 3% PCV, pathlength = 0.5mm]

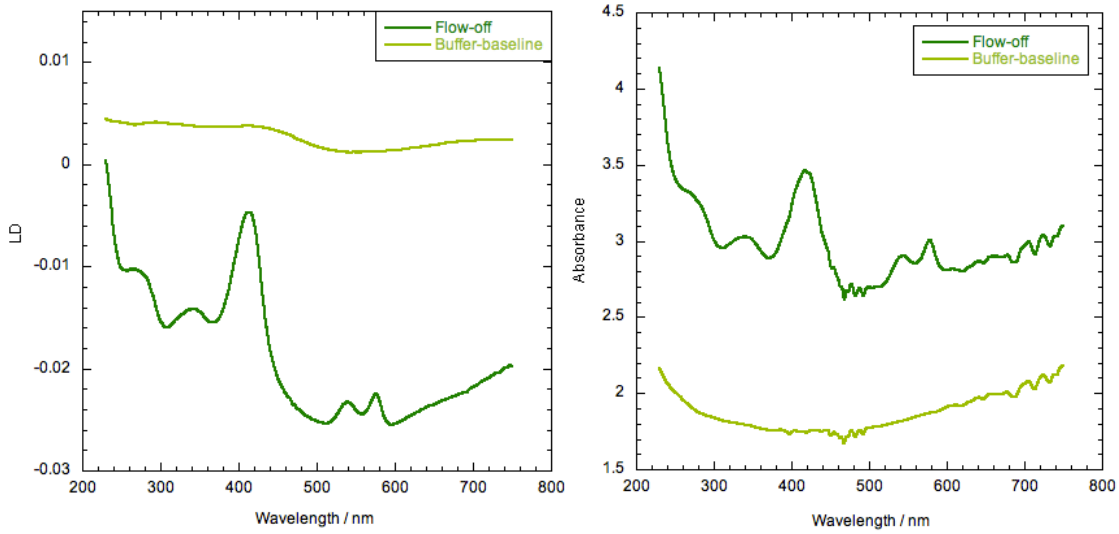

Figure 4.19: Flow-off state LD (*left*) and absorbance (*right*) spectra from an erythrocyte cell preparation in PBS buffer. [conc. 3% PCV, pathlength = 1mm]

If we consider the individual flow-off spectrum contrasted to a buffer baseline another feature can be observed, Fig. 4.19. The entire spectrum has been downshifted in intensity heavily in contrast to the buffer, which is close to zero (as expected due to the lack of any chromophores absorbing in this wavelength range). Since there are no

intense absorbance peaks in the ~600–750 nm wavelength range for hemoglobin this cannot be attributed to the LD component of the spectrum. In the absence of stray light, and the experimental setup is designed to minimize this, this deviation from the buffer-baseline LD is produced from the scattered light produced from the incident light striking the sample. In addition if we contrast the LD to the corresponding absorbance spectra, in addition to the overall reduction in intensity, there is a distinct change in the baseline shape of the flow-off LD not observable in the buffer spectra. This can be most easily observed again in the ~600–750 nm region where there is a steep incline not present not present in the base-line buffer LD spectrum and no absorbance.

The usual result observed when dealing with LD is that of a distinct spectrum observed in the flow-on sample, and a spectrum that closely resembles the buffer baseline absorbance in the flow-off sample[54]. This is not surprising since any LD signal requires alignment, and usually in the absence of flow induction samples randomly orient within solution. Since random rotation has no preferred alignment, this leads to the baseline spectrum shown in the flow-off sample, Fig 4.19. However as shown in Fig. 4.18, not only is there a distinct spectrum observed in the flow-off sample, it both shares a peak pattern with flow-on samples and is of greater intensity. Additionally both flow state spectra demonstrate exclusively peaks of the positive transition. This is indicative that there exists another mechanism present that is responsible for the induction of orientation within the sample to replace that of shear-flow (aka mechanically driven, pressure, sedimentary etc.). The negative LD spectrum observed initially is only produced as a result of difference calculation and as such this spectrum is not indicative of the chromophore alignment. Due to this, the main spectra of interest are those of the individual flow-on/off states, and not the difference LD spectrum.

4.4.4 Fission Yeast Cells

The last system to be analysed is the most complex in terms of both absorbing components and structure, and the closest comparison to that of a standard eukaryotic cell. Fission yeast (*Schizosaccharomyces pombe*) is a species of yeast that is

commonly used in biological studies since it acts as a unicellular eukaryotic 'model' organism[66]. It contains the typical organelles found in the majority of eukaryotic cells (such as mitochondria and the nucleus), in addition to extensive plasma membrane and cell wall structures. The geometry of the cells is also strongly uniaxial in nature, due to their rod-like structure, which is ideal for LD with regards toward flow alignment.

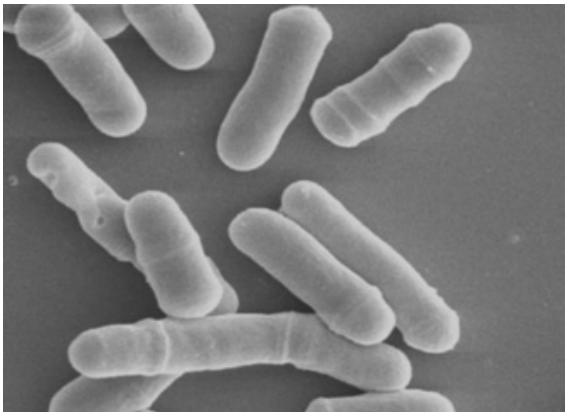

Figure 4.20: Microscopic view from a fission yeast culture from the literature[79].

Regarding aligned chromophores within the cells, it is unlikely that most of the organelles contribute toward the resultant LD spectrum. Unless these internal structures are membrane/cytoskeleton anchored they will orient randomly within the cells cytosol (aqueous contents within a cell). Since regardless of flow alignment each cell will have a random distribution and orientation of these 'free-floating' organelles they are unlikely to give rise to any noticeable LD signal. Therefore the chromophores that contribute to the LD spectrum are going to be chromophores linked to either the cell membrane or wall. These components are expected to primarily consist of aromatic amino acids comprising the cytoskeleton of the cell and chitin, a fibrous polymer (glucose derivative), which is one of the primary elements that form cell walls in fungi[76].

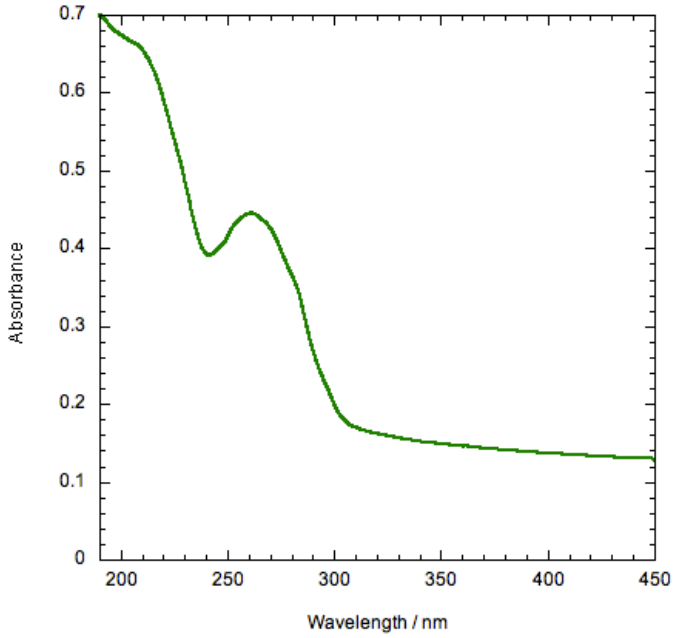

Figure 4.21: Absorbance spectra from a fission yeast sample suspended in purified water, (conc. 5% PCV, pathlength 0.5mm).

As we can see from Fig. 4.21, each of the elements expected are observable in the spectrum measured. There is an overlapping cluster of peaks present in the ~240–300 nm range corresponding to chromophores within the cell including the various aromatic amino acid peaks and DNA. Additionally there is a noticeable hump at ~210 nm which can be attributed to the chitin component of the cell wall as well as well as protein amide bonds and DNA bases. Unfortunately due to the influence of light scattering and the relatively low absorbance intensity of the samples it was not possible to scan further into the far-UV wavelength range (e.g. to examine protein secondary structure elements).

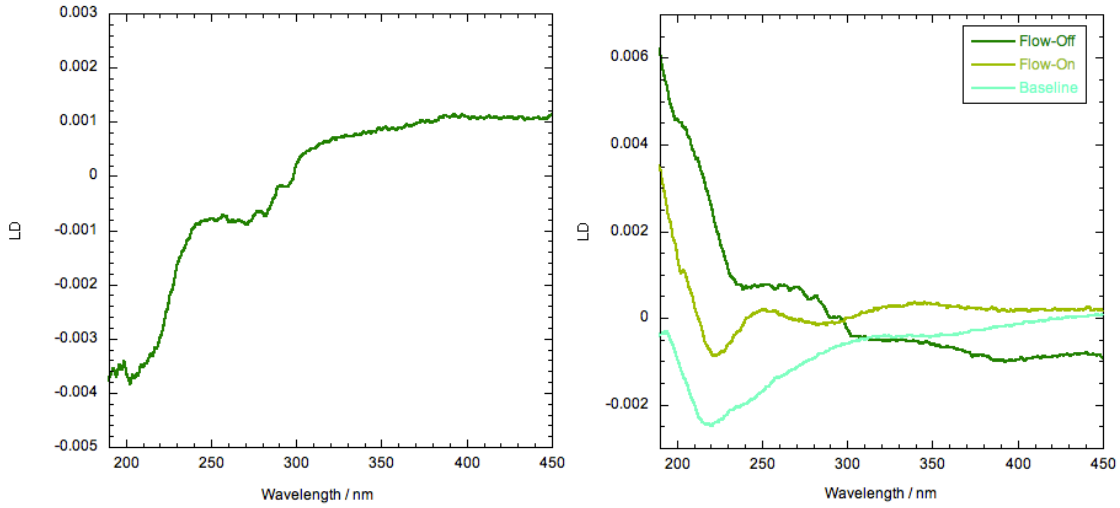

Figure 4.22: LD spectra from a fission yeast sample suspended in purified water, (conc. 5% packed cell volume, pathlength 0.5mm). *Left*: Flow on/off difference spectrum. *Right:* Individual base-lined flow on/off spectra.

Of the observed elements in the absorbance spectrum, the peaks at the ~240-300 nm range in the corresponding LD are far more defined now and can be much more easily attributed to the various contributions from aromatic amino acids. Similarly there appears to be indication of chitin alignment due to the vague peaks occurring at ~210 nm although to a much lesser degree. This could be due to a relatively weak chromophore absorbance of chitin or the extent of its orientation. An interesting additional feature can also be observed regarding the transition signs of the spectrum in conjunction with the individual flow-state spectra. There appears to be a substantially more intense LD absorbance when considering samples in the absence of flow. Although this is a system of much greater complexity, a trend can also be observed in which flow-off spectra produce a more intense LD (similar to that of red blood cells, Fig 4.18). In the absence of shear-flow induced cell orientation, another mechanism must logically be in its place to produce the flow-off spectra observed. The fact that this behaviour is being observed in both simple (RBC) and complex cellular systems (fission yeast), and yet is not present in smaller systems (M13 and DNA) warrants further investigation since attempts to determine the precise extent of component orientation when the source of impetus, and the extent of orientation in flow-off conditions, is under debate would be imprecise at best.

4.5 Conclusions

In summary, the main aims of the work reported in this chapter were to take a given spectrum, be it cellular or smaller (i.e. DNA) and understand how it is produced in terms of its component chromophore spectra. A process was applied in which any given component spectrum could be emulated in terms of Gaussian curve (the optimal amount and preliminary values for fitting determined via an approach known as space-scale filtering). Systems in terms of increasing complexity, and number of components were examined from DNA to M13 bacteriophage to the cellular systems of RBCs and finally fission yeast. Further features regarding the component interactions within each system were also examined such as the hypochromicity of hemoglobin. Lastly when considering the RBC and yeast cellular spectra, further features were observed regarding the orientation of components under flow-off conditions that warrant further investigation.

Ideally the approach taken in this work with regards to the Gaussian decomposition of component and system spectra would be sufficient to analyse any given system spectrum and return information about the oriented components within that system. Although intensity matching of the component Gaussians has proven to be difficult, the contrasting of peak wavelength and shape has been shown, in works with DNA and M13 phage, to be a viable approach to indicate the component transitions of an LD spectrum. The contribution of each predetermined component can be clearly outlined within the system spectrum. However, when dealing with larger and more complex cellular systems, demonstrated by RBCs and fission yeast, there appear to be further concerns that need to be addressed. Most notable among these is the positive transition spectra produced from the flow-off LD recorded from equine red blood cells. At this stage, without further investigation into the origination of these changes, the definition of what precisely constitutes a model cellular LD system spectrum, particular regarding the unusual behaviour of RBCs, is still debatable. To facilitate this, a detailed investigation into the RBC LD spectra was undertaken, (due to its simpler structure and apparent single component as opposed to that of fission yeast) and the role of scattering in LD spectroscopy of large systems was explored.

Chapter 5: Erythrocyte LD dynamics

5.1 Overview

As discussed in Chapter 4, LD spectra are usually presented as difference spectra between flow on and off states. Therefore since alignment should only occur in the flow-on state the resultant spectrum is essentially a baseline subtracted flow-on spectrum. Also as demonstrated this is not the case for red blood cells, in which the flow-off sample exhibits a distinct spectrum of purely positive transition sign peaks. To produce such a spectrum there needs to be elements of internal hemoglobin orientation present within the sample that in turn means that the cells must be oriented.

5.1.1 Protein orientation

The first matter to be considered regarding protein orientation is the inherent intensity of the hemoglobin absorbance demonstrated in both flow state spectra. Regarding hemoglobin concentration within a given volume of blood cells (the mean corpuscular hemoglobin concentration, MCHC), literature sources state values of ~20 mM[80]. The concentration commonly used in this work, 3% PCV, equates to an average hemoglobin concentration of 600 μM enabling us to obtain maximal absorbance intensity whilst remaining within limits of detection of the photomultiplier tube. In contrast, samples used in the aromatic amino acid studies in this work reach a similar absorbance threshold with samples of only ~100 μM (dependent on the amino acid in question). However, if we were to consider the quantity of membrane related proteins and the corresponding quantity of aromatic amino acids this ratio no longer becomes comparable. The most prevalent of these is the anion transporter protein Band 3, taking up a ~25% of the membranes interior surface[70]. Band 3 is comprised of ~900 amino acids (dependent on the species of RBC) ~14% of which are aromatic amino acids all of which contribute to an LD spectrum. Literature sources have reported the apparent binding of hemoglobin to these proteins[73], but even with the assumption that

for every copy of Band 3 there is an equivalently bound hemoglobin, the resultant LD should be demonstrating at least signals of similar intensity from both aromatic amino acid and heme group sources. However we observe only the hemoglobin peak pattern, even at the 250–280 nm wavelength region where aromatic amino acids absorb (far-UV, N and M bands as shown in Chapter 4). This is unexpected since it was initially postulated that the primary contributions expected to appear in the RBC LD would be from these aromatic amino acids, and yet hemoglobin absorbs a sufficiently high intensity that these are hidden. In order for this hemoglobin signal to dominate the LD, it cannot be produced by purely those in close proximity or bound to the membrane. Instead the bulk hemoglobin content within the cytosol of the red blood cell must be contributing towards the LD spectrum.

In order to analyse the source of impetus for this hemoglobin dominated LD signal we must first understand how oriented hemoglobin produces an LD signal. When considering the signal produced by oriented hemoglobin, it is more precise to consider the chromophores within the protein that are giving rise to the absorbance peak. It is not particularly uncommon for proteins to contain multiple copies of the same chromophore, however, proteins from the globin family have the unusual trait where they contain multiple copies of the *heme* porphyrin (one in each of four sub-units) that are in different orientations[65]. Within hemoglobin in particular there exist four *heme* groups in two general orientations (motion and flexibility in protein quaternary structure render each pair approximately equal, but not exactly). Although this has no particular effect on the absorbance spectra (other than the increase in intensity proportional to the amount of chromophores), the resultant LD presented by a single protein should always be considered to be a cumulative overlay of the LD contribution from each individual *heme* group, (Fig 5.1).

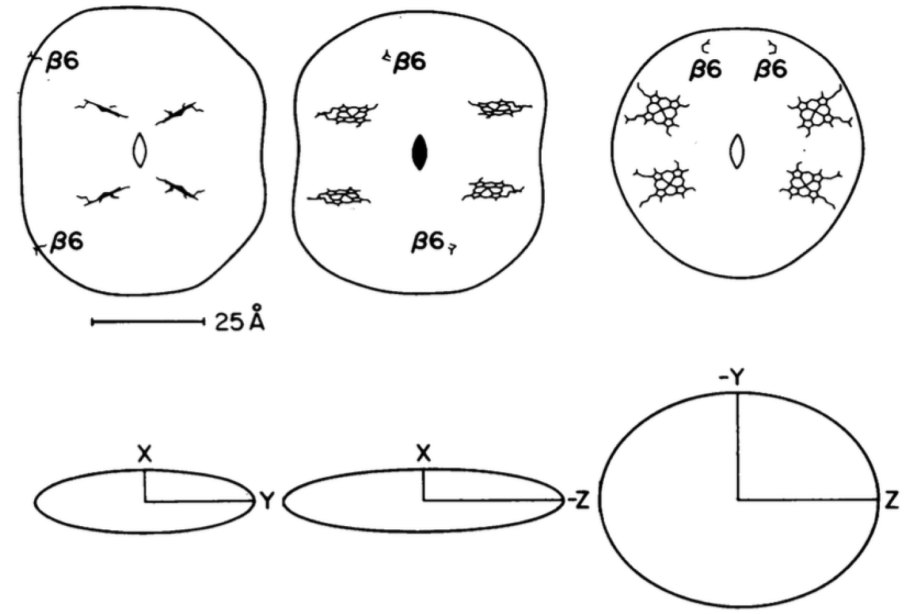

Figure 5.1: Literature illustration of the angular states of the planar heme group within deoxyhemoglobin; projection of the proteins molecular surface (*Top*) and optical absorption ellipsoid (*Bottom*). Central 2-fold molecular axes are shown to demonstrate the various angular positions of the collective heme planes in contrast to the natural axis of the beta 6 residues. The views are drawn from computer plots of a stick model using atomic coordinates of horse deoxyhemoglobin, whose structure is very similar to that of human deoxyhemoglobin A[65].

Normally it would be both unlikely and unreasonable to expect such an intense LD signal from a protein solution, be it derived from membrane-bound or bulk cytosol proteins, since high levels of orientations are more likely to result as when considering fixed structures like crystals. However, due to the combined signal source from the four hemes it permits a higher variation in protein position and relative orientations, since as long as there is a prevailing orientation of the *heme* groups, regardless of the actual protein orientation, an LD signal can be detected. Essentially the angular orientation values for each heme can differ between proteins of slightly different orientation and position (e.g. relaxation and motion) as long as the *average* heme orientation remains the same.

When considering the flexibility available to proteins in general within a fluid living system (instead of a fixed crystal structure), particularly regarding the relative positioning of quarternary structures within a protein such as globin sub-units, there

exist a significant potential range of motion for the *heme* planes. Provided that a predominant average heme orientation is maintained between each protein, this extra flexibility in each proteins relative orientation allows for the possibility of a less rigid structure to produce the observed LD signal. If that is indeed the case what would be observed would be less like an fixed ordered protein crystal (unrealistic to expect to form within healthy cells), but instead a more fluid quazi-crystal type formation within the cell. There cannot be a fixed state crystal formation, hence the terminology 'quazi-crystal' since such a structure at such a high concentration inside the cell would cause negative health issues (characterised in patients with the mutant form of hemoglobin, HbC)[ref]. In previous literature it has been a topic of much speculation whether hemoglobin exists in this type of ordered liquid-crystalline state over a state of random rotation. Most notably are works by M. Perutz (Noble Prize winner for founding research into hemo/myo-globin) in which x-ray scattering studies suggested that the arrangement of hemoglobin in cells is intermediate between the order of a solid and the disorder of a dilute solution although definitive proof was not obtainable (most likely due to the technological constraints of the time)[82]. In support of this are also extensive works conducted in the electron-microscopic examination of sickle-hemoglobin gels (formed by the polymerisation of hemoglobin into long chains due to mutations in the protein structure) by Deaver et al., which were observed to be similar to that of nematic-phase crystal structures[102].

Lastly investigation of the internal protein organisation within red blood cells is a matter of considerable difficulty. Although it is simple to introduce a variety of conditions that can influence the behaviour of the hemoglobin rich cytosol, exclusively investigating the potential presence of interactions between proteins is extremely difficult if the cell integrity is to be maintained in its healthy state. In addition, conditions that influence the behaviour of either the membrane or membrane related structures (e.g. how pH changes can be linked to stomato/echino-cytosis of red blood cells[83]), could lead to the altering the geometry of the cell and consequently the extent of cellular orientation. To compound this, when considering protocols, concentrations must be carefully considered since alterations to the osmotic strength of the buffer can also alter cellular geometry[84]. Since any changes to the cell geometry have the knock-

on effect of influencing *cellular* orientation, this makes it difficult to isolate whether any changes to the LD peak intensity is occurring specifically changes occurring from the extent of *protein* orientation.

5.1.2 Cellular orientation

During LD measurement, spectra are usually recorded shortly following the initiation of shear flow since when dealing with small uniaxial particles (e.g. DNA) it is not required to maintain a high rate of flow for long periods of time in order to achieve optimal levels of orientation. In fact prolonged periods of rapid flow can often be detrimental due to damage being inflicted by the shear stresses[85]. However, when dealing with the flexible and robust red blood cells this is no longer an issue. In fact when dealing with large particles on the scale of microns with a relatively low axis ratio (relative to long fibrous particles such as tubulin), in order to obtain equivalent proportions of oriented particles it takes a proportionally longer time under the same shear rates. Since the influence of the shear flow on red blood cells should be relatively low over a short period of time taken to record a typical LD spectrum, any disruptions to the cellular orientation in the flow-off state would be of minimal impact. Extending the duration of the flow however should help ascertain the interaction of the flow-induced orientation with the flow-off pre-existing cellular orientation. In fact the usual assumption with regards to LD is that in the absence of flow the sample does not exhibit any significant degree of orientation, at least in contrast to flow-on samples. Studies in red blood cell interactions have observed their capacity to form ordered macrostructures. An example of this is *rouleaux*, a cylindrical face-on stacking of aggregated cells similar in geometry to a stack of coins[86,103]. Although it is unlikely to be seen in this work, since it is usually driven by fibrin binding between cells (samples in this work are defibrinated to prevent clotting), however, it serves as proof of principle for the types of behaviour that these cells can exhibit. However, if we consider the LD produced from RBC samples in the absence of flow, there is a well-defined LD spectrum consisting of the hemoglobin peak pattern of greater intensity than the flow on samples (Fig. 4.18). In order for these 'flow-off' samples to produce a LD signal of this relative intensity those cells must be exhibiting a sufficiently high

degree of orientation such that it outweighs the orientation produced within this flow-induced samples.

Red blood cells have been examined previously in the literature in relation to their orientation dynamics in flow (primarily considering the fluid dynamics within blood vessels, Fig. 5.2)[103].

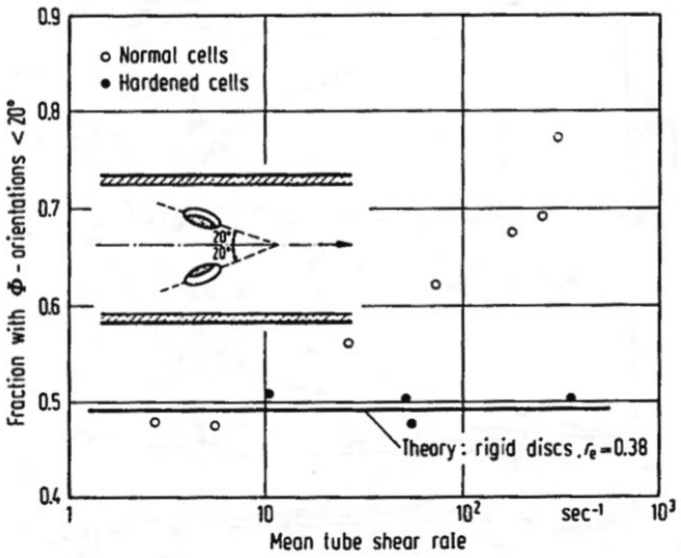

Figure 5.2: The flow orientation distribution of healthy red blood cells (hollow circles) and hardened cells (solid circles, hardened by treatment with glutaraldehyde) oriented such that the cellular long axis has an angle of < 20° with respect to the flow direction[103].

When subjected to shear rates in excess of 50 s^{-1}, even at extremely low concentrations (to minimize interactions between cells), RBC cell suspensions begin to orient such that the long axis (major axis) of the cell is orientated in the flow direction, in increasing quantities as flow rate increases (Fig. 5.2)[103]. As concentration increases and so inter-cell distance decreases this is further exacerbated, causing orientation of greater volumes of cells at correspondingly lower shear rates. It can also be seen in the same work that the extent of flow-orientation is heavily dependent on membrane fluidity, linking membrane stability to LD signal intensity. Shear rates induced in LD assays in this work (unless specified otherwise) are a close approximation of those found in blood vessels (dependent on vessel diameter and proximity to wall), at 3000 rpm[104]. Although higher shear rates would be preferable for the purposes of signal intensity and clarification, at rates higher than the aforementioned values erythrocytes

have been seen to distort and finally rupture[85]. Therefore, provided that the shear flow LD system used in this work matches the shear rates observed in the literature, similar levels of flow orientation should be occurring. In that case the orientation observed in our flow-off must be at least as prevalent, if not more so, to produce LD signals of competing intensity.

When considering how red blood cells can orient in this manner, they are not only much larger than the particle size normally examined in the literature regarding LD (by several orders of magnitude), but are also both highly dense (due to the high concentration of hemoglobin within each cell) and exhibit various morphologies dependent on their environment (e.g. the salt concentration, the tonicity, of the surrounding buffer, Fig. 5.3) [84].

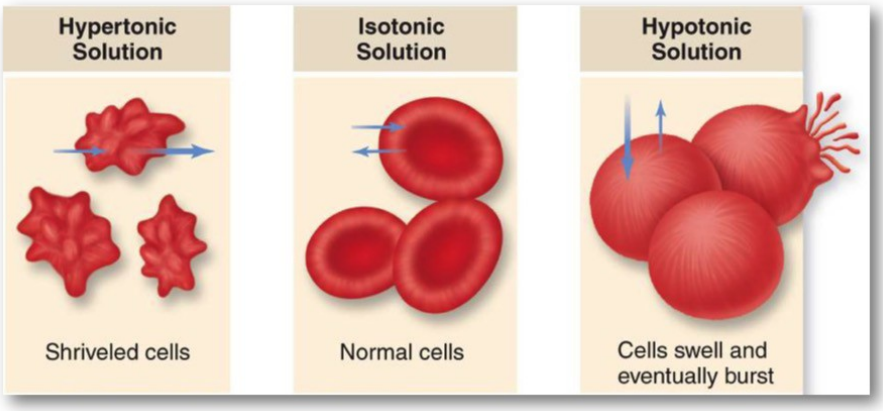

Figure 5.3: Graphical representation of the transition from a normal red blood cell to echinocyte (hypertonic) and stomatocyte geometries (hypotonic) based on the osmotic pressure of the buffer.

Red blood cells are sensitive to the surrounding environment in further ways that are not limited to purely the osmotic pressure however. Various other parameters such as the temperature, gravity, or even the physical container for the samples can all influence the cells be it by geometrical or behavioural changes (such as cell adhesion toward specific material surfaces or aggregation into macrostructures) to induce this orientation in flow-off samples[87]. The presence of a pre-existing orientation present in a dilute cell suspension, however, is not a topic that has been observed in existing literature. This is most likely due to the difficulty in observing large-scale orientation

throughout the suspension, particularly those in motion, as opposed to samples upon fixed slides (e.g. via microscopy). What is commonly assumed therefore in the literature is that large particulate suspensions such as cells exist in a state of random rotation when in the absence of any outside interference. Even in situations in which particles have a degree of inter-particle interaction sufficient to demonstrate aggregation, there appears to be no cause for an overall directional alignment to exist within these aggregates. Despite this, there clearly exist some influence from the surrounding environment, which is capable of inducing an overall cellular alignment.

If we consider a static prepared sample contained within a LD capillary cell, there are a limited number of forces present upon it, which fall into three main categories. Firstly the impetus provided by the sample preparation process that is still present during scanning. This has been noted previously in related LD works that after shear flow induction a significant degree of orientation is retained in some samples after flow has ceased[54]. This can generally be observed as weak but measurable spectrum in flow-off spectra taken directly after the shear motor is stopped. Secondly there is the physical environment that the sample is contained in, where the substance composing the sample vessel and its geometry could potentially be influencing the particle alignment. Of particular note are the details regarding the adhesion of cells on glass surfaces have been documented in the past[87], and if the quartz vessels used in most LD studies were to demonstrate the same or similar characteristics this could present a possible solution. Lastly there are the standard environmental effects present in the forms of temperature (via influencing membrane behaviour)[88] and sedimentary forces (selective for red blood cells due to their non-spherical nature) remain possibilities.

5.1.3 Light scattering

Standard practice when recording spectroscopic data is to place the sample in question as close to the detector apparatus as possible[54]. All samples can scatter light to some degree, although the majority of the scattered intensity occurs in the forward direction (towards the detector). If the sample is sufficiently close to the detector, however, then most of this scattered light, along with that not being absorbed, will enter the detector

and thus be treated as transmitted light (and so ignored by the software). Therefore although we technically measure the cumulative total scattering, the signal is generally going to be dominated by the scattering intensity that occurs at the smallest scattering angles for any given sample[89].

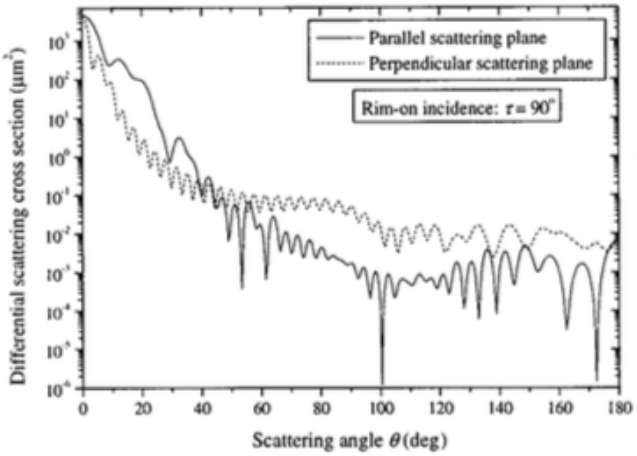

Figure 5.4: Evaluated differential scattering cross sections for rim-on He-Ne laser light illumination of a biconcave-disk-shaped RBC plotted versus the scattering angle θ [89].

In general, when dealing with particles within the RGD size range (as discussed in Chapters 2–3) the scattering intensity has a $1/\lambda^4$ wavelength dependence, which can be observed in the LD spectrum as exponential increase in baseline as wavelength decreases[32]. If we then consider the individual flow-off spectrum contrasted to a buffer baseline (Fig. 4.19), the shape of the negative baseline shift demonstrates features that are highly indicative of scattering. However, in order to deconvolute a given LD spectrum into component Gaussians, as demonstrated in the previous chapter, this scattering must first be addressed and removed either via calculation or by experimental protocol. Literature studies regarding scattering from a modeled RBC either parallel or perpendicular to the plane of the rim-on cell. As the angle decreases the intensity of the scattered light increases accordingly on a logarithmic scale.

Therefore in summary, in order to fully interpret the red blood cell LD spectrum the main areas to be addressed are as follows: to determine the underlying influences responsible for inducing cellular alignment in flow-off samples, the

alignment of hemoglobin present in the bulk RBC cytosol, and the LD specific scattering behaviour.

5.2 Methods

Unless specified otherwise red blood cell samples and pellets were prepared as previously stated in Section 4.1.1, with the addition that unless specified otherwise sample vessels were positioned at an 18 cm from the emitter prior to recording LD. Unless specified otherwise, flow-on/off samples were prepared at 3% PCV and the LD recorded immediately after the initiation of flow. Preparation of each buffer solution and other protocols are as stated for each assay:

Flow-on assays

Samples were taken from flow-on samples prior to flow, flow-on samples recorded immediately after flow begins, and flow-on samples only recorded after 10 minutes of flow. Samples were collected via an LD shear flow apparatus (as discussed before), distanced ~10cm from the detector aperture in 0.5mm cylindrical couette cell sample holders.

Flow-off assays

Microscopic imaging of flow-off samples was conducted via insertion of slides at 1% and 2% PCV into a Cellometer. Concentrations were assigned at below the standard concentration used in flow-assays in order to investigate potential inter-cell interactions, which is easier to observe in dilute cell suspensions. Sample preparation impetus assays were conducted by the removal of the end of the plastic tip attached to the measuring pipette (resulting in an ~0.5 cm aperture instead of ~0.1cm) when placing samples into the LD couette cell. The lack of a higher-pressure extrusion of the sample into the recording vessel should reduce any impetus this extrusion causes in contrast to a standard sample preparation. Physical environment impetus assays were first conducted by the preparation of standard samples in both LD couette and 1mm CD cuvette sample vessels. The samples were then drained from the vessels (micropipette with a long ultra-fine tip) and the LD spectra recorded. Secondly

alternative sample vessels of the same type were contrasted containing identical RBC preparations (e.g. 1 mm cuvette with a different 1mm cuvette). Standard conditions impetus assays were conducted firstly by incubating samples at 4 and 37ºC temperatures (via a water bath) for a 2-hour period prior to LD recording, in contrast to standard preparations at room temperature (~25ºC). To examine sedimentation, samples were placed in 1 mm cuvette sample vessels, at a distance of 29 cm from the emitter, and time-course assays were taken recording a full LD spectrum every 5 minutes over a total duration of 4 hours at 1.5% PCV.

Steric influences: Concentration and pathlength assays

For the concentration assay, samples were made up from 0.5% PCV to 2% in 0.5% intervals (via dilution with PBS buffer of a concentrated stock cell suspension) in 1 mm quartz cuvettes and baselined using pure buffer. For the latter assay, a demountable quartz cuvette was used at 0.2mm in pathlength and contrasted to one at 1mm in pathlength. Each sample used the same concentration sample (1.5%PCV)

Environmental influences: Ionic and oxygenation assays

Regarding the ionic assay, the solution for the cells was altered such the 155 mM (0.9%) NaCl solution was instead replaced by a sucrose solution of identical osmotic pressure[21]. The phosphate buffer salts however remain in order to maintain pH stability. In the oxygenation assay, in order to convert a standard sample from oxygenated to its deoxygenated state, the suspension had N_2 bubbled through it for a period of 10–15 minutes before immediate LD measurement[90,75].

LD scattering influence: Angular contribution assays

Standard samples were made up in a 1 cm cuvette at 0.15% PCV and placed in contact with the detector aperture of the equipment setup and the LD signal recorded. These samples were then moved towards the source along the path of the incident light in intervals of 1 cm, measuring the LD spectrum at each interval.

Figure 5.5: Apparatus used in the angular contribution assays to move samples in 1mm and 1cm pathlength quartz cuvettes along the incident light direction (left to right) between emitter and detector.

Altered morphologies: Basic and tonicity assays

The protocol adopted for the basic assay, was that the buffer was pH adjusted using NaOH (using a pH meter) to reach pH 10.51, in which the cell pellet was then resuspended at the 1.5% PCV and spectral data recorded. For the tonicity assay, the buffer was diluted with phosphate buffered purified water (at the same concentration as standard samples) to reach osmotic pressures between the ranges of 144 (hypotonic) and 577 mOsm (hypertonic), concentrations commonly used and as specified within ranges of minimal lysis, as stated in the literature[105,83,91].

Applications: Ageing and metabolic assays

For the ageing assay, samples were prepared at 1.5% PCV and LD measured daily for a period of three weeks and then contrasted. For the metabolic assays samples were incubated at either 4 or 37ºC (via either fridge or water bath) for a period of 24 h, contrasting against a standard sample incubated for only 2 h (just to equilibrate) at 4ºC. This assay was then repeated without the presence of the phosphate salt in the buffer for each of the samples.

5.3 Results: Flow Dynamics

5.3.1 RBC flow-on dynamics

A series of LD assays were conducted on identical RBC samples, where shear duration was the determining factor, being measured via interval scanning time-courses. Their function was to examine whether the reduction in intensity in contrast to the flow-off samples was a short-term temporary loss of orientation (as the shear motor is started and flow initiated), or a steady dependence over time.

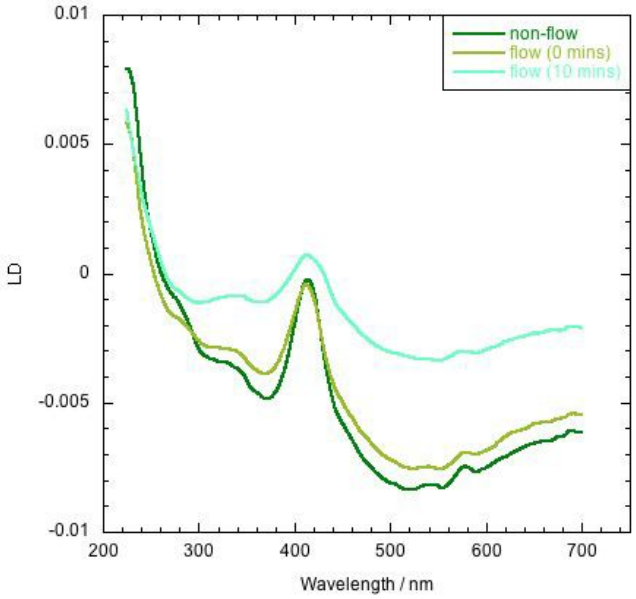

Figure 5.6: Representative LD variable duration assay [conc.: 3% PCV, pathlength = 0.5mm]

Repeat analysis demonstrated similar trends regarding peak size, although there existed variability in the relative peak intensity between flow and non-flow samples due to variability in the overall scattering baselines. What can therefore be observed from this assay, Fig. 5.6, is a clear relationship between both the hemoglobin peak size and underlying scattering baseline across the spectrum, and the duration of the shear flow. As the duration of flow increases the size of the hemoglobin peaks steadily reduce, and the scattering baseline approaches that of the surrounding buffer.

5.3.2 RBC flow-off dynamics

Since cell suspensions have the capacity to form aggregates or larger macrostructures in solution[92] (usually through membrane related protein binding, as is the case with RBCs and fibrin), a simple method to examine the behaviour of defibrinated cells in buffer is via microscopy of a standard RBC preparation, (Fig 5.7). For example, a visual inspection of the cell suspension should demonstrate aggregation or non-uniform cell dispersion if inter-cell interactions are occurring.

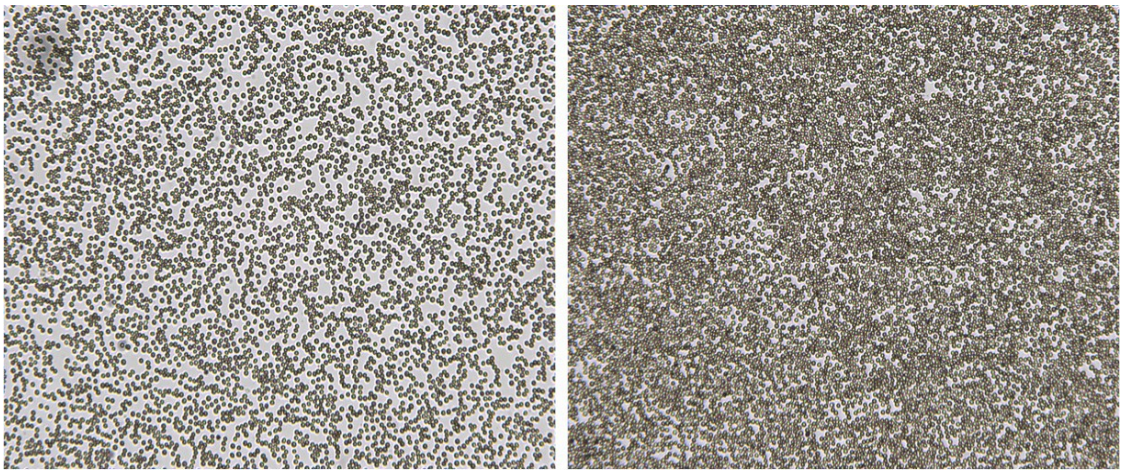

Figure 5.7: Microscopy images for RBCs. *Left* 1% PCV, *Right* 2% PCV. Scale automatically determined by the Auto M10 Cellometer for cells of 2-12um in size.

From the image of Figure 5.7, we can see that the cells are well resolved (with no jagged edges as would be seen if the cells were damaged or unhealthy) and randomly arranged. From a visual inspection there does not appear to be any significant deviation from a random dispersion of cells throughout the sample. This would indicate that here also appears to be no prevailing direction of cellular orientation and negligible elements of aggregation present in these samples. If inter-cell interactions were occurring, patterns in the cell dispersion would be present or clumping of cells into aggregates would be observable. This assay was also conducted at various concentrations (to investigate any potential influence of altered cell proximity), with lysed samples and pure serum as controls.

As a consequence the next step is to investigate the potential sources of orientation impetus that are present upon a static sample. These fall into the

aforementioned categories of sample preparation, physical environment and standard conditions. Regarding sample preparation assays, no alterations to the LD spectra were observed in any cases. In addition rapid shaking of the capillary before analysis (which should remove any inducing alignment caused by the insertion of samples) likewise rendered no change to the resultant LD spectrum in comparison to a standard flow-off spectrum, as observed in Fig. 4.19. Next, when examining the effect of the physical environment the resulting spectra from the drained samples demonstrated no noticeable change from the baseline. In addition no signal loss occurred in any of the alternative sample vessels was used. Lastly in the assays concerning investigation of standard conditions regarding the temperature assays, samples were tested between temperatures of 4 and 37ºC (to remain within the limits of RBC stability) in contrast to room temperature (~25ºC). Again negligible changes to the LD peak intensities were observed between each case.

To determine the effect of sedimentation, samples were scanned for extended periods (up to 4 hours) at 3-minute intervals. In the short time (<10 minutes) frame there was no noticeable change to the LD spectra observed, however, when considered for longer durations (>30 minutes) in some cases a slow progressive increase in LD intensity was observed, Fig. 5.8. It should however be noted that this was not reliable, even under identical setups regarding concentration (with minimal age difference), some of the repeat assays demonstrated no change over the full time-course. This would appear to be indicative of the sedimentary effects being present in the system capable of influencing the resultant LD. There is also a distinct change in the intensity of peaks present in these flow samples in contrast to those shown in previous flow-off samples, such as Fig 4.19. This can be attributed to the position of the sample within the instrument relating to collection of scattered light as detailed later on, Fig 5.14.

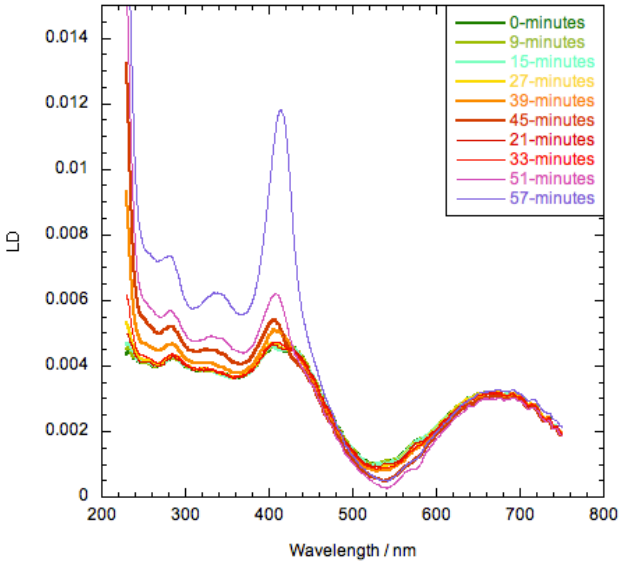

Figure 5.8: Time-course flow-off LD spectra taken at 3-minute intervals over the course of an hour. [conc. 1.5% PCV, pathlength 1mm, position 29cm].

5.3.3 Steric influences: Concentration and pathlength assays

Although rouleaux stacks are unlikely to be found within our samples (as discussed before), the potential influence of inter-cell interactions, however, is a serious concern for LD analysis. Ideally using extreme dilution for all samples would eliminate this, however this is unfeasible in order to gather spectra of sufficient intensity. An experimental assay therefore to examine the extent to which this occurs within the cell suspensions was conducted via investigation of the influence of concentration (e.g cell packing) on the intensity of the LD spectrum.

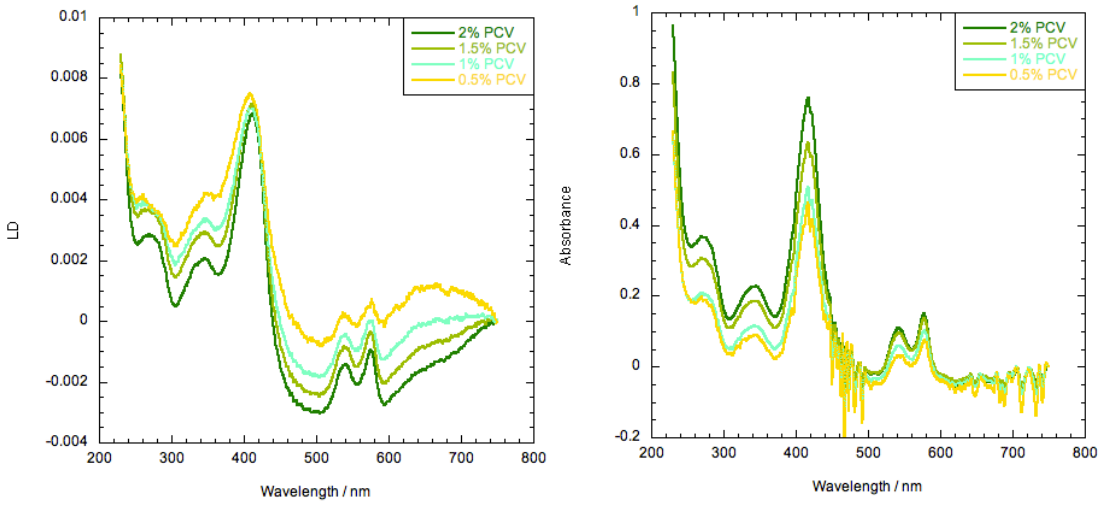

Figure 5.9: LD flow-off (Left) and Absorbance (Right) spectra from serially diluted RBC suspensions in PBS to four concentrations; LD data has been concentration corrected and zeroed to a non-absorbing wavelength (750 nm) to contrast peak intensities. [pathlength: 1mm]

Due to the variable influence of scattering for each cell density (aka more cells results in a greater scattering influence), demonstrated in Fig 4.19, in order to better analyse trends within the data, samples were zeroed at 750 nm, where no absorbance occurs for RBCs. To eliminate the effect of the increased concentration of hemoglobin upon the data (since we are interested specifically in the change in absorbance from cell packing and inter-cell interactions), the data was concentration corrected according to the Beer-Lambert Law. By altering the concentration the density of the cell packing within the sample would consequently increase. As the distance between the cells decrease, any physical interactions between cells that exist would become more and more prevalent (since it would be increasingly easier for each cell to reach the others). If these physical interactions were to occur to a noticeable extent, what would result is an alteration in the behaviour and/or position of each cell in suspension. Consequently the extent of orientation would also be altered, which would be then represented in this assay as a negative relationship between concentration and peak size, Fig. 5.9. It would appear that there seems to be minimal negative dependence of LD peak size with respect to concentration, with the exception of the lowest concentration samples (which are on the limit of machine detection). However although the relative peak intensities can be observed to be higher it is difficult to directly contrast these intensities since this is masked by a scattering baseline shift that becomes more extreme as concentration increases (similar to those observed previously, Fig. 4.19). Examining the corresponding absorbance spectra it can be seen that there is also noticeable scattering influence present, increasing as concentration increases and as the cell-cell distance decreases.

An alternative approach that supports this concentration assay is one in which the pathlength of the sample vessel was altered. Human red blood cells generally have a long axis diameter on the order of size of 6–8 microns[89] and equine cells (as used in these studies) are slightly smaller in the range of ~6 microns on average[93]. When

constrained within sample vessels of pathlength of a similar order, theoretically the extent of cellular orientation in the direction of the incident light would be inhibited. Minimal change in the LD spectra was observed between the ranges of 1cm - 0.2mm pathlength, however upon reaching 0.1mm all LD signal was lost.

5.4 Results: Environmental influences

As mentioned above in our introduction, it is particularly difficult to exclusively influence the internal environment of the red blood cell without also causing a corresponding change to the cell's shape or behaviour (and therefore confusing analysis by changing both protein and cellular orientation). Of the limited methods available the first is to alter the ionic strength of the cytosol. Studies in the literature have examined the relationship of hemoglobin towards the membrane-integrated protein Band 3, and in particular the positive relationship of ionic strength with the dissociation constant between the proteins was observed[91]. Although it is unlikely for the membrane bound hemoglobin to be solely responsible for the LD flow-off spectrum observed (as discussed above regarding relative intensities in contrast to those of aromatic amino acids), it may serve as a source of impetus for orientation within the rest of the cytosol. By the replacement of the ionic saline solution with a non-ionic sucrose solution of the same osmotic strength this ionic influence should be apparent. The resultant data did indeed show a reduction in LD intensity. However. a side effect was an extreme increase in red blood cell aggregation, to the point of sedimentation out of suspension, making the assay inconclusive.

An alternative approach is to consider the hypothesis (previously postulated in literature in relation to a discussion on the possibility of the hemoglobin cytosol acting like a pseudo-liquid crystal) is that the internal organisation of hemoglobin is linked to favourable packing interactions regarding internal oxygen transfer (the primary function of hemoglobin)[81]. An assay was therefore conducted to contrast the LD between oxy and deoxygenated samples, Fig 5.10.

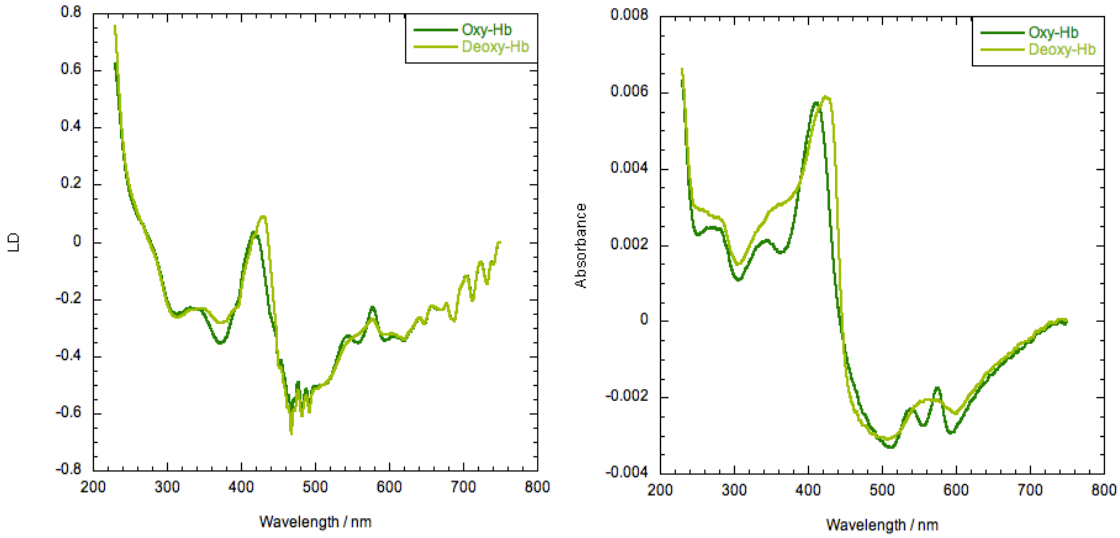

Figure 5.10: Flow-off LD spectra demonstrating the influence of hemoglobin oxygenation state for both LD (*left*) and Absorbance (*right*). [conc.: 1.5% PCV, pathlength = 0.5mm]. Data has been zeroed to a non-absorbing wavelength (750nm) to contrast peak intensities

When examining the resultant absorbance spectrum from the deoxygenated sample, as expected deoxygenated samples demonstrated slightly higher intensities primarily within the Soret region. Previous analysis in the literature regarding the polarised absorbance of oriented hemoglobin crystals have demonstrated slightly higher absorbance intensities for deoxyhemoglobin and, without a much more complex setup, a minor degree of evaporation was also expected[65]. When considering the accompanying LD spectrum it would appear as if there was only a minor loss in intensity in the deoxygenated samples. However, considering the elevated absorbance intensity deoxygenated samples displayed what should be observed if there was no significant LD dependence on oxygenation state was the corresponding increase in intensity in the Soret region. This minor loss of intensity should therefore be treated as if it was a greater loss than presented.

5.5 Results: Morphological dependence

To complement the assays conducted regarding the investigation of inter-cellular interactions, and the consequences regarding cellular orientation (concentration and pathlength assays), another method to examine the dynamics of cellular orientation is

to alter the geometries of the cells. As demonstrated in Fig. 5.3, the osmotic pressure of a given solution in general has a strong influence on the geometry of any cell without a structural wall (since cell walls are strong enough to resist deformation due to osmotic pressures to a much higher degree). Hypotonic saline solutions for example will have a corresponding decrease in pressure resulting in the cells distorting into a bloated ovoid/spherical shape (stomatocyte-like) with an increased intracellular volume, and vice versa for that of hypertonic solutions. This geometrical alteration directly influences the axis ratio and therefore the capacity for each cell to orient in a favoured direction (since spherical particles have no preferential orientation). However, alterations to the internal volume and concentration within the cell may also have significant affects with regards to the extent of protein orientation. The first assay was a tonicity assay, altering the salinity of the surrounding buffer to induce geometrical changes via internal volume loss/gain (Fig 5.11).

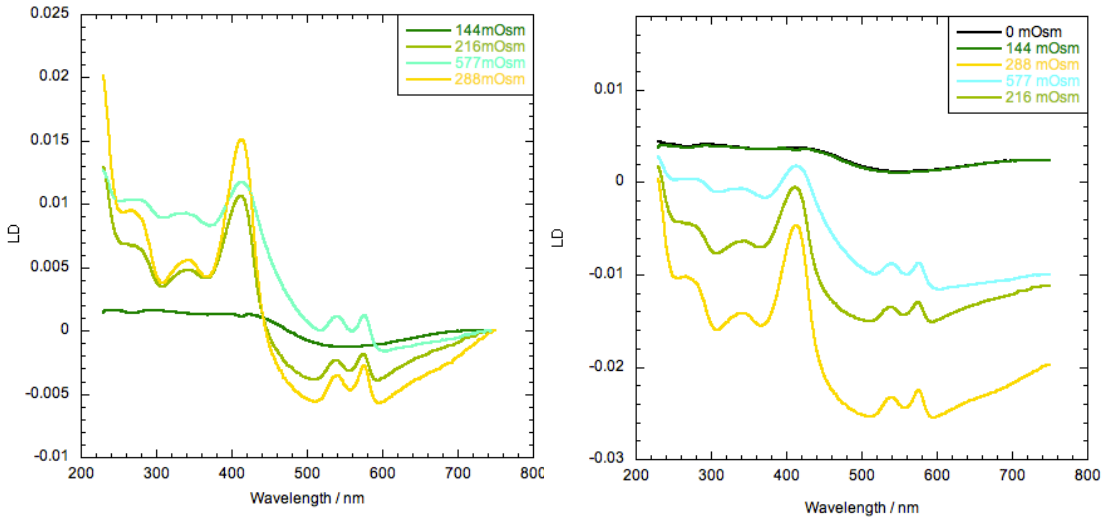

Figure 5.11: Flow-off RBC LD spectra in PBS for a range of buffer tonicity. Data has been shown as zeroed to a non-absorbing wavelength (750nm) (*left*), and raw data in contrast to the buffer baseline (*right*). [conc.: 1.5% PCV, pathlength: 1mm, position: 18cm from emitter].

In regards to the osmotic assay, under hypertonic (577 mOsm) conditions the peak size was reduced in contrast to standard isotonic samples (288 mOsm) trending towards the buffer baseline in addition to a reduction in the contribution from the negative scattering baseline (as can be more clearly seen from the raw data in Fig. 5.11).

Corresponding absorbance assays were also examined in order to verify that no lysis occurred in any of the above samples (since lysed samples demonstrate spikes in ~415 nm absorbance, Fig 4.16). When examining dilute hypotonic suspensions (216 mOsm) a similar reduction in peak size occurs, accompanied by strengthening the scattering influence upon the baseline. However when the osmotic strength is reduced further, transitioning from a bloated/cupped ovoid cellular geometry towards a more spherical one (144 mOsm), both the hemoglobin peak pattern and scattering contribution are eliminated.

To complement this, a second assay was conducted in which RBCs were exposed to pH basic conditions (pH 10.51), Fig 5.12. Literature studies regarding blood cells under these conditions have observed a similar geometrical type transition to that presented in hypotonic solutions[91]. This leads to the standard bi-concave shape to collapse towards a more spherical form, and as such the internal volume of the cell will remain constant, in contrast to the osmotic assay.

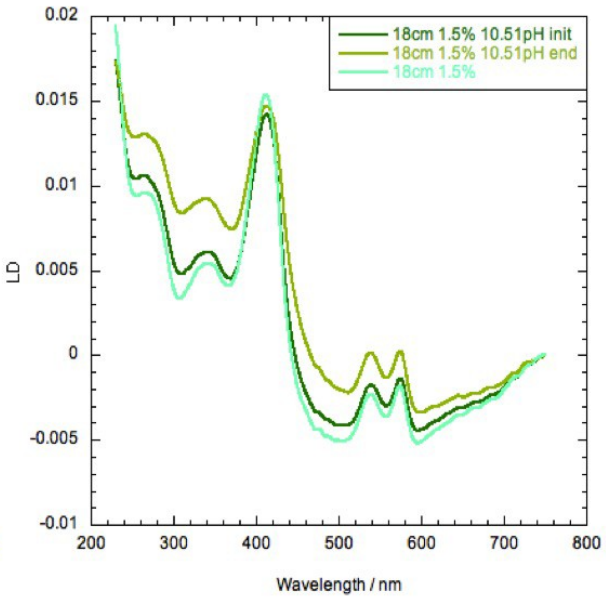

Figure 5.12: Flow-off RBC LD spectra in saline buffer under pH basic conditions in contrast to neutral standard conditions (pH 7). Data has been zeroed to a non-absorbing wavelength (750nm) to contrast peak intensities (*left*), and raw data in contrast to the buffer baseline (*right*). Samples were recorded both immediately after pH fixing ('init') and after 5 minutes of equilibration ('end'). [conc.: 1.5% PCV, pathlength: 1mm, position: 18cm from emitter].

The resultant LD demonstrated shows a noticeable reduction in the negative scattering contribution, similar to that seen in hyper/hypo tonic samples, in contrast to standard conditions. However there appears to be minimal change to the peak size across the spectrum, with the exception of a slight reduction of the 415nm Soret peak.

5.6 Results: Applications

Having established that the spectral characteristics of red blood cells samples are dependent upon changes to both interior and exterior environment, this opens up the field of research to a wider range of applications than simply a deeper understanding of the protein layout within the cell. The capacity to both detect and potentially quantify the extent to which the cellular geometry or internal structure may change dependent upon various circumstances should be of great use, particularly in the medical field. For example, every day hospitals are forced to dispose of vast quantities of donated blood that is past pre-determined storage duration. Commonly red blood cells have a lifespan of 120 days in circulation before exhibiting phenomena such as membrane vesiculation, volume loss and hemoglobin glycation, all of which should theoretically be visible under LD analysis[94]. A method for which to test blood as it is ageing to track these changes would validate their continued use would serve to reduce the wastage of viable bloodstocks. In an effort to explore this, assays were conducted to examine the ageing process of red blood cell stocks.. Although ideally examination would be conducted over a 120-day span to model this, both the lack of the materials to prepare optimal long-term storage solutions and time-constraints prevented this. It was postulated that over a 21 day period if this ageing process was measurable (before the final stages of breakdown nearing ~120 days) , then there would be an indication of a progressive trend. However despite daily measurement over the 3-week period, negligible variation and a lack of any notable trending of the data was observed in the resulting LD spectra.

Live blood cell preparations are also metabolically active and constantly respire, even in refrigeration, raising the concentration of carbonic acid within the surrounding buffer simultaneously influencing the pH of the solution[95]. Any

deterioration in the efficacy of this storage buffer (or potentially contamination) could lead to pH changes, which can be observed in the resultant LD (as shown in our pH basic assays Fig. 5.12). Assays were conducted in order to evaluate the relative stability of blood cell preparations since a method for which to analyse blood samples and detect variance from the healthy state should prove to be of use. By incubation of the RBCs at elevated temperatures (to increase the rate of metabolic activity) with and without the presence of phosphate buffering salts, the impact of this metabolic activity can be seen.

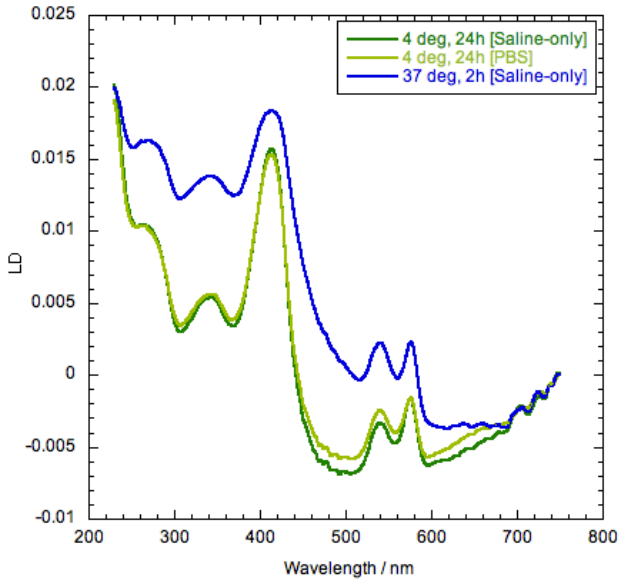

Figure 5.13: Phosphate salt-free buffer LD assay. Samples were incubated at either 4 or 37ºC for a 24h period and contrasted to a standard 4ºC sample allowed to equilibrate for a period of 2h. [conc.: 1.5% PCV, pathlength: 1mm, position: 18cm from emitter]

As demonstrated, Fig 5.13, there appears to be little to no difference to spectra collected from samples stored either in refrigeration or elevated temperatures when buffer salts are present in the solution. However in the absence of buffer salts there is a notable reduction in non-resonant across the spectrum after incubation at body temperature reminiscent to those demonstrated in the previous pH/osmotic assays. This change however was not observed in identical samples kept in refrigerated temperatures.

5.7 Results: LD scattering influence

In general, by positioning samples adjacent to the detector (as mentioned above in the introduction) the majority of any scattering influence on the spectral baseline is removed, leaving a spectrum purely considering the absorbance characteristics of a sample. However, by moving the sample back along the incident light direction this introduces a solid angle between where the incident light strikes the sample and the physical limits of detector, in which the scattered light is treated as if it had been absorbed. As the sample moves further away this solid angle shrinks and increasing amounts of scattered light miss the detector and are measured as 'absorbance'. Repeat assays at various solid angles allows the examination of the influence scattered light has upon the resultant LD spectra at various angular contributions.

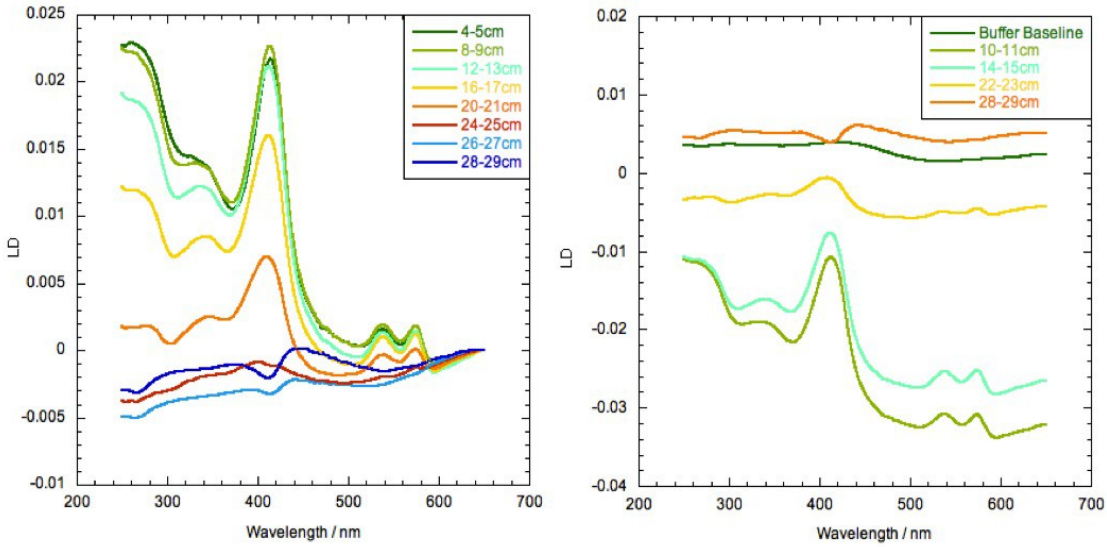

Figure 5.14: LD distance assay for zeroed (*left*) and non-zeroed (*right*) samples. Legend denotes the spacing distance between sample position and the light emitter aperture. (Left) Spectra were zeroed (at 700nm) after baseline solvent correction for clarity. Distance from emitter to detector apertures was 30cm in total. [Conc: 0.15% PCV, pathlength = 1cm]

As can be seen in Fig 5.14 (left), we can see that there appears to be a positive relationship between the quantity of scattered light intensity that is measured (increasing solid angle) and the peak intensity of the resultant LD spectrum. This appears to follow a clear and steady trend up to what appears to be a threshold at 8 cm

from the source where no further changes occur. In addition, as can be seen from Fig 5.14 (right), the underlying scattering baseline is of negative intensity, trending upwards towards baseline values as wavelength decreases. There can also be seen what appears to be a negative peak transition at 28–29 cm from the emitter, a distance at which minimal scattering is present since, as mentioned above in the introduction, the majority of scattering occurs at small solid angles and will therefore enter the detector. The resultant LD signal should then be dominated by pure absorbance, at the Soret peak (~415 nm) wavelength.

5.8 Discussion

During the course of this work it has become apparent that within the red blood cell there exist oriented structures, as opposed to the traditionally accepted chaotic random distribution of hemoglobin proteins within the cell. If we first address the matter of cellular orientation, the behaviour of blood cells in shear rates has been well documented in past literature. When subjected to shear rates in excess of 50 s^{-1} [103], even at high dilutions (to minimize particle interactions) cell suspensions begin to orient such that the long axis (major axis) of the cell is orientated with the flow direction, with increasing quantity of orienting cells as flow rate increases. As concentration increases and so inter-cell distance decreases this becomes exacerbated, at lower shear rates. Shear stresses induced in the LD assays conducted in this work are a close approximation of those found in human capillaries (500 s^{-1}), at 3000 rpm[104]. Regarding the flow-state assays, we postulate that the extent to which cells orient under these shear rates is lower than that present in a flow-off system even at 'optimal' levels of orientation (maximum possible alignment of the cellular long-axis with the direction of flow) due to the decreased intensity of peak absorption that occur under the flow-on state. If this was not the case, and the loss of peak intensity between flow-on and off states was simply caused by an initial disruption to the flow-off organisation, what we would observe instead would be an initial decay in LD peak intensity followed by a recovery trending back towards, and surpassing, the intensity demonstrated in flow-off spectra. Therefore instead of the usual difference taken for LD where the resultant data is the flow-on/off difference spectrum the more

appropriate approach in this case is to purely analyse the higher orientation flow-off system (using a PBS buffer for baseline difference). Since shear flow was only required to induce particle orientation, and that orientation is already present in static samples, only the flow-off spectra are required for LD analysis (although this necessitates the collection of solvent baselines to compensate for the lack of flow-difference baseline correction). This approach, although unusual for LD studies (in which alignment and therefore noticeable signals do not occur in flow-off spectra, hence the requirement for a flow-difference spectrum), permits analysis in alternative stationary vessels such as the quartz cuvettes as commonly used for either CD or absorbance sample collection in addition to the freedom to further adapt the experimental setup (due to not requiring a large couette flow system in place). Not only does this permit a closer degree of accuracy due to being able to use the same sample vessel for all types of spectroscopic studies but also allows more flexibility regarding further assays.

Next in regards to the flow-off spectrum analysis, there are a limited number of effects that can influence a non-flowing sample, and of those investigated almost all of them can be conclusively excluded from any potential particle orientation induction with the exception of sedimentation (Fig 5.8). It can be further deduced from the microscopy assay that it is unlikely that strongly uniaxial structures are present. It is not possible without specialised equipment to fully examine the influence of sedimentary forces over time, most notably the short time scale where red blood cells begin to orient (from an initial random orientation) since it is possible that particles optimally orient via sedimentary action in the 1–2 minutes it takes to record an LD spectrum. Further attempts were made to examine this short-time window closer by increasing scanning speeds with consequent reduction in spectral quality, and/or rapid reorientation of the sample (via tilting of the sample vessel relative to the incident light beam). Although the resultant LD peak intensities did demonstrate variability, it was not possible to observe a completely reliable trend. Ideally in order to establish a more extensive proof, a study would need to be undertaken examining peak wavelength intensities (since full spectra are too time consuming) directly observing the sample immediately after the cell pellet / buffer mixing process. Alternatively the sample

could be kept in constant random motion and observed after motion ceases. Since sedimentary forces are related to both particle shape and geometry it would logically follow that non-spherical particles, such as the biconcave discoid red blood cell will settle at varying rates dependent upon their orientation within solution. In addition, the tumbling rates, and subsequently the duration each particle spends in a particular orientation may well also be a factor, resulting in an overall favoured orientation within suspension. Literature studies regarding the falling dynamics of discs (similar in shape to the biconcave cells) would appear to support this concept[96].

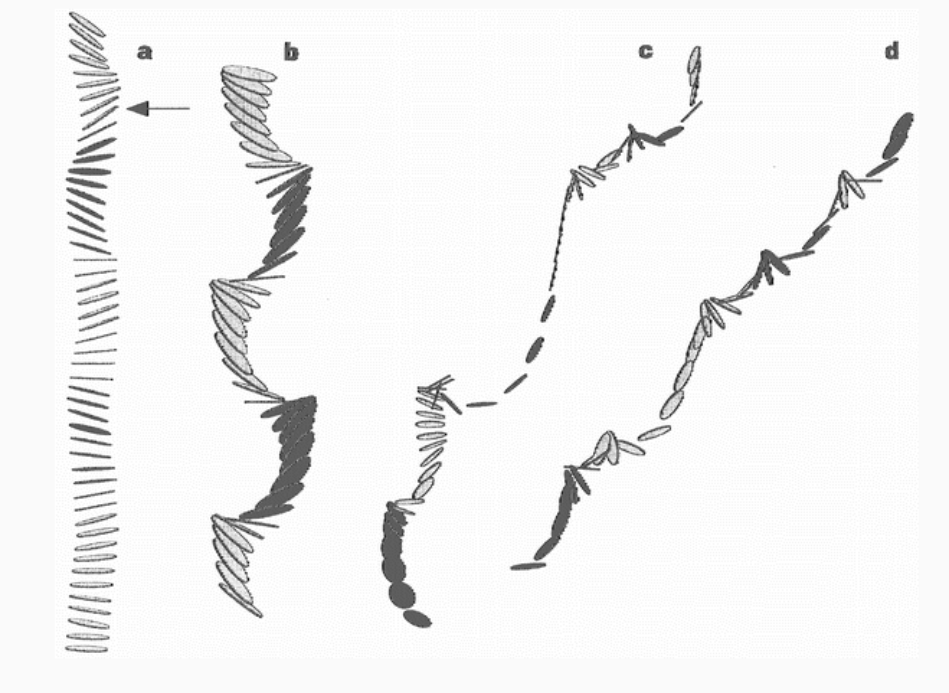

Figure 5.15: Illustration of the various falling dynamics demonstrated by discs depending on the Reynolds number and inertia of the falling disc; a) Steady-falling regime observed at lower Reynolds (Re) numbers, b) Periodic-oscillating motion observed at higher Re and low dimensionless moment of inertia (I), c) Chaotic motion found when both Re and I are moderately large. d) Tumbling motion found at very large inertia. [Figure reproduced from literature[96]].

The saline buffer solution used in these studies (PBS) should not be viscous enough (at least in contrast to the glycerol as used in literature studies) to correspond to a low Reynolds number (dimensionless quantity in fluid mechanics used to help predict flow patterns). However although dense, with no driving force other than gravity, red blood

cells should not possess a high inertia during sedimentation. The most suitable of the falling dynamics then according to literature (Fig. 5.15, b), is where a disk, dropped with any initial orientation, oscillates between horizontal and vertical states as it falls. The proportion of time in which the cell remains in each state then corresponds to the predominating orientation of the cell in suspension.

More recent works by Matsunaga *et al*[113], conducted after the work in this chapter was completed, made theoretical claims for the RBC alignment as a result of a boundary element modelling process. The result being such that the blood cell model predicted that the cellular long axis was positioned vertically with regards to the incident light (and perpendicular to the flow direction) as the cell fell through solution. To complement this, more experimentally driven works were conducted by Hoffman *et al*[114] investigating the behaviour of dilute red blood solutions under the influence of both sedimentation and centrifugation. They noticed that under standard gravity driven sedimentation cells did not appear to reorient themselves. Instead they were observed to slowly wobble with regards to their initial orientation, instead of tumbling (postulated to be due to shear stresses). It was only under centrifugation that cells began to reorient vertically (and distort into a 'bag-link' shape).

This would appear to indicate that the behaviour for red blood cell sedimentation without any impetus aside from standard gravity is for no significant prevailing orientation. However a notable feature of both of these sources (and of further references made in these works)[113,114] , is that they strictly deal with either sole red blood cells or solutions of extreme dilution. In order to obtain high intensity and quality LD the volume ratio of cells to suspension is of several orders of magnitude greater (1.5% PCV suspension equates to ~75,000 cells per ul). Due to this, the steric implications regarding the packing of cell layers could potentially influence the initial cellular orientation to cause the prevailing orientation that we have observed.

Regarding flow-on samples, since shear flow induces samples to orient their longest axis in the direction of flow (and considering the vertical cylindrical shear-flow system used in these studies), flow-alignment should induce cellular alignment edge on to the flow direction and predominantly face-on towards the incident light direction. Thus, any light that strikes the cell in the face-on orientation to the incident

light axis should return a null signal for LD (due to the symmetry of the disc around the incident light axis). In addition as the cells rotate around the flow axis, at the vertical edges of the Couette LD cell, they will present as edge-on but with the long axis oriented vertically. This equates to the opposite orientation as expected for flow-off samples (horizontal orientation with regards to the incident light), this provides an explanation for the reduction in LD peak size observed when comparing flow-on to flow-off samples.

Regarding analysis of the protein alignment within each cell, it is more appropriate to consider the implications of the light scattering assays first. The amount of light that a sample absorbs should have no relation to the sample distance from the detector; the only factor changing is the quantity and angular contribution of scattered light entering the detector. In essence was appears to be a the hemoglobin LD spectrum would instead appear to be being produced by the light scattering component resulting from the sample interacting with the incident light as opposed to its actual absorbance pattern. As far as typical RGD light scattering goes the intensity, although wavelength dependent to a certain degree, should not be capable of producing a hemoglobin peak pattern. When considering both formats of the data in Fig. 5.14, it becomes apparent that there are in fact two scattering behaviours occurring simultaneously. Firstly there is the typical smooth $1/\lambda^4$ curve (as mentioned above in the introduction) as expected from the signal being produced by hemoglobin proteins within the RGD size range, underlying the peaks of the spectrum (albeit negative in intensity). Then there is an unusual absorbance-mimicking peak pattern scattering layered on top of this. The latter of these two phenomena has been observed and detailed previously in other works, although the determining factors are still unknown, and has been characterised as *resonance scattering*[97]. Therefore contained in our spectra there appears to be an overlay of simultaneously non-resonant (typical RGD) and resonant scattering. Therefore in all of the observed assays, the strong intense hemoglobin LD peak pattern observed is not produced as a result of a difference in polarised absorbance; instead it is being produced by an unusual dynamic in scattering behaviour. In support of this premise, studies in the literature regarding the Resonance Raman spectra produced by red blood cells aligned ether horizontally or vertically

relative to the optical path have demonstrated large differences in intensity for various wavelength bands[98]. What has been observed was that edge-on cells exhibit more polarised bands whereas face-on cells produced more 'anonymously' polarised bands. This indicates that the orientation of the cell has a direct impact on the interaction with different polarisations of incident light. Of particular note is that Raman spectroscopy is specifically linked to light scattering (albeit in-elastic, not elastic resonance as we have observed) not absorbance, and yet still displays these trends. To compound this, from the same source, it was postulated that not only is it possible that hemoglobin forms liquid-crystalline structures within the cells, but also that the extent of alignment is linked to the transitioning from T to R (tense and relaxed) states of the protein as oxygen is bound[99]. Related works by Klug et al[106] have also confirmed that such oxygen gradients can act as a potential driving force on the diffusion/convection of hemoglobin within the cell.

Next, if we were to consider the samples in closest proximity to the detector (28–29 cm, Fig. 5.14) there is also a weak negative signal in the Soret wavelength region (~415 nm). Since scattering should be almost zero in this experiment and at this wavelength, this signal can only be being produced by the difference in polarised absorbance, i.e. a proper absorbance LD spectrum. We can therefore hypothesize that the average prevailing orientation of the heme groups contained within a flow-off sample cell suspension based on the negative transition sign displayed. The equipment setup dictates that in order to demonstrate a negative sign the absorbance transition of a given chromophore must be aligned in the vertical polarisation direction (perpendicular to that of the flow direction). In this case the average heme planar alignment must therefore be along this direction to produce the given LD signal (i.e. vertically aligned). Taken together with the cellular orientation that has already been determined, the resultant flow-off system is comprised of cells oriented horizontally and presented edge-on towards the incident light. Then within each one of those cells is an array of proteins in the bulk cytosol oriented such that on average the heme planes are oriented vertically and edge-on, Fig. 5.16.

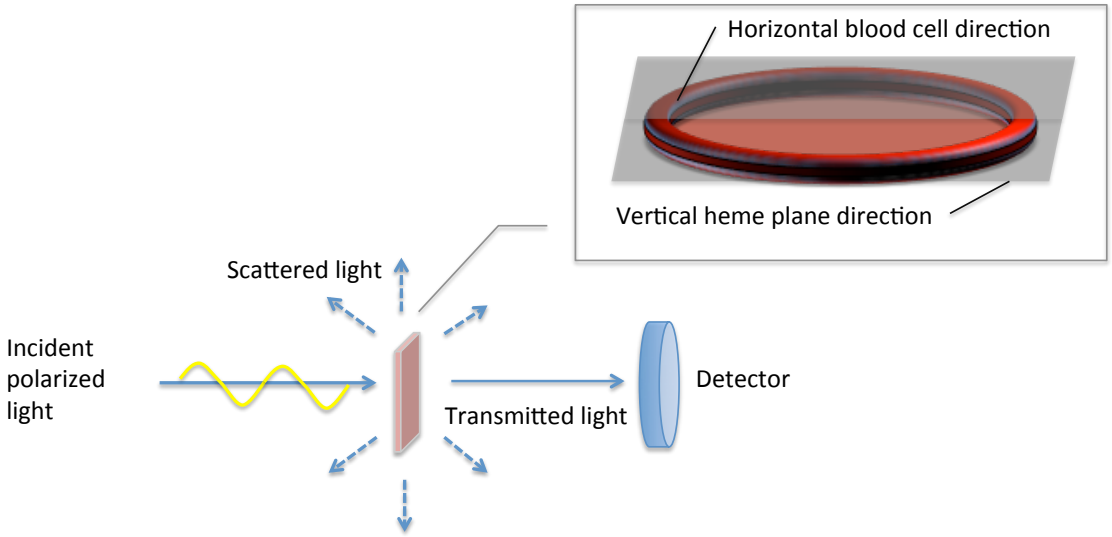

Figure 5.16: Illustration of a simplistic LD setup and the relative orientations of both cell and heme plane within a 1mm rectangular cuvette.

Although studies on healthy red blood cells have not been conducted with the aim of aligning the long-axis of the cell with the direction of light polarisations (due to the lack of awareness regarding these internal structures) studies have been conducted regarding the sickle-hemoglobin mutation[102]. This mutation in one of the beta hemoglobin sub-units, and amongst other effects alterations to the hydrophobic regions within the protein lead to the formation of long polymerised strands of hemoglobin. These strands have been observed to form such that they are orientated across the long axis of the cell[100].

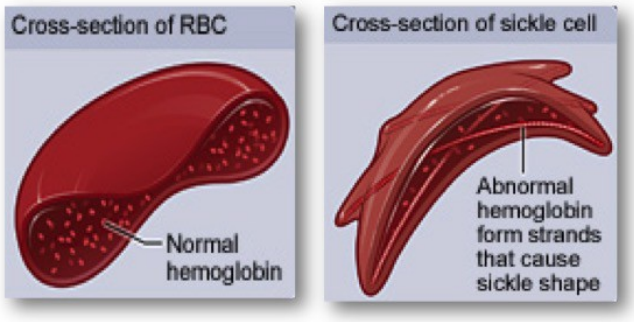

Figure 5.17: A cross-section of a sickle red blood cell, demonstrating the polymerised hemoglobin-S strands forming along the long axis forcing the characteristic distortion of shape[107].

A closer look at the orientation of the individual proteins within these sickle-hemoglobin polymers would appear to indicate that on average the plane of the heme groups are aligned such that they are perpendicular (face-on) to the direction of the polymer strand. In studies contrasting absorbance from light polarised parallel or perpendicular to the long-axis of these sickled cells, an increased absorbance was also observed in those cells aligned parallel to the polarisation direction[82,107]. Sickle cells appear to demonstrate an increased absorbance in the perpendicular orientation to the cellular long axis, serving as an indication of the heme orientation within those cells. This further supports the statement that heme planes are oriented such that they are perpendicular to the hemoglobin polymers that stretch parallel to the long axis of the cell. These sickle-hemoglobin studies are of particular interest because it matches the results provided in this work, which also demonstrate heme planes oriented perpendicular to the cellular long-axis. Although it would need further study, this implies that the underlying forces (e.g. hydrophobic interactions) that induce these strands to form are already present in healthy cells. This would imply that the sickle-hemoglobin mutations, instead of introducing new interactions simply exacerbate ones that are already present and influencing protein behaviour, albeit to a much lesser extent.

With evidence now that suggests that the positive transition hemoglobin peak spectra observed is scattering derived, the remaining assays can now be correctly evaluated. Regarding the concentration assay, the minimal change in resonance scattering is understandable since there should not be strong enough steric interactions at these relatively low concentrations to influence the extent of cellular alignment within the sample. Additionally since the cell interior is unchanged there should be no change in the amount of aligned proteins in each sample when adjusted with respect to concentration. The non-resonant scattering, however, is obviously influenced by the extent to which the cells pack together. Since this is purely a baseline shift and has no relation to the heme peak pattern presented within resonance scattering, we can attribute this scattering contribution to the cell as a whole. As observed in Chapters 2–3 (particularly regarding the orientation of uniaxial liposomes), when dealing with particles in the RGD size regime theory regarding LD, this non-resonant scattering

follows a smooth $1/\lambda^4$ curve for particles oriented in the flow direction. If the cells were to be oriented in the opposite direction, however, this would be reversed, demonstrating a $-1/\lambda^4$ dependent curve instead.

Another characteristic of large particle samples that has been examined in related works is multiple-scattering[101], where the scattering distribution detected is the cumulative contribution from multiple layered cells. In other words, the scattering from one particle can strike a second producing another scattering distribution and so on until reaching the detector. At low concentrations this effect is minimized, since the fewer particles that are in close proximity the lesser this layering of scattering effect will occur. Unfortunately, although this phenomenon has been characterized, the sheer complexity of the resultant scattering intensity distribution after passing through multiple cells makes calculation of this distribution exceptionally difficult. Regarding the tonicity/basic assay and their intended use to examine the extent of intracellular alignment, the spectra cannot be so clearly separated into components. Unlike the concentration/pathlength assays most changes to the intracellular environment also influence cell geometry, which may also influence the extent of sedimentary alignment (and therefore intercellular alignment), and also the extent of multiple scattering exhibited. Therefore in a similar vein to the previous assays what results is primarily a mixture of altered peak sizes and baseline scattering intensities.

Firstly, regarding hypotonic solutions, in contrast to that of an isotonic spectrum, the reduction in osmotic pressure noticeably reduced resonance scattering, with minimal baseline reduction. These effects are clearly visible in weakly hypotonic suspensions and are greatly exacerbated in solutions with lower osmotic pressures. We can assume that as the cells swell the intracellular protein arrays are disrupted, in addition to decreased intercellular alignment (altered sedimentary forces due to distortion from a discoid geometry). In contrast the transition from discoid to compressed discoid/echinocyte (hypertonic) presents a reduction in resonance LD with a less pronounced baseline scattering. The concentration inside each cell is already very high, so there is only limited disruption that can be made to the protein arrays by the small volume reduction. In this latter case the alteration in baseline is harder to analyse since there is a transition from biconcave to compressed disc geometry, as

volume is removed, to that of an echinocyte (spine-coated sphere). The compressed form should have an increased polarisability (easier for thinner discs to align in contrast to thicker ones), however, the spiny spherical form of the echinocyte (Fig. 5.3) should oppose this. In addition considering the influence of multiple scattering on this mixed geometry suspension makes further detailed analysis difficult. The basic assay, however, complements this by causing a geometry shift to exclusively the echinocyte form (via disruption of the membrane cytoskeleton) without any corresponding volume loss since isotonicity is maintained. Here much the same baseline alteration is seen without a significant corresponding change in resonance scattering. There is still a noticeable reduction, after all the extent of cell alignment is still being reduced (reducing the total amount of aligned hemes) but the intracellular arrays should not be affected as greatly. We can therefore attribute the baseline change in our hypertonic solutions to be primarily derived from echinocyte geometries. In addition the reduced resonance scattering confirms that intracellular disruption from volume alterations has a significant impact aside from the influence of geometry on the degree of cellular alignment.

Lastly in the metabolic assays, it was observed that when samples were allowed to incubate at elevated temperatures they exhibited a reduction in non-resonant scattering across the board with minor reduction in the Soret (415nm) resonant scattering peak. As cells respire, carbonic acid is produced lowering the pH of the surrounding cytosol which as mentioned above can lead to reductions in pH can be a driving force for the shift in cellular geometry from biconcave to stomatocyte formation[91,95]. What should have been observed therefore is an alteration in the cellular shape to cupped/bloated ovoid with minimal to no change in internal volume, similar to that demonstrated in the pH assays. The resulting spectra therefore follows a similar logic in which a disruption to inter-cellular alignment is responsible for the reduction in non-resonant scattering with minimal change in resonant scattering due to the lack of internal volume loss driven intra-cellular disruption.

5.9 Conclusions

The initial aims for this section of work was to explore and investigate the LD spectrum produced by the simplest of mammalian cells. Over the course of the investigation, it became apparent that most of the LD signal observed was in fact being produced by scattered light instead of the typical absorbance. It was also hypothesized that cells aligned in the absence of flow, via sedimentation due to gravitational forces, which our collected data appears to support. This is unlike standard LD analysis that typically focuses on particles that are too small to be influenced by such forces (forces they are subjected to, like Brownian Motion, are random and as such do not produce a prevailing particle orientation). Where shear flow is required to induce alignment in standard LD, when dealing with red blood cells stationary (or flow-off) samples were demonstrated to provide higher LD intensities. By means of a variety of assays intended to alter both the geometry and surrounding environment of the blood cells it also became apparent that within the red blood cell there exist oriented structures. Contrasting the transition sign of 'scattering-free' LD (flow-off samples placed adjacent to the detector), and literature work conducted involving the fluid dynamics of falling discs, the orientation of the internal heme groups comprising this internal protein array relative to the cellular orientation was also determined (Fig 5.16) [96].

Although it has been speculated in past literature that this protein rich cytosol existed in a liquid-crystal type state, and various assays such as x-ray crystallography, and more recently resonance Raman spectroscopy[98], this is the first study that so clearly demonstrated the existence of these structures. The potential implications with regards to the under-lying forces behind the sickle-hemoglobin mutation should be of great interest provided that the postulated hypothesis is correct, that the forces that lead to the formation of sickle-hemoglobin are already present and acting within the cell and that the mutation in its structure simply exacerbates these forces. If proven true, with sufficient research a protocol could be developed that controllably disturbs the intra-cellular 'pseudo liquid-crystal' protein arrays. Although this is likely to interfere with the oxygen-transfer of the diseased cell, this approach could work to limit the production of these sickle-fibres. Since sickle-fibres are primarily responsible

for the deformation of the red blood cells into the diseased state (Fig 5.17), this leads to various symptoms such as swellings as cells become stuck within blood vessels[108]. If successful, the more debilitating of these effects on the cell shape and the consequential symptoms could be alleviated. Lastly regarding practical applications it would appear that for medical practice, another relative easy method for the monitoring of both cellular and buffer stability would be of great use. With the establishment of golden standards and the quantification of what LD intensity would define a healthy cell over an un-healthy one, for a given concentration, the state of the cell could be determined from a single wavelength. The capacity to rely on sedimentary forces to align the cells instead of shear flow also greatly eases the collection of data. Due to the ease of collection, the potential speed of this approach could also be applied prior to a routine clinical blood test as a preliminary test to determine if a more in depth examination is required. The more time consuming full spectrum analysis could be reserved for a more in depth analysis of the red blood cell geometry (or even other features such as the formation of aggregates). Application of the full spectrum analysis could even be used to examine the state of samples in longer-term storage and approaching expiry.

Chapter 6: Conclusions and future work

6.1.1 Summary

The primary premise behind this thesis has been the development of linear dichroism for applications regarding living cells, and similar structures, to bridge the resolution gap between microscopic and spectroscopic disciplines. LD spectra from these systems were considered to be a composite spectrum comprised of the spectral contributions from each aligning component in that system. Studies were conducted to examine the spectra produced by most common individual components found in biological systems and their relation to multiple component systems in increasing order of complexity. LD spectra from each system was then deconvoluted in terms of the peak contributions from each component, although quantitative analysis of peak intensity was not possible at this time. Additional features that alter this basic cumulative behaviour, such as the $\pi - \pi^*$ stacking of DNA bases, were also experimentally demonstrated.

The most complex system examined, that of the equine red blood cell, demonstrated an LD spectrum unlike any other system examined. Even in the absence of flow-induced orientation an LD spectrum with a peak distribution that corresponded exclusively to that of hemoglobin was observed. In order to produce such a signal both inter-cellular and intra-cellular (protein) alignment must be present. This inherent cellular alignment was investigated in terms of the environmental effects ever-present on all samples (time, pressure, temperature, gravity) and, via a process of elimination, sedimentary action was determined to be the most probable cause. Contrasts against heme plane orientations within sickle cells further serves as an indication for the average alignment of the absorbing chromophore within each cell. By assuming that the same intracellular alignment occurs in each cell, a wide degree of motion would be permitted in any edge-on downwards oriented cell, provided the vertical orientation of the cellular long-axis is preferred. Further analysis then demonstrated the existence of

light scattering as the driving factor behind the LD spectra instead of the commonly observed absorbance as part of studies into the solid angle of detection from the sample. This is a rare phenomenon is little understood, however it is characterised as resonance scattering where the light scattering produced by a sample is increased at wavelengths that share an absorbance peak (in essence 'mimicking' the absorbance spectrum). Various protocols conducted (i.e basic and tonicity assays) examined the cellular behaviour when either the internal or external environment is altered, and the corresponding influence on intracellular *heme* alignment. It was possible to determine that spectra produced by red blood cells are constructed from simultaneously resonant and non-resonant scattering being responsible for the observed spectra; the former being responsible for the characteristic hemoglobin peak pattern, and the latter comprising baseline non-peak specific intensity shifts (attributed to multiple and back-scattering).

To further examine the influence of scattering behaviour on LD spectra, a study into both commonly accepted scattering theory and its practical application was conducted. Non-linear regression models were found to be lacking in accuracy, and in the literature there appeared to be little to no practical applications of the more complex theory regarding LD. Modifications to the theory were then implemented according to the experimental setup (i.e. the inclusion of the solid angle of detection into the total angular scattering intensity measured). Detailed data regarding volume losses, deformation and the corresponding LD spectra of vesicles under flow were used as a model for which to study the application of this theory. This approach appeared to be capable of correcting the scattering contribution of a given spectrum (by the use of reliable vesicle samples as 'gold standards' for deformation and orientation values previously ascertained in the literature) and return values for deformation and orientation parameters as a result of the examined scattering.

6.1.1 Applications and Future work

As far as applications go, the studies into spectral deconvolution of multiple-component systems taken to the extreme (with healthy normal eukaryotic cells) should provide use as an analytical tool. In the absence of the resonance scattering observed

in red blood cells samples, the intensity of a given peak within the cellular LD spectrum should give information about the position, quantity and relative orientation of any organised structures within that system. As far as future work goes, the development of a more extensive component database (e.g. lipids) in conjunction with an increase in the complexity of the multiple component systems with known degrees of component orientation, to act as model systems would be advisable. Regarding the investigations into red blood cell work, several areas could do with further investigation (which were not conducted due to either equipment or time constraints), of particular note are the areas of; oxygen gradients acting as an orientation inducing force for hemoglobin, sedimentary dynamics of the cells, sickle-cell LD, and ideally a direct microscopic imaging of the cells under LD analysis. Current practical applications for this field of work (other than novel fundamentals regarding hemoglobin substructures) extend primarily to the clinical field where it could present a function in the examination of blood cell health or that of prepared stocks. Lastly the theoretical work carried out for the calculation of scattering has several areas in which it could be expanded upon. This approach should theoretically be possible to be modified such that the scattering observed in circular dichroism samples is also available for calculation. Additionally since Rayleigh and Mie theories overlap in this region of particle size, a more detailed investigation of the trends and dependence is in order as well as any potential alternatives for this specific size regime. For applications, currently as long as samples are provided to act as standards for a given setup and exist within a similar size regime, scattering can be fitted, subtracted and used to calculate values for particle orientation and deformation for any LD or absorbance spectra. Additionally this branch of theory supports calculations for various particle shapes, of both solid and hollow nature, widening its range of applications for the simultaneously improvement of spectra and the derivation of additional information.

References

1. D. J. Stephens and V. J. Allan, *Science*, 2003, **300**, 82-86.
2. F. Schotte, M. H. Lim, T. A. Jackson, A. V. Smirnov, J. Soman, J. S. Olson, G. N. Phillips, M. Wulff and P. A. Anfinrud, *Science*, 2003, **300**, 1944-1947.
3. S. Mason, *Nature*, 1996, **381**, 488-488.
4. T. K. Gaylord and M. G. Moharam, *Proceedings of the Ieee*, 1985, **73**, 894-937.
5. H. G. J. Worth, *Annals of Clinical Biochemistry*, 1985, **22**, 343-350.
6. K. Kneipp, Y. Wang, H. Kneipp, L. T. Perelman, I. Itzkan, R. Dasari and M. S. Feld, *Physical Review Letters*, 1997, **78**, 1667-1670.
7. M. Roy, J. K. Nelson, R. K. MacCrone, L. S. Schadler, C. W. Reed, R. Keefe and W. Zenger, *Ieee Transactions on Dielectrics and Electrical Insulation*, 2005, **12**, 629-643.
8. S. Takamori, M. Holt, K. Stenius, E. A. Lemke, M. Gronborg, D. Riedel, H. Urlaub, S. Schenck, B. Brugger, P. Ringler, S. A. Muller, B. Rammner, F. Grater, J. S. Hub, B. L. De Groot, G. Mieskes, Y. Moriyama, J. Klingauf, H. Grubmuller, J. Heuser, F. Wieland and R. Jahn, *Cell*, 2006, **127**, 831-846.
9. M. Collinson and E. F. Bowden, *Analytical Chemistry*, 1992, **64**, 1470-1476.
10. N. C. Santos and M. Castanho, *Biophysical Journal*, 1996, **71**, 1641-1650.
11. I. S. Saidi, S. L. Jacques and F. K. Tittel, *Applied Optics*, 1995, **34**, 7410-7418.
12. T. R. Dafforn and A. Rodger, *Current Opinion in Structural Biology*, 2004, **14**, 541-546.
13. C. Hiort, B. Norden and A. Rodger, *Journal of the American Chemical Society*, 1990, **112**, 1971-1982.
14. C. A. Stover, D. L. Koch and C. Cohen, *Journal of Fluid Mechanics*, 1992, **238**, 277-296.
15. Y. H. Chen, J. T. Yang and H. M. Martinez, *Biochemistry*, 1972, **11**, 4120-&.
16. K. Ishihara, H. Nomura, T. Mihara, K. Kurita, Y. Iwasaki and N. Nakabayashi, *Journal of Biomedical Materials Research*, 1998, **39**, 323-330.
17. B. R. Masters, P. T. C. So, C. Buehler, N. Barry, J. D. Sutin, W. W. Mantulin and E. Gratton, *Journal of Biomedical Optics*, 2004, **9**, 1265-1270.
18. T. Maniatis, A. Jeffrey and D. G. Kleid, *Proceedings of the National Academy of Sciences of the United States of America*, 1975, **72**, 1184-1188.
19. F. Chen and N. J. Tao, *Accounts of Chemical Research*, 2009, **42**, 429-438.
20. A. Ghosh and M. Bansal, *Acta Crystallographica Section D-Biological Crystallography*, 2003, **59**, 620-626.
21. P. Lincoln, A. Broo and B. Norden, *Journal of the American Chemical Society*, 1996, **118**, 2644-2653.
22. B. Henrissat and A. Bairoch, *Biochemical Journal*, 1993, **293**, 781-788.
23. H. Maeda and N. Dudareva, in *Annual Review of Plant Biology, Vol 63*, ed. S. S. Merchant, Annual Reviews, Palo Alto, 2012, vol. 63, pp. 73-105.
24. A. A. Adzhubei and M. J. E. Sternberg, *Journal of Molecular Biology*, 1993, **229**, 472-493.
25. A. Caputo, E. Caci, L. Ferrera, N. Pedemonte, C. Barsanti, E. Sondo, U. Pfeffer, R. Ravazzolo, O. Zegarra-Moran and L. J. V. Galietta, *Science*, 2008, **322**, 590-594.
26. R. Marrington, M. Seymour and A. Rodger, *Chirality*, 2006, **18**, 680-690.
27. R. C. Murdock, L. Braydich-Stolle, A. M. Schrand, J. J. Schlager and S. M. Hussain, *Toxicological Sciences*, 2008, **101**, 239-253.
28. OpenStax, *Anatomy & Physiology*. OpenStax CNX. viewed 14 August 2017 http://cnx.org/contents/14fb4ad7-39a1-4eee-ab6e-3ef2482e3e22@8.25.
29. A Rodger, 2012, *11._circular_dichroism.ppt*, Powerpoint presentation, University of Warwick, viewed 14 August 2017.

30. T Shafee, *Summary of protein structure (primary, secondary, tertiary, and quaternary) using the example of PCNA. (PDB: 1AXC),* viewed 14 August 2017, https://commons.wikimedia.org/wiki/File:Protein_structure_(3).png.
31. A Rodger, 2012, *11._linear_dichroism.ppt*, Powerpoint presentation, University of Warwick, viewed 14 August 2017.
32. Van De Hulst, *Light Scattering by Small Particles*; Wiley: New York, 1957.
33. Hahn. W D, Diagnostic tutorial, *Light scattering theory: Chapter 7,* Department of Mechanical and Aerospace Engineering: University of Florida, 2009, Available from: http://plaza.ufl.edu/dwhahn/Rayleigh%20and%20Mie%20Light%20Scattering.pdf [17 August 2017].
34. W. Mahmood, M. Y.; Fen Y; Yee L, *American Journal of Applied Sciences*, 2009, **6,** 328-331.
35. A. Panacek, L. Kvitek, R. Prucek, M. Kolar, R. Vecerova, N. Pizurova, V. K. Sharma, T. Nevecna and R. Zboril, *Journal of Physical Chemistry B*, 2006, **110**, 16248-16253.
36. G. H. Meeten, *Journal of Colloid and Interface Science*, 1981, **84**, 235-239.
37. N. Mikati, J. Nordh and B. Norden, *Journal of Physical Chemistry*, 1987, **91**, 6048-6055.
38. J. R. A. McLachlan, D. J. Smith, N. P. Chmel and A. Rodger, *Soft Matter*, 2013, **9**, 4977-4984.
39. W. Yoshikawa, H. Akutsu and Y. Kyogoku, *Biochimica Et Biophysica Acta*, 1983, **735**, 397-406.
40. S. R. Strand, S. Kim and S. J. Karrila, *Journal of Non-Newtonian Fluid Mechanics*, 1987, **24**, 311-329.
41. M. Castanho, N. C. Santos and L. M. S. Loura, *European Biophysics Journal with Biophysics Letters*, 1997, **26**, 253-259.
42. Y. H. M. Chan and S. G. Boxer, *Current Opinion in Chemical Biology*, 2007, **11**, 581-587.
43. B. A. Lewis and D. M. Engelman, *Journal of Molecular Biology*, 1983, **166**, 211-217.
44. H. Noguchi and G. Gompper, *Proceedings of the National Academy of Sciences of the United States of America*, 2005, **102**, 14159-14164.
45. M. Ardhammar, P. Lincoln and B. Norden, *Proceedings of the National Academy of Sciences of the United States of America*, 2002, **99**, 15313-15317.
46. T. M. Allen and L. G. Cleland, *Biochimica Et Biophysica Acta*, 1980, **597**, 418-426.
47. N. C. Maiti, S. Mazumdar and N. Periasamy, *Journal of Physical Chemistry B*, 1998, **102**, 1528-1538.
48. D. Axelrod, *Traffic*, 2001, **2**, 764-774.
49. P. Croce and L. Nevot, *Revue De Physique Appliquee*, 1976, **11**, 113-125.
50. A. Nuraeva, S. Vasilev, D. Vasileva, P. Zelenovskiy, D. Chezganov, A. Esin, S. Kopyl, K. Romanyuk, V. Y. Shur and A. L. Kholkin, *Crystal Growth & Design*, 2016, **16**, 1472-1479.
51. J. D. Hartgerink, E. Beniash and S. I. Stupp, *Science*, 2001, **294**, 1684-1688.
52. K Lloyd, *Stability of Lipid Vesicles in Flow at High Shear Rates*, Thesis, Doctor of Philosophy, University of Warwick, Coventry. 2015
53. S Norton, *Linear dichroism spectroscopy and biophysics of an amyloid protein*, Thesis, Doctor of Philosophy, University of Warwick, Coventry. 2015
54. N Bengt; R Alison, D Timothy R, *Linear dichroism and circular dichroism: A textbook on polarized-light spectroscopy*. Cambridge, UK: RSC Publishing, 2010
55. C Montgomery, *The self-assembly of diphenylalanine fibres*, Thesis, Doctor of Philosophy, University of Warwick, Coventry. 2015
56. T. M. Fischer, M. Stohrliesen and H. Schmidschonbein, *Science*, 1978, **202**, 894-896.
57. A. D. Dupuy and D. M. Engelman, *Proceedings of the National Academy of Sciences of the United States of America*, 2008, **105**, 2848-2852.

58. L. Cordone, A. Cupane, M. Leone and E. Vitrano, *Biophysical Chemistry*, 1986, **24**, 259-275.
59. J. S. Pedersen, *Advances in Colloid and Interface Science*, 1997, **70**, 171-210.
60. A. L. Yuille and T. A. Poggio, *Ieee Transactions on Pattern Analysis and Machine Intelligence*, 1986, **8**, 15-25.
61. M. R. Hicks, J. Kowalski and A. Rodger, *Chemical Society Reviews*, 2010, **39**, 3380-3393.
62. S. Matile, N. Berova, K. Nakanishi, J. Fleischhauer and R. W. Woody, *Journal of the American Chemical Society*, 1996, **118**, 5198-5206.
63. C. H. Lee, H. Mizusawa and T. Kakefuda, *Proceedings of the National Academy of Sciences of the United States of America-Biological Sciences*, 1981, **78**, 2838-2842.
64. W. Wickner, *Proceedings of the National Academy of Sciences of the United States of America*, 1976, **73**, 1159-1163.
65. W. A. Eaton and J. Hofrichter, *Methods in enzymology*, 1981, **76**, 175-261.
66. P. A. Fantes and C. S. Hoffman, *Genetics*, 2016, **203**, 621-629.
67. L. Makowski, *Current Opinion in Structural Biology*, 1994, **4**, 225-230.
68. H. Noguchi and G. Gompper, *Proceedings of the National Academy of Sciences of the United States of America*, 2005, **102**, 14159-14164.
69. S. Chien, *Annual Review of Physiology*, 1987, **49**, 177-192.
70. D. N. Wang, *Febs Letters*, 1994, **346**, 26-31.
71. D. E. Discher, D. H. Boal and S. K. Boey, *Biophysical Journal*, 1998, **75**, 1584-1597.
72. S. E. Lux, *Blood*, 2016, **127**, 187-199.
73. R. K. Kaul and H. Kohler, *Klinische Wochenschrift*, 1983, **61**, 831-837.
74. M. R. Dayer, A. A. Moosavi-Movahedi and M. S. Dayer, *Protein and Peptide Letters*, 2010, **17**, 473-479.
75. W. G. Zijlstra and A. Buursma, *Comparative Biochemistry and Physiology B-Biochemistry & Molecular Biology*, 1997, **118**, 743-749.
76. M. Rinaudo, *Progress in Polymer Science*, 2006, **31**, 603-632.
77. New Health Advisor, *High Red Blood Cell Count*, http://www.newhealthadvisor.com/High-Red-Blood-Cell-Count.html, 2014, [viewed 20 August 2017],
78. Trun N, Trempy J, *Fundamental bacterial genetics*, Blackwell Science Ltd, Oxford, 2004
79. O D Morgan, *The Cell Cycle,* New Science Press, London, 2007
80. B J Wallach, *Interpretation of diagnostic tests*, Lippincott Williams & Wilkins, Philadelphia, 2007.
81. M.F. Perutz, Nature, **161**, 1948, 204.
82. J. T. Finch, M. F. Perutz, J. F. Bertles and J. Dobler, *Proceedings of the National Academy of Sciences of the United States of America*, 1973, **70**, 718-722.
83. M. M. Gedde, D. K. Davis and W. H. Huestis, *Biophysical Journal*, 1997, **72**, 1234-1246.
84. A. K. Solomon, M. R. Toon and J. A. Dix, *Journal of Membrane Biology*, 1986, **91**, 259-273.
85. L. B. Leverett, E. C. Lynch, C. P. Alfrey and J. D. Hellums, *Biophysical Journal*, 1972, **12**, 257-&.
86. R. Skalak, P. R. Zarda, K. M. Jan and S. Chien, *Biophysical Journal*, 1981, **35**, 771-781.
87. A. Yamamoto, S. Mishima, N. Maruyama and M. Sumita, *Journal of Biomedical Materials Research*, 2000, **50**, 114-124.
88. U. Seifert, *Advances in Physics*, 1997, **46**, 13-137.
89. S. V. Tsinopoulos and D. Polyzos, *Applied Optics*, 1999, **38**, 5499-5510.
90. T. Asakura and J. Mayberry, *Journal of Laboratory and Clinical Medicine*, 1984, **104**, 987-994.
91. M. Rasia and A. Bollini, *Biochimica Et Biophysica Acta-Biomembranes*, 1998, **1372**, 198-204.

92. J. L. R. Baum, R. L. Jones, T. J. Manning, J. Nienow and D. Phillips, *Acta Pharmaceutica*, 2012, **62**, 201-209.
93. N. Adili, M. Melizi and H. Belabbas, *Veterinary World*, 2016, **9**, 960-963.
94. M. H. Antonelou, A. G. Kriebardis and I. S. Papassideri, *Blood Transfusion*, 2010, **8**, S39-S47.
95. R. P. Henry and M. G. Wheatly, *American Zoologist*, 1992, **32**, 407-416.
96. S. B. Field, M. Klaus, M. G. Moore and F. Nori, *Nature*, 1997, **388**, 252-254.
97. P. J. Collings, E. J. Gibbs, T. E. Starr, O. Vafek, C. Yee, L. A. Pomerance and R. F. Pasternack, *Journal of Physical Chemistry B*, 1999, **103**, 8474-8481.
98. B. R. Wood, L. Hammer and D. McNaughton, *Vibrational Spectroscopy*, 2005, **38**, 71-78.
99. S. Bettati and A. Mozzarelli, *Journal of Biological Chemistry*, 1997, **272**, 32050-32055.
100. Hofricht.J, Hendrick.Dg and W. A. Eaton, *Proceedings of the National Academy of Sciences of the United States of America*, 1973, **70**, 3604-3608.
101. J. Korringa, *Physics Reports-Review Section of Physics Letters*, 1994, **238**, 341-360.
102. G L, Deaver, C F Whitten , J H L Watson, *Federation Prec*. **22**, 1963, 601.
103. Y C Fung, *Biomechanics,* Springer, New York, 1993.
104. G T Papaioannou, C Stefanadis, *Hellenic J Cardiol*, **46**, 2005, 9-15.
105. T L Goodhead, M F MacMillan, *Adv Physiol Educ,* **41**, 2017, 298–305
106. Klug A, Kreuzer F, Roughton F J W, *Helv. Physiol*., **14**, 1956, 121
107. National Heart and Lung Institute, *What Is Sickle Cell Disease?*, https://www.nhlbi.nih.gov/health/health-topics/topics/sca, 2017, [viewed 20 August 2017],
108. National Heart and Lung Institute, *What Are the Signs and Symptoms of Sickle Cell Disease*, https://www.nhlbi.nih.gov/health/healthtopics/topics/sca/signs, 2017, [viewed 20 August 2017],
109. E. Brown, E. S. Pysh, *Journal of Chemical Physics*, 1972, **56**, 31-&.
110. Rodger A, Dorrington G, Ang D L, *Analyst*, 2016, **141**, 6490-6498
111. Rodger A, Dafforn T, *Current Opinion in Structural Biology*, 2004, **14**, 541-546
112 Bechinger B, Ruysschaert J M, Goormaghtigh E, *CellPress,* 1999, **76**, 552-563

Appendix A

A.1 Liposome LD scattering calculation

Fluorescence leakage data for DMPC samples collected by Norton *et al*.[53], however the lack of resolution in these spectra renders it unsuitable for analysis without curve fitting.

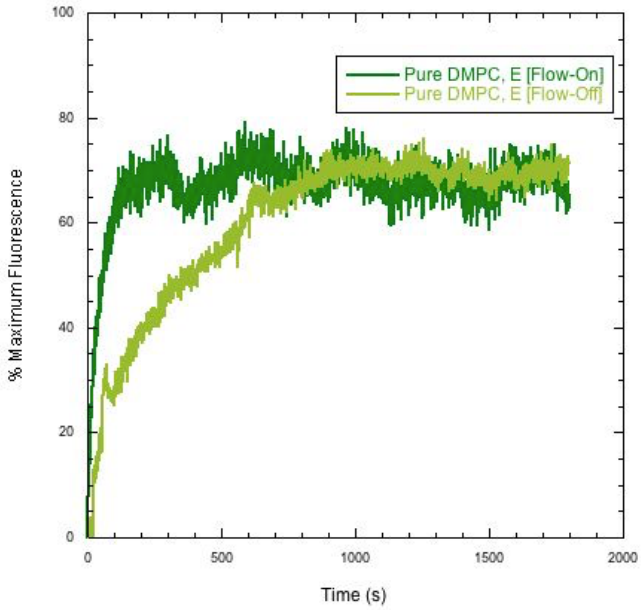

Figure A.1: Calcein leakage fluorescence spectra collected from DMPC vesicles under flow on and off conditions, [conc 20ug/ml, pathlength 0.5mm]

Additional scattering fits were also generated for both DMPC and replicate BTLE LD data from their respective LD spectra under flow. DMPC spectra are of extremely low intensity and as demonstrated above are highly leaky/deformable under flow. The baseline scattering is also different to as observed in all other cases due to the high deformation, which makes it difficult to fit with any of the approaches developed. BTLE alternatively is well resolved and can be fit nicely, however the variability even between 'identical' repeats is high, Fig A.2.

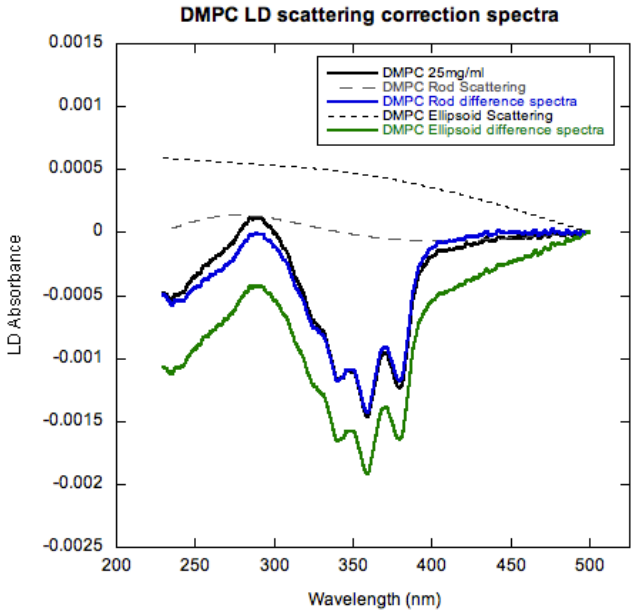

Figure A.2: DMPC LD scattering correction spectra for various vesicle scattering fitting approaches, [concentration 25mg/ml, pathlength 0.5mm]

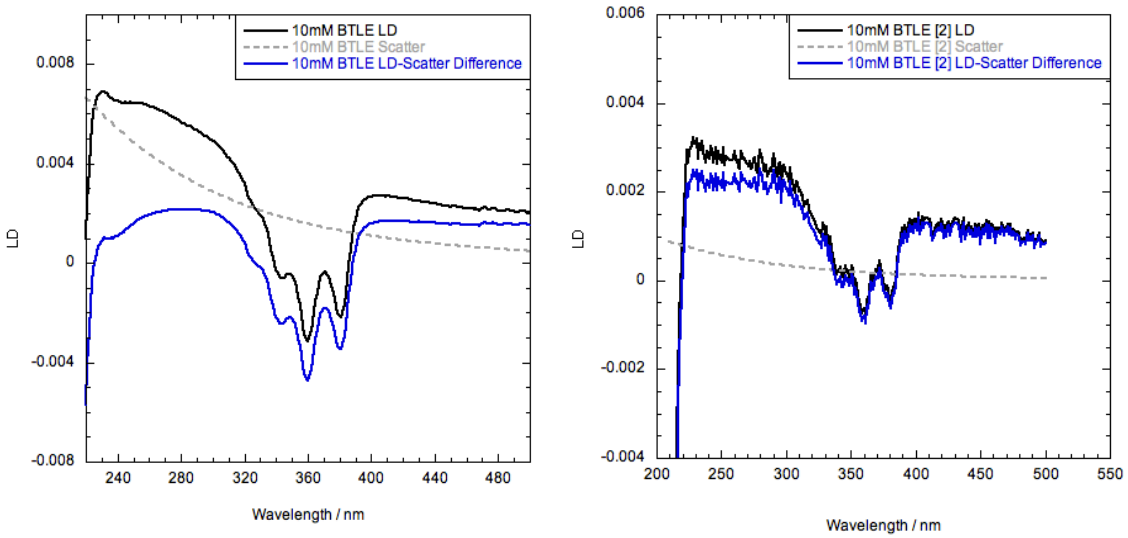

Figure A.3: BTLE LD scattering correction spectra for two identical repeats, [concentration 10mM, pathlength 0.5mm]

A.2 Aromatic amino acid spectra

As part of the construction of the component spectral database, much like with regards to the nucleotide spectra, each aromatic amino acid has their corresponding absorbance and CD spectra recorded. Spectra were also collected for the far-UV CD however they proved extremely variable in quality.

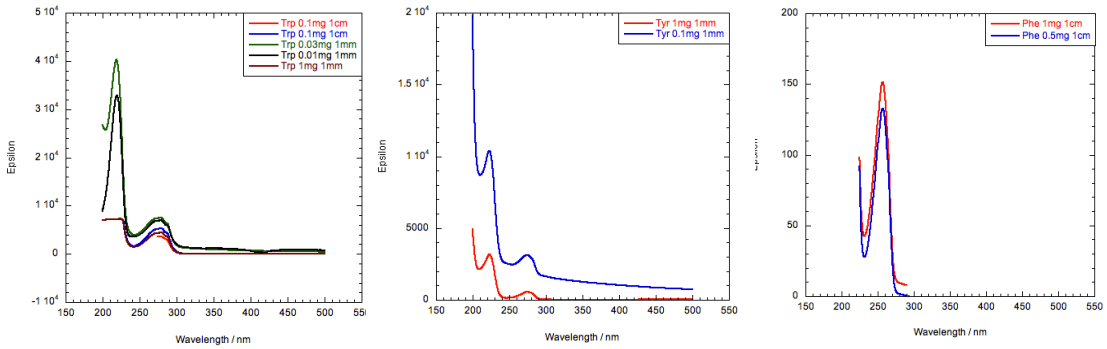

Figure A.4: Absorbance spectra for each of the aromatic amino acids at a variety of concentrations and pathlength (as denoted in the corresponding graph legend).

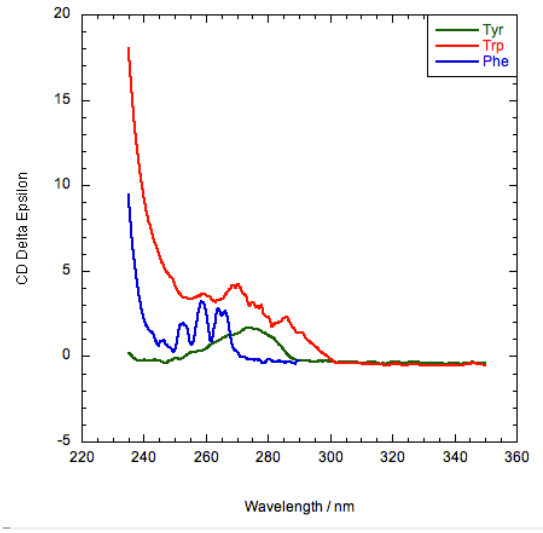

Figure A.5: Near-UV CD spectra for each of the aromatic amino acids at 1mg/ml, [pathlength (Trp, Tyr) 1mm, (Phe) 1cm].

A.3 M13 fitting spectra

As part of the M13 bacteriophage study although we do not possess individual protein spectra for which to use as components there is still the capacity to use the M13 absorbance spectrum to produce Gaussians and contrast those to the M13 LD data. This allows the observation of further features, such as the exciton coupling at 273 nm, not immediately obvious from the absorbance spectrum alone.

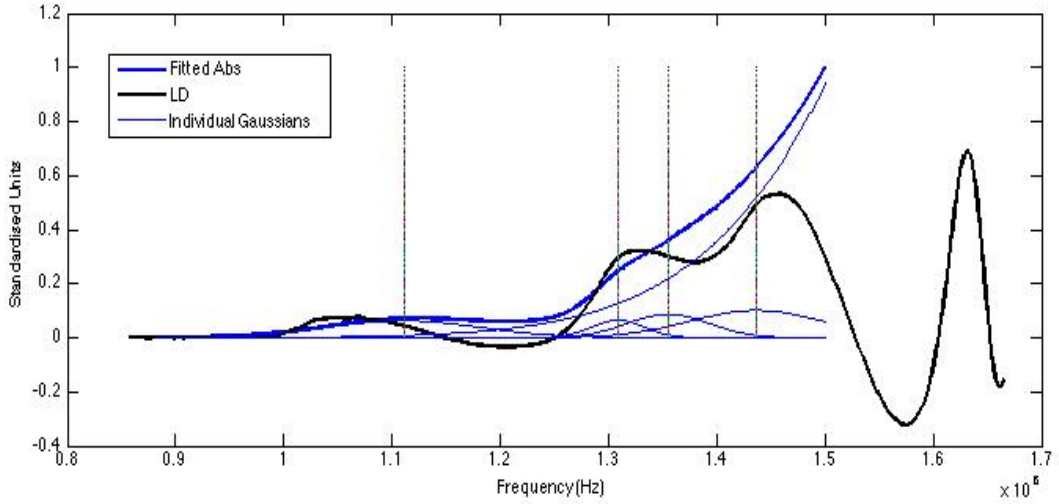

Figure A.6: Overlaid spectrum of the fitted absorbance spectrum for M13 with associated Gaussians, and the M13 LD spectrum. Vertical lines represent peak values for the component Gaussians.

A.4 Matlab scattering program code.

***VesicleCCalc.m*: Code for determination of liposome short semi-axis and associated leakage for a given long semi-axis 'c', provided the surface area matches that of a sphere of radius 'r'.**

```
function [Eval] = VesicleCCalc(c,r)

%Ellipse Vesicle Deformation

SSA = 4*pi*r^2;
SVol = (4/3)*pi*(r^3);

syms a
Eeqn = 4*pi*( ((((c*a)^1.6)+((c*a)^1.6)+((a^2)^1.6))/3)^(1/1.6)) == SSA;
b = vpasolve(Eeqn,a); %radius  parallel to axis of revolution (ellipsoid short semi-
axis))
Eval = double(b);
EVol = eval((4/3)*pi*(c*(b^2)));
EllipseVolRatioPercent = (1-((EVol/SVol)))*100;

assignin('base', 'EllipseVolRatioPercent', EllipseVolRatioPercent);
assignin('base', 'EllipseMinorSemiAxis', Eval);
assignin('base', 'EllipseMajorSemiAxis', c);

end
```

***VesicleSCalc.m*: Code for determination of liposome short semi-axis and associated leakage for a given long semi-axis 'c', provided the surface area matches that of a sphere of radius 'r' increased by a factor 'Stretch'.**

```
function [Eval] = VesicleSCalc(c,r,Stretch)

%Ellipse Vesicle Deformation

SVol = (4/3)*pi*(r^3);
SSA = (4)*pi*r^2;

syms a
ESA = SSA*(Stretch);
Eeqn = 4*pi*( ((((c*a)^1.6)+((c*a)^1.6)+((a^2)^1.6))/3)^(1/1.6)) == ESA;
b = vpasolve(Eeqn,a); %radius  parallel to axis of revolution (ellipsoid short semi-
axis)
Eval = double(b);
EVol = eval((4/3)*pi*(c*(b^2)));
EllipseVolRatioPercent = (1-((EVol/SVol)))*100;

assignin('base', 'EllipseVolRatioPercent', EllipseVolRatioPercent);
assignin('base', 'EllipseMajorSemiAxis', c);
assignin('base', 'EllipseMinorSemiAxis', Eval);

end
```

***VesicleConstantFinal.m*: Code for determination of liposome scattering, provided the surface area matches that of a sphere of radius 'r'.**

```
function VesicleConstantFinal
tic;

[FileName,PathName] = uigetfile({'*.txt','Data Files (.txt)';'*.*','All Files (*.*)'},
...
'Pick AnoTher File','/home/')
data1 = importdata(fullfile(PathName,FileName));

fullLD = data1(:,5);
fullWave = data1(:,1);
x = fullWave(1);
inter = 1;
LD(:,1) = fullWave(1:(inter*10):end);
LD(:,2) = fullLD(1:(inter*10):end);
endval = fullWave(end);

%%%%INPUT VARIABLES

Conc = [7.5];  %Molarity of sample.
L = [78.8]; %Particle long semi-axis.[POPC]

LipPerVesc = 81700; %%%Lipids in a 100nm vesicle
MicroConc = 83.25e-6; % Volume of capillary in l

Theta = (pi/2); % Polar angle of particle
rPhi = (pi/2); % Azimuthal angle of particle

rpm = 3000; %Shear Flow speed (rpm)

SphR = 50; %Non-flow liposome sphere radius (nm).

l = ((L)*2); % Length
d = (VesicleCCalc((l/2),SphR))*2; % Diameter of The particle.

yy = 1.5;
zz = 3;
ang = asin(yy/zz);
solidangle = pi-ang; % Solid angle measured

%%%% Orientation function

Ori = Orient(l/2,d/2,rpm);

%%%% k4 and R

n = 1;

while x < endval+inter

k = (2*pi)/x;
Bilayer = 4;
Vo = (4/3)*pi*((d/2)*(d/2)*(l/2));
Vi = (4/3)*pi*(((d/2)*(d/2)*(l/2))-Bilayer);
Vf = Vi/Vo;
m1 = 1.31848 + (6.662/(x - 129.2)); % Refractive index of the medium outside the
particle, water.
m2 = 1.451 + (6.662/(x - 129.2));

%%%% Lit Polarizability - Hollow

Pol = ((Vf*(((m1^2)-1)/((m1^2)+2)))+((1-Vf)*(((m2^2)-1)/((m2^2)+2))));

%%%%

cosgamma = @(Alp,Bet) (sin(Theta) .* cos(Bet/2) .* cos(rPhi - Alp)) - (cos(Theta) .*
sin(Bet/2));
```

```
%Hollow Ovoid
K2        =        @(Alp,Bet)        (2*k*m1).*(sin(Bet/2)).*(sqrt(((d/2)^2)+(((l/2)^2)-
((d/2)^2))*((cosgamma(Alp,Bet)).^2)));
G1 = ((d/2)-Bilayer)/(d/2);
G2 = @(Alp,Bet) G1.*K2(Alp,Bet);
R      =      @(Alp,Bet)      (3./((K2(Alp,Bet).^3)*(1-(G1)^3))).*(sin(K2(Alp,Bet))      -
(K2(Alp,Bet).*cos(K2(Alp,Bet))) + sin(G2(Alp,Bet)) - (G2(Alp,Bet).*cos(G2(Alp,Bet))) );
%solid

Idif  = @(Alp,Bet) (R(Alp,Bet).^2).*( (sin(Bet).^3) ).*cos(2*Alp);

Int = @(Alp,Bet) Ori.*Idif(Alp,Bet);

I(:,1) = LD(:,1);
I(n,2) = (integral2(Int,0,2*pi,0,solidangle));

y(n,1) =  (k.^2)*(Pol^2);

n = n+1;
x = x+inter;
end

%%%% I0/r^2 constant

I0r2 = 5e-11; % Lit Hollow (1.41% leakage) Constant

%%%% Particle Count

ParticleCount = ((Conc/1e3)/LipPerVesc)*6e23;
ParticleCouetteCount = ParticleCount * MicroConc;

%%%% Total Constant, N

Na = ParticleCouetteCount*I0r2;
Nb = 1/((4*pi)*(cos(solidangle)+1));
N = Na*Nb;

%%%% Total Variable, C

C(:,2) = y(:,1).*I(:,2);
C(:,1) = LD(:,1);

%%%% Total Scattering

T(:,2) = C(:,2)*N;
T(:,1) = I(:,1);

figure
plot(LD(:,1), LD(:,2),'color', 'black')
line(I(:,1), T(:,2), 'color', 'blue')
line(LD(:,1), LD(:,2)-T(:,2),'color', 'red')
legend('LD','Scattering','Corrected LD')

assignin('base', 'Wavelength', LD(:,1));
assignin('base', 'LD', LD(:,2));
assignin('base', 'TotalScat', T);
assignin('base', 'CorrectedLD', LD(:,2)-T(:,2));

toc
end
```

***VesicleStretchFinal.m*: Code for determination of liposome scattering, provided the surface area matches that of a sphere of radius 'r' increased by a factor 'Stretch'.**

```
function VesicleStretchFinal
tic;


[FileName,PathName] = uigetfile({'*.txt','Data Files (.txt)';'*.*','All Files (*.*)'},
...
'Pick AnoTher File','/home/')
data1 = importdata(fullfile(PathName,FileName));

fullLD = data1(:,3);
fullWave = data1(:,1);
x = fullWave(1);
inter = 1;
LD(:,1) = fullWave(1:(inter*10):end);
LD(:,2) = fullLD(1:(inter*10):end);
endval = fullWave(end);

%%%%INPUT VARIABLES

Conc = [10];  %Molarity of sample.
L = [72]; %Particle long semi-axis.[POPC]
Stretch = (7/100)+1; %Stretch = 1.0441 necessary to reach S=0.03 for Soy-PC at at POPC
Leakage of 3.65%.

LipPerVesc = 81700; %%%Lipids in a 100nm vesicle
MicroConc = 83.25e-6; % Volume of capillary in l

Theta = (pi/2); % Polar angle of particle
rPhi = (pi/2); % Azimuthal angle of particle

rpm = 3000; %Shear Flow speed (rpm)

SphR = 50; %Non-flow liposome sphere radius (nm).

l = ((L)*2); % Length
d = (VesicleSCalc((l/2),SphR,Stretch))*2; % Diameter of The particle.

yy = 1.5;
zz = 3;
ang = asin(yy/zz);
solidangle = pi-ang; % Solid angle measured

%%%% Orientation function

Ori = Orient(l/2,d/2,rpm);

%%%% k4 and R

n = 1;

while x < endval+inter

k = (2*pi)/x;
Bilayer = 4;
Vo = (4/3)*pi*((d/2)*(d/2)*(l/2));
Vi = (4/3)*pi*(((d/2)*(d/2)*(l/2))-Bilayer);
Vf = Vi/Vo;
m1 = 1.31848 + (6.662/(x - 129.2)); % Refractive index of the medium outside the
particle, water.
m2 = 1.451 + (6.662/(x - 129.2));

%%%% Lit Polarizability - Hollow

Pol = ((Vf*(((m1^2)-1)/((m1^2)+2)))+((1-Vf)*(((m2^2)-1)/((m2^2)+2))));

%%%%
```

```
cosgamma = @(Alp,Bet) (sin(Theta) .* cos(Bet/2) .* cos(rPhi - Alp)) - (cos(Theta) .*
sin(Bet/2));

%Hollow Ovoid
K2        =        @(Alp,Bet)        (2*k*m1).*(sin(Bet/2)).*(sqrt(((d/2)^2)+(((l/2)^2)-
((d/2)^2))*((cosgamma(Alp,Bet)).^2)));
G1 = ((d/2)-Bilayer)/(d/2);
G2 = @(Alp,Bet) G1.*K2(Alp,Bet);
R      =      @(Alp,Bet)      (3./((K2(Alp,Bet).^3)*(1-(G1)^3))).*(sin(K2(Alp,Bet))      -
(K2(Alp,Bet).*cos(K2(Alp,Bet))) + sin(G2(Alp,Bet)) - (G2(Alp,Bet).*cos(G2(Alp,Bet))) );
%solid

Idif  = @(Alp,Bet) (R(Alp,Bet).^2).*( (sin(Bet).^3) ).*cos(2*Alp);

Int = @(Alp,Bet) Ori.*Idif(Alp,Bet);

I(:,1) = LD(:,1);
I(n,2) = (integral2(Int,0,2*pi,0,solidangle));

y(n,1) =  (k.^2)*(Pol^2);

n = n+1;
x = x+inter;
end

%%%% I0/r^2 constants

I0r2 = 1.05e-11; % Lit Hollow

%%%% Particle Count

ParticleCount = ((Conc/1e3)/LipPerVesc)*6e23;
ParticleCouetteCount = ParticleCount * MicroConc;

%%%% Total Constant, N

Na = ParticleCouetteCount*I0r2;
Nb = 1/((4*pi)*(cos(solidangle)+1));
N = Na*Nb;

%%%% Total Variable, C

C(:,2) = y(:,1).*I(:,2);
C(:,1) = LD(:,1);

%%%% Total Scattering

T(:,2) = C(:,2)*N;
T(:,1) = I(:,1);

figure
plot(LD(:,1), LD(:,2),'color', 'black')
line(I(:,1), T(:,2), 'color', 'blue')
line(LD(:,1), LD(:,2)-T(:,2),'color', 'red')
legend('LD','Scattering','Corrected LD')

assignin('base', 'Wavelength', LD(:,1));
assignin('base', 'LD', LD(:,2));
assignin('base', 'TotalScat', T);
assignin('base', 'CorrectedLD', LD(:,2)-T(:,2));

toc;
end
```

Orient.m: **Code for determination of liposome orientation parameter S.[38] (primarily derived from Mchlaughan *et al*).**

```
function [HolderMatlab] = Orient(a,b,rpm)

% Parameters

visc = 1e-3;  %viscosity in Pa s

R_0 = 2.9; %outer diamter of couette flow cell

R_i = 2.4; %inner diameter of couette flow cell

T = 298;  %Temperature

k_b = 1.3806503e-23;  % Boltzmann constant

a = a*1e-9;

b = b*1e-9;

r = a/b;

F_t = sqrt(r^2-1)/(r^(1/3)*log(r+sqrt(r^2-1)));

F_r = (4*(r^4-1))/((3*r^2)*(((2*(2*r^2-1))/(r^(4/3)*F_t))-2));

lambda = (4*F_r*pi*visc*a*b^2)/(3*k_b*T);

global M;

R_0 = R_0/2;
R_i = R_i/2;

G = (2*pi*R_0*rpm)/(60*(R_0-R_i));

P_lambda = G*lambda; %Peclet number

N = 12; %Solution expansion order (N even)

N_tilde = (N/2+1)^2-1; %Number of non-trivial ODEs
N_total = 2*(N+1)^2; %Number of A_iqp for i=0,1, p,q=0,1,2,...,N
N_ind = N_total/2;

A = ones(N_total,1); %A_inm (or A_iqp)

for n = 0:N
    A((N+1)^2+n*(N+1)+1,1) = 0; %A_1n0=0
end

M = zeros(N_total,N_total); %Matrix of coefficients of the A_iqp for the A_dot_iqp. For
example, M(1,iqp)=M(1,i(N+1)^2+q(N+1)+p+1)

a = zeros(N+1,N+1,N+1,N+1); %a(m+1,n+1,p+1,q+1) for m,n,p,q = 0,...,N


%We calculate the a_mpnq

for n = 0:2:N

    for m = 0:2:n

        for q = 0:2:N

            for p = 0:2:q

                if ((m-p==2) && (n-q==2))

                   a(m+1,n+1,p+1,q+1)             =             (n-2)*factorial(n+m)*(1-
```

```
eq(m,0))/(4*(2*n+1)*(2*n-1)*factorial(n+m-4));

                elseif ((m-p==2) && (n-q==0))

                    a(m+1,n+1,p+1,q+1)      =      3*factorial(n-m+2)*factorial(n+m)*(1-
eq(m,0))/(4*(2*n-1)*(2*n+3)*factorial(n+m-2)*factorial(n-m));

                elseif ((m-p==2) && (n-q==-2))

                    a(m+1,n+1,p+1,q+1)           =           -(n+3)*factorial(n-m+4)*(1-
eq(m,0))/(4*(2*n+1)*(2*n+3)*factorial(n-m));

                elseif ((m-p==0) && (n-q==0))

                    a(m+1,n+1,p+1,q+1) = -m/2;

                elseif ((m-p==-2) && (n-q==2))

                    a(m+1,n+1,p+1,q+1) = -(n-2)*(1+eq(m,0))/(4*(2*n+1)*(2*n-1));

                elseif ((m-p==-2) && (n-q==0))

                    a(m+1,n+1,p+1,q+1) = -3*(1+eq(m,0))/(4*(2*n-1)*(2*n+3));

                elseif ((m-p==-2) && (n-q==-2))

                    a(m+1,n+1,p+1,q+1) = (n+3)*(1+eq(m,0))/(4*(2*n+1)*(2*n+3));
                end
            end
        end
    end
end

%After applying the Galerkin method, we obtain a linear system of ODEs.

    for q = 0:2:N
        for p = 0:2:q
            for n = 0:2:N
                for m = 0:2:n
                    M(q*(N+1)+p+1,q*(N+1)+p+1) = -q*(q+1)/6; %Coefficient of A_0qp for
A_dot_0qp

                    M(q*(N+1)+p+1,(N+1)^2+n*(N+1)+m+1)  =  -P_lambda*a(m+1,n+1,p+1,q+1);
%Coefficients of the A_1nm for A_dot_0qp

                    M((N+1)^2+q*(N+1)+p+1,(N+1)^2+q*(N+1)+p+1)       =       -q*(q+1)/6;
%Coefficient of A_1qp for A_dot_1qp

                    M((N+1)^2+q*(N+1)+p+1,n*(N+1)+m+1)  =  P_lambda*a(m+1,n+1,p+1,q+1);
%Coefficients of the A_0nm for A_dot_1qp
                end
            end
        end
    end


M = M*diag(A); %Set the coefficients of the A_1n0 to zero to account for A_1n0=0

M(1,:) = 0; %Set the coefficients for A_dot_000 to zero

for q=0:2:N
    M((N+1)^2+q*(N+1)+1,:) = 0; %Set the coefficients for the A_dot_1q0 to zero
end


x0 = zeros(N_total,1); %Initial conditions
x0(1,1) = 1;     %A_000(t=0)=1

dx = @(tau,x)  M*x;

x = ode45(dx,[0,10],x0); %Solve in the interval tau=[0,10]

N_steps = size(x.x,2); %Number of time steps in ODE solutions
```

```
syms  the Phi cThe The

poly = vpa(zeros(1,N+1));

for n = 0:N
    poly(n+1)  =  (1/(2^n*factorial(n)))*diff((cThe^2-1)^n,cThe,n);  %generate  legendre
polynomials
end

P = vpa(zeros(N+1,N+1));

for n = 0:1:N
    for m = 0:1:n
        if m > n
            P(m+1,n+1) = 0;
        else
            P(m+1,n+1) = ((-1)^m)*((sin(the))^m)*diff((poly(n+1)),cThe,m);   %calculate
matrix of associated Legendre polynomials
        end
    end
end


P_fin = subs(P,cThe,cos(the));
P_fina = eval(P_fin);  %these three lines substitute cos(the) back in for cThe

A0 = x.y(1:N_ind,:);  %generate matrix of A_0 amplitudes

A1_inp = N_total+1;
A1 = x.y(N_ind+1:N_total,:); %generate matrix of A_1 amplitudes


MM = zeros(N_ind,1);
MM(1) = 0;

for n = 1:N_ind-1
    MM(n+1) = MM(n)+1;
    if MM(n)==12
       MM(n+1) = 0;       %generate m values for psi calculation
    end
end

psi = vpa(zeros(N_ind, N_steps));

P_final = reshape(P_fina,N_ind,1);

for t = 1:1:N_steps
    psi(:,t) = (A0(:,t).*P_final.*cos(MM.*Phi))+(A1(:,t).*P_final.*sin(MM.*Phi));
end

final_psi = sum(psi(1:N_ind,:)).*(1/(4*pi));

test = final_psi*sin(the);

fun_for_S = ((sin(the)^2)*(cos(Phi)^2)).*test;  %function to be integrated

sincos = double(int(int((fun_for_S),the,0,(pi)),Phi,0,(2*pi))); %integrate with respect
to theta and phi

S = (0.5)*((3.*sincos)-1);

assignin('base', 'S', S);

holder = test(end);
Hold = subs(holder, the, The);

HolderMatlab = matlabFunction(Hold);

end
```